Stony Brook University

OFFICIAL COPY

The official electronic file of this thesis or dissertation is maintained by the University Libraries on behalf of The Graduate School at Stony Brook University.

© All Rights Reserved by Author.

Energetics and Kinetics of Epitaxial Nanostructure Formations on Topographically Patterned Substrates in Three Dimensions

A Dissertation Presented

by

Noah D. Machtay

to

The Graduate School

in Partial Fulfillment of the

Requirements

for the Degree of

Doctor of Philosophy

in

Mechanical Engineering

(Solid Mechanics)

Stony Brook University

May 2009

Stony Brook University

The Graduate School

Noah D. Machtay

We, the dissertation committee for the above candidate for the

Doctor of Philosophy degree,

hereby recommend acceptance of this dissertation.

Dr. Robert Kukta, Advisor
Associate Professor, Mechanical Engineering Department

Dr. Chad Korach, Chair
Assistant Professor, Mechanical Engineering Department

Dr. Imin Kao, Member
Professor, Mechanical Engineering Department

Dr. John Stevenson, Outside Member
Mathematics Department, Long Island University, C.W. Post Campus

This Dissertation is accepted by the Graduate School

Lawrence Martin
Dean of the Graduate School

Abstract of the Dissertation

Energetics and Kinetics of Epitaxial Nanostructure Formations on Topographically Patterned Substrates in Three Dimensions

by

Noah D. Machtay

Doctor of Philosophy

in

Mechanical Engineering

(Solid Mechanics)

Stony Brook University

2009

The formation and stabilization of strained epitaxial systems of islands on areally constrained substrates is a point of increasing interest for the promise it offers to the advancement of electronic and optical-electrical device technology. While current fabrication methods are available to readily produce micron-scale devices, as size is reduced fabrication becomes increasingly difficult. A possible solution is to use relatively large scale areal constraints, such as topographical substrate features, which can be formed via conventional techniques such as lithography, masking, and ion etching, to guide the formation of smaller structures. While the growth of nanoscale structures on larger scale patterned substrates has been investigated by numerous researchers, there has yet to be a complete explanation for why, where, and how these structures form. The goal of this investigation is to contribute to the understanding of the energetic and kinetic mechanisms governing the formation of self-assembled nanoscale structures grown epitaxially on topographically patterned substrates. Such insight is essential for the development of effective and low-cost nanoscale fabrication techniques. The current research investigates the energetic and kinetic mechanisms that guide the positioning of strained epitaxial islands in three dimensions. Continuum level models are used wherein the free energy of the system consists of surface energy and strain energy. The goal is to identify conditions that can lead to the formation of multiple island systems, and determine the influence of such factors as substrate shape, lattice mismatch, surface energy, and the amount of material deposited. The full three dimensional kinetic evolution of the film surface through the process of surface diffusion is also simulated to determine island shapes.

Contents

List of Figures

Acknowledgments

I am eternally grateful for the tireless support and patience of my parents Richard and Christine and my brother Aaron, without which this or any other work would not be possible. I gratefully acknowledges the support of my advisor and mentor Professor Robert V. Kukta. Research support for this work from the National Science Foundation through Grant No. CMS-0134123 is gratefully acknowledged.

1 Introduction

If an engineer wishes to build a macroscale device such as a car, the tools required to accomplish that goal are available and well understood. Some machine tools, a couple of wrenches, and some screwdrivers are all that may be required. If the engineer then wishes to build something on a smaller scale, such as a microchip, he is presented with a problem. Macroscale tools can no longer be used because of the limitations of spacial resolution. That is to say, a screwdriver cannot be used to build a microchip, because the flaws on the end of the screwdriver are larger than the features that need to be produced on the chip in order for it to function as designed. Fortunately, additional tools such as lithography and ion-etching exist and are well understood, allowing engineerings to produce things like microchips and similar scale devices. The question then arises as to how a device on an even smaller scale might be produced when the resolution limits of the tools available are again challenged? The answer to that question under current consideration is the use of larger scale patterned substrates to influence the spontaneous self-assembly of nanostructures in lattice-mismatched epitaxial systems.

Even when existing fabrication techniques are available, the cost associated with a reduction in scale can be prohibitive, making their deployment impractical. In such cases, a manufacturing process which takes advantage of self-assembly will again offer a solution, as the elimination of the need to directly interact with the system on the smaller length scale offers the potential for a great reduction in cost.

To continue along this line of thought for an additional step, when there are fabrication techniques available for producing a small scale device which are both practical and economical, the principles governing self-assembly must still be considered. Improperly designed devices which ignore the tendencies of materials to reorganize themselves at small scales could run into serious reliability issues if instabilities arise which essentially drive the system towards spontaneous self-disassembly. It may be possible to create a device with a particular functional configuration, but if it ends up having a natural inclination towards rearranging itself into a non-

functioning configuration then premature failures can become likely. Considering the mechanisms under current investigation can allow designers to properly address this issue and create more reliable devices.

There are then three compelling reasons to consider the mechanisms governing self-assembly in nanoscale systems. There is the potential for developing manufacturing techniques which will allow for the production of devices on length scales that are otherwise unachievable. There is also the promise of reduced cost over other competing manufacturing techniques. Finally, there is the necessity for all small length scale device designs to consider these principles so as to avoid device reliability issues arising from instabilities driving self-disassebly.

Spontaneous self-assembly of nanostructures in lattice-mismatched epitaxial systems has been a problem of long-standing interest for fabricating advanced electronic and optical devices. The idea is to deposit a material onto a substrate surface and allow inherent physical processes to control formation of the deposited material into nanostructures, such as mounds, lines, or other simple units that are the building-blocks of a particular device. The spontaneous formation of nanostructures in these systems is a well-known phenomenon that occurs during deposition, however the challenge is to produce units of a particular size that are organized in a predefined configuration. For example a device might require mounds of uniform size arranged in a regular two-dimensional array or in one-dimensional lines or line patterns. A method under current investigation for guiding the organization of epitaxial nanostructures is growth on topographically patterned substrates, wherein relatively large substrate features, formed for example by lithography and ion-etching, act as templates for positioning smaller nanoscale structures.

Epitaxy is the growth of a material using the crystallographic structure of another material as a template. In a system where one material is deposited epitaxially on another, the deposited material is essentially grown on the substrate as a continuation of the substrate crystal structure. In cases where the lattice spacing of the two materials is different, a mismatch strain results, which drives the formation of island structures and other features. When this effect is coupled with the presence

and positioning of patterns on the substrate surface, the formation and evolution of structures at particular preferred sites within that system offers a possible mechanism by which controlled formations can be designed on a small scale which would otherwise be unachievable.

1.1 General Selective Area Epitaxy

Particular focus has been on the Stranski-Krastanov mode of epitaxial growth due to its application in important semiconductor systems, such as $SiGe$ on Si. In this growth mode, islands of deposited material form atop an initial wetting layer that covers the substrate. These islands can act as quantum dots, and if properly arranged, configurations of islands may serve as the building blocks for devices with exceptional characteristics. While the mechanics of island formation is well understood [8, 9], work continues towards a technology to guide islands to self-organize into regular patterns. One possible method for achieving self-organization of nanoscale structures is selective area epitaxy.

In selective area epitaxy, deposited film material is isolated to certain areas of the substrate. The areal constraint can be achieved either through use of a patterned deposition mask [10–12], or a nanostencil applied directly to the substrate surface [13]. With both of these techniques only a specific area of the substrate is exposed to deposition, and surface mass transport is generally constrained to occur within those areas. Another technique that effectively limits growth to a confined area is the deposition of material on a topographically patterned substrate. A feature such as a raised mesa [2, 3] or an etched pit [14] can have properties similar to that of selective area epitaxy due to a significant activation barrier preventing diffusion of material past the perimeters of such features.

Epitaxial growth on a confined area has been shown to be fundamentally different from growth on large unpatterned substrates. While it is interesting that the number of islands that form can apparently be controlled by varying the size of the growth area [2, 11, 14] (smaller areas support fewer islands) this alone would not be

terribly helpful. More importantly, the multiple island configurations that arise are often regularly arranged and exhibit uniform size and shape [2, 3, 14], offering great promise for device designs that require arrays of regularly spaced and sized quantum dots. The persistence of multiple island configurations indicates that growth on a patterned substrate (as on a topographical feature or through a deposition mask) provides a strong resistance to island coarsening, which is not observed in growth on unpatterned substrates. Resistance to coarsening and the corresponding ability to achieve regular and predictable arrays of islands is critical for the advancement of this technology, however a complete understanding of the mechanisms which govern these trends has not yet been established.

1.2 Experimental Literature

Experimental research into the self organization of nanostructures, and the mechanisms that can be used to guide and control the formation of those morphological features has been extensive. Xie *et al.* [15] produced arrays of islands by separating film depositions with substrate spacer layers. It was determined that the strain field induced by the buried islands provided a driving force for increased island organization in subsequent layers. Ozkand and Nix [16] found that annealing of thin films of sub-critical thickness with respect to the formation of dislocations resulted in strain relaxation by means of surface roughening. Initially, grooves formed along preferential crystallographic planes, and subsequently formed islands when exposed to annealing conditions for longer periods of time. Tang *et al.* [17] reported the formation of $SiGe$ quantum dots by applying a coating of porous silica to a Si substrate and then using of the pores in the silica as preferred sites for material agglomeration during subsequent film deposition by molecular beam epitaxy or chemical vapor deposition. The resulting arrays of buried quantum dots were found to have improved light emission properties. Floro *et al.* [18] observed the dynamic formation of self-organized strained epitaxial islands during growth and deposition by molecular beam epitaxy of $SiGe$ onto $Si(001)$ in real time using a

spectroscopic light scattering technique. The formation of arrays of "hut clusters" was observed. Initially high degrees of order in the island arrays is credited to the reduction in island-island repulsion forces, while a subsequent drop in the degree of order is blamed on island coalescence and coarsening. Gao *et al.* [19] worked with high temperature laser ablation deposition to form epitaxial thin film systems with relatively low lattice mismatch between a $Y_2O_3 : Eu$ film and a $LaAlO_3$ substrate, and transmission electron microscopy (TEM) was used to find pores in the film. Luo *et al.* [20–22] determined that a compliant substrate will allow an epilayer system to relax part of its misfit strain, thereby reducing the occurrence of dislocation flaws while also relieving a driving force for film roughening and coarsening. The use of a buffer layer to achieve similar compliant properties at the film interface was also considered and was found to reduce the effective lattice mismatch, again reducing the driving force for dislocation formation and morphological instabilities. Liao *et al.* [23] investigated the effect of annealing on the morphology of quantum dots in sequentially layered film/substrate systems where the buried film layers act as a template, by means of the strain field they induce in the subsequent layers, for island formation. It was found that annealing conditions offered a significant degree of control over the formation of system microstructures, with annealed samples showing greater island aspect ratio and more uniform composition. Leon *et al.* [24] used dislocations as a mechanism by which control over the morphological development of a film surface can be controlled. Quantum dots were found to nucleate and grow preferentially in the trenches formed by misfit dislocations during annealing. Teichert [25] found that substrate miscut angle (i.e. the deviation from the prescribed crystallographic plane on the surface of the substrate), film thickness, and super-lattice formations can be used to achieve large area arrays of relatively uniform nanostructures in the form of both surface waves or ripples as well as islands. Tan *et al.* [26] studied the effect of partial amorphization of the substrate surface and observed that increased amorphization led to film surfaces that were smoother, showed less epitaxial registry with the substrate, and allowed greater oxygen penetration than systems with mono-crystalline substrates.

1.2.1 Patterned Substrates

Experiments have demonstrated that patterned substrates offer some control over the sites where islands (mounds) tend to form. Mui *et al.* [1] found that InAs deposited on GaAs ridges by Molecular Beam Epitaxy (MBE) forms extremely small islands 40nm in diameter and 12nm in height along the ridge. On a substrate with a valley shaped groove, it was found that islands formed either on the floor of the valley or on the side walls. Wang *et al.* [27] investigated control of quantum dot formation, size, and positioning in Ge films on Si substrates by means of raised elongated substrate mesas. Islands were found to form along the crest of a mesa stripe with a high degree of uniformity, which is credited to the elastic interaction between the islands and the substrate.

Kitajima *et al.* [2] investigated self-assembly of Ge islands on patterned silicon substrates. The motivation for their work was the precise alignment and position of material which is required for the integration of nanostructures in semiconductor devices. The silicon substrate was first coated with a layer of polymethyl-metacrylate (PMMA), and patterns in this coating were created using a 20keV electron beam. The spacing of features on the substrate surface was limited to 120nm due to the resolution limits of the apparatus. The unmasked areas of the substrate surface were then etched to a depth of 20nm by exposure to chlorine plasma, and the remaining PMMA mask was removed. Material was deposited via molecular beam epitaxy. In an attempt to determine the mechanisms of island formation and positioning, the experiment was repeated with square mesa dimensions of 700nm, 500nm, 300nm, and 140nm.

For large mesas Kitajima *et al.* [2] found that nucleation occurred at the mesa edges and corners, and also at random locations across the top of the substrate mesa. For smaller mesas, the edge and corner locations were found to be preferred nucleation sites over other interior locations. For yet smaller mesas, only a single island was found to form on the mesa top, either centered on the mesa, or offset to one side. It is speculated that the preference of the mesa edges and corners for

certain systems is due to the lateral deformability of those locations and the reduced constraint of the substrate which allows for a reduction in strain relative to other potential nucleation sites. It is further noted by Kitajima *et al.* that the mesa tops maintain lower strain levels, and surface diffusion is expected to favor the relocation of deposited material from more constrained locations within the substrate topology to the mesa top.

Jin *et al.* [3, 28–30] formed stripe patterns on a Si substrate using selective gas-source molecular beam epitaxy. Ge was then deposited on the patterned substrate by Knudsen cell source molecular beam epitaxy. It was found that regular arrays of islands form along the ridges of stripes. Island formations on square substrate mesas were also investigated [3, 29, 31, 32]. Deposited islands were found to form preferentially at the four mesa corner locations. With further deposition a fifth island was found to form at the mesa center. A possible mechanism for the formation of this central island is offered by Jin *et al.* as the result of island strain field interaction which in turn alters the energy distribution on the mesa top, resulting in a shift in the relative favorability of sites within the substrate topology.

Lee *et al.* [33] investigated the use of circular substrate mesas with a diameter of less than 100nm in an attempt to produce smaller quantum dot structures. They suggest that a reduction in strain energy in the system at this size scale allows for the growth of Ge dots with increasing aspect ratios. Flat substrate samples were coated with PMMA, which was then selectively removed by lithography. Subsequently, the exposed substrate surfaces were plasma etched and the remaining PMMA mask was removed to achieve a desired substrate topology. Ge islands were then formed on the substrate via ultra high vacuum molecular epitaxy. Lee *et al.* report the formation of islands around the perimeter of the circular mesas, consistent with the observations of Jin *et al.* and Kitajima *et al.*. They add that for mesa structures with diameters of about 65nm, island base dimensions can be reduced to about 10nm. It is important to note, however, that these conclusions are made from the observation of arrays of similar mesa structures. Various island configurations were observed on mesas of similar size. While it can be generally noted that islands favor the mesa

edges and occasionally form in central locations, without more careful controls it is difficult to draw any more specific conclusions regarding island placement from these results.

These experiments demonstrate that a relatively large scale topography can guide the organization of smaller scale features, however they offer limited insight to the mechanisms that govern this spontaneous organization. Conventional wisdom is that islands will tend to form at sites of low free energy, as islands near the edge of a mesa tend to be most favorable because the relatively high compliance at the boundary can act to relax misfit strain and thereby reduce the strain energy of the system. However recent experiments by Zhong *et al.* [4, 34] suggest that Ge islands grown on a Si substrate patterned with lateral stripes in the $\langle 110 \rangle$ direction do not form as predicted by energetics alone. Substrate stripes were formed via holographic lithography and reactive ion etching with a period of less that 1μm. The effects of variations in sidewall geometry were considered for different cases. The edges of the top terrace locations of the stripe substrate structures are identified as energetically favorable sites for islands to form. Their experiment shows that islands do not form at these predicted locations, preferring instead to form on the stripe sidewalls and trenches. It is proposed by Zhong *et al.* that kinetic considerations govern the nucleation and formation of deposited islands, accounting for the experimentally observed variation from energetically predicted results.

1.3 Theoretical Literature

To explain the experimental results discussed above, it is first useful to review the case of islands on a flat substrate, as similar mechanisms guide island positioning on patterned substrates. For islands of a given volume, strain energy is lower for a high aspect ratio island than a low aspect ratio island. This is because a higher aspect ratio is more effective at relaxing mismatch strain in the island and thereby acts to decrease the total strain energy of the system. At the same time, surface area and therefore surface energy increases as an island increases in aspect

ratio. Strain energy and surface energy compete to determine the equilibrium shape of an island.

Tersoff has done extensive investigation [35–39] into the growth of epitaxial structures. layered growth was considered, and found to stabilize for a sufficient number of layers due to a reduction in strain energy [35]. The effect of stress on the morphological evolution of a surface was then considered, and identified as a driving mechanism for roughening in heteroepitaxial systems [36]. The contention was made that contiuum-theory based models should be appropriate for simulations which separate energy into surface, bulk, and other components, particularly for simple geometries [37]. Misfit stress was found to influence the growth of heteroepitaxial systems, resulting in the self-assembly of quantum dots, quantum wires, and quantum wells [38]. The importance of kinetics on the formation and morphology of strained heteroepitaxial layers was also asserted [39].

Jonsdottir and Freund [40] associated the occurrence of equilibrium surface roughness or waviness in epitaxially grown films with the formation of defects along the film-substrate interface. These non-uniformities in the strain field result in a chemical potential gradient along the surface of the film, which drives the surface diffusion of film material as the system attempts to reach equilibrium. As a result, the final configuration exhibits a rough or wavy surface. An analytic expression for the final surface shape was found by enforcing uniform chemical potential as the condition for equilibrium. That equation was solved numerically, and surface roughness was determined for a range of system parameters. The surface roughening was found to vary from just a small percent of the nominal film thickness, up to a significant portion of the nominal film thickness.

Shchukin *et al.* [41] looked at three dimensional pyramid and elongated prism shaped islands on a lattice-mismatched substrate. The elastic interaction between islands was considered for systems with high areal density, with the dipole-dipole elastic repulsion between islands being the primary contributing factor. The energy per unit area of the systems was determined as a function of surface coverage for one dimensional arrays of elongated prisms, two dimensional arrays of square pyramids,

two dimensional "checkerboard" distributions of square pyramid islands, and two dimensional hexagonally distributed square pyramids. It was concluded that when particular conditions are met periodic arrays of equally sized islands will be stable. Criteria for stability of a square lattice of strained islands were offered in relation to the material and configurational parameters of the system.

Johnson and Freund [9] investigated the formation of an epitaxially mismatched island on a flat substrate and calculated minimum energy morphologies versus volume of deposited material using a finite element model. An isolated island on a large substrate was considered under plane strain conditions. Islands were modelled as portions of a semicircular arc described by the cross-sectional area of the deposit and the aspect ratio of the island. The total energy of the system was taken to consist of surface energy and strain energy, which results from the lattice mismatch between the island and substrate. It is noted that multiple islands on the flat substrate will have a tendency to repel each other as the competing strain fields induced by each island would interact at close proximity. It is also noted that larger islands are expected to favor higher aspect ratios while smaller islands favor lower aspect ratios. This results from the reduction in strain energy associated with islands of increasing aspect ratio in which material is further removed from the constraint of the substrate, and the competing increase in surface energy that follows that change in morphology. Larger islands were found to take greater advantage of this strain energy reduction, while smaller islands were better able to lower their system energy by taking advantage of the lower surface energy of a flatter shape.

Using similar energetic assumptions and arbitrary shapes expressed by Fourier series, Kukta and Freund [8] investigated the formation of film morphologies on an unbounded half-space. The film surface was modelled as a periodic function along the interface axis with some system dependant wavelength, and the elastic field was found by solving a boundary integral equation. The formation of island structures was found to be favorable, despite the tendency of surface energy to drive the formation of a uniform flat film, for cases where the mismatch between the deposit and substrate materials are sufficiently large. In addition, the coalescence of two islands

into a single larger island was found to be energetically favorable. However there is evidence that elastic interactions between islands might impede the kinetic process of coalescence [42, 43].

Suo and Zhang [44] investigated stability in epitaxial films induced by long-range forces. While the competition between surface free energy and strain energy is often regarded as the driving force behind the evolution of thin film morphologies, this paper suggests that more distant forces can exert an influence in competition with those accepted driving forces. Attractive and repulsive long-range interactions are considered. In particular, van-der Waals dispersive forces and quantum confinement and charge transfer in metallic films are offered as physical example of long-range forces. It is concluded that such forces within a system can stabilize a thin film against stress driven evolution.

Chiu [45] presented a theoretical simulation on the evolution of a Stranski-Krastanov system through the process of annealing. Strain energy, surface free energy anisotropy, and film/substrate interaction energy were included in the model. Both surface energy anisotropy and film/substrate interaction energy were found to influence the formation of arrays of islands which were stable against coarsening. The explanation was offered that both the surface energy anisotropy and the film/substrate interaction energy act to suppress the relaxation of strain energy which, left unopposed, would favor coarsening. Strain energy relaxation would drive the system to increase the size of an island, and to increase the aspect ratio of the island, in both cases relieving strain by further removing material from the elastic constraint of the substrate. The competing surface energy and interfacial interaction energy would conversely drive the system in the opposite direction, with surface energy favoring flatter islands, and film/substrate interaction energy favoring smaller islands. Combined, these two factors serve as a check against unfettered strain driven system ripening, and result in a stable array of islands.

Ortiz *et al.* [46] offered a continuum model for the growth of thin films using a series expansion technique and considering deposition and film/substrate interfacial energy. The physical processes represented in the model include surface

diffusion, evaporation-condensation, and forced material migration driven by the film/substrate interfacial energy. Flat films below a certain critical thickness were predicted to be stable as a result of the interface energy term. Above this critical thickness, film coarsening is predicted to occur, and is presented in the context of a mechanism facilitating the nucleation of islands within the system. For greater film thicknesses, system trends favoring the formation of particular morphological features are identified. Evaporation-condensation diffusion favors the accumulation of material on portions of the film surface which are relatively flat, and the migration of material away from locations on the film surface which are relatively steep. The balance between those effects will drive the system towards a particular favored slope angle.

Zhang [47–49] investigated the formation, evolution, and stability of epitaxially strained thin films. A three dimensional continuum model considering strain energy, surface energy, and surface anisotropy was first used to model the formation of epitaxially strained islands, and the formation of regular arrays of islands was observed for certain system configurations and annealing conditions [47]. The effect of surface energy anisotropy on coarsening, ripening, and the strength of observed self-organization was then studied, and it was found that small changes to the anisotropic nature of the system could have significant effects on those properties [48]. The stability and dominant growth mode of a biaxially strained thin film was then analyzed using first order perturbation analysis, and a transition between the formation of islands and the formation of wires was reported, with dependencies on the Poisson's ratio of the system and the relative values of the principle stresses [49].

Floro *et al.* [42] observed island coarsening in epitaxial systems using light scattering spectrography. Molecular beam epitaxy was used, and the deposits formed as pyramidal "hut clusters". The island spacing and areal density were measured with respect to time during deposition and subsequent annealing. Island coarsening of "hut cluster" morphologies was found to proceed in a manner inconsistent with the common view of Ostwald ripening. This inconsistency is credited to

the effects of elastic interactions between islands, and by incorporating these effects into a model, it was found that calculations could be brought into better agreement with experimental observations, depending on the island size. Coarsening with deposition was considered using a numerically solved standard mean field analysis approach, however the results of that investigation were not able to satisfactorily reproduce the experimental findings, indicating that the effects of deposition alone cannot fully explain system coarsening. The mean field analysis was then modified to include elastic interactions using results obtained from finite element calculations. The addition of elastic interactions into the model produced mathematical solutions that were in good agreement with experimental results, showing that the combined effects of deposition and elastic interactions influence the nature of system coarsening.

F. Liu *et al.* [5] investigated self-assembly and coarsening of two dimensional islands. The effect of strain driven island-island interaction on island size and position was considered for systems with only mass transport based coarsening, as well as systems with combined mass transport and island migration. The analytic solution is complemented with computational simulation. At each step in the simulation, the chemical potential of each island is determined, including a component resulting from the island-island interaction, and island size and position evolve in response. A periodic boundary condition was employed. In the case of fixed islands, a power law relationship between island size and the number of islands occupying a given area was identified. When island migration was also considered, it was determined that island-island interaction is expected to control island motion (via island edge diffusion), resulting in regular arrays of islands with uniform size and spacing. First, an initial distribution of islands was developed, random in both size and position. The final converged distributions of island for the cases where only mass transport was considered, and when both mass transport and island translation were considered were then determined. It is noted that the island-island interaction favors the formation of relatively uniform distributions of islands, both in terms of island size as well as spacing.

The self-assembly of both strained and unstrained three dimensional islands was considered by F. Liu [50]. The island-island edge interactions are modeled as a dipole and incorporated into a Volmer-Weber growth simulation. The most favorable configuration for a single unstrained island on a sparsely populated surface (i.e. no island-island interaction) was first determined. Coarsening of these unstrained islands during later growth stages, governed by chemical potential gradients, was then simulated. This analysis was conducted both for dilute systems (no inter-island interaction) and dense systems (significant inter-island interaction). The effect of island-island interactions on the growth and stability of strained islands was then determined by numerical evaluation, and it was determined that those interactions served to stabilize the islands against coarsening.

P. Liu *et al.* [51–56] have looked into the growth of islands and arrays of heteroepitaxial islands. First, a three dimensional continuum based simulation was used to model the growth of quantum dot superlattices using a layering technique in which subsequent thin film deposits trend towards an ordered morphology as a result of the influence of the elastic interaction with the previously deposited system [51]. The stress distribution in a strained epitaxial island was then analyzed using a combined atomistic and continuum model utilizing molecular dynamics for the island and adjacent substrate, and finite element method for the remaining system. From that work it was suggested that a nonlinear elasticity assumption could be used to reconcile the relationship between the strain level in the system and the resulting surface roughness [52]. The effect of elastic anisotropy on the formation of heteroepitaxial islands was considered and it was determined that increased anisotropy favors more pronounced island self-assembly and alignment, with island spacing depending strongly on the smallest wavelength surface instability in the anisotropic film [53,55]. The role of growth rate in the formation of heteroepitaxial islands was investigated as part of a three dimensional simulation and was found to have a strong effect on the coarsening kinetics of the system, with densely spaced smaller islands forming for high growth rates and more sparsely arranged larger islands forming for slower growth rates [54]. A three dimensional simulation including both surface energy and

elastic anisotropy was used to model the self-assembly of islands and it was found that increased surface energy anisotropy resulted in increased faceting of islands, and increased resistance to shape transition [56].

Eggleston and Voorhees [6] analyzed the use of a patterned substrate to induce a morphological instability in a deposited film. It was found that if a lattice mismatch exists between the film and substrate, the instability can propagate along the surface of the system in the form of a traveling wave, which results in large regions of highly ordered nanocrystals in the vicinity of the substrate feature. It was shown that substrate topology can result in the formation of a regular distribution of nanostructures. A film thickness of zero (i.e. no film material has been deposited, so the substrate is bare) was first considered. It was then shown that for increasing film thickness the local effect of the morphological instability caused by the mesa is the formation of islands centered around the feature. With further film deposition the instability begins to propagate out from the mesa, and finally the instability is shown to have propagated to produce highly ordered structures over approximately three to four times more of the substrate surface than was occupied by the topographical pattern. While this analysis does offer a method for producing large areas of ordered structures, it relies on the deposition of a film with thickness greatly in excess of the pattern applied to the substrate. As a result, the substrate feature would seem to have to be small in terms of height compared to the dimension of the final structures, and at least comparable in terms of the surface dimension. This could apply a lower limit to the spacial resolution that can be achieved with a technique based on this mechanism. An interesting question that arises is whether the morphological instability which is utilized here could be better understood and characterized in the earlier stages of deposition where the nominal film thickness is lesser, and therefore the dimensions of the resulting structures could be further reduced.

Chiu *et al.* [7] conducted a numerical simulation using a continuum model for a Stranski-Krastanov film-substrate system. Evolution of the system is driven by an elastic mismatch between the film and substrate, as well as film-substrate interfacial energy, and surface free energy. The use of patterns on the *film* surface were consid-

ered as possible mechanisms for controlling morphological evolution. Film thickness was restricted such that surface undulation was suppressed while still allowing for island nucleation. It was found that the introduction of film surface patterns will influence the formation of nanostructures within the system. As the size of the pattern is increased, the system switches from arrays of relatively uniform islands to regular rim structures. The presence of a disproportionate pattern dimension, such as a long side on a rectangle, can act to favor line or rim formation over island formation. It is important to be clear that the patterning used by Chiu *et al.* is being made on the *film* surface as opposed to the *substrate* surface.

Chiu [57] also employed an energy analysis and accompanying numerical simulation to look at the resistance of Stranski-Krastanov islands to coarsening. Evolution by surface diffusion was considered, and results suggest that stability against coarsening can arise as a result of film-substrate interaction and mismatch strain. This stability can allow for the growth of regular arrays of islands, the size and spacing of which can be controlled via the length scale of the system, as well as the introduction of patterns to the film surface as mentioned previously. The film-substrate interfacial energy was modeled within the continuum framework as a particular form of surface energy where the analogous for the surface energy density varies with the thickness of the film at any given point. This same method is employed in the current investigation, as discussed later. Chiu *et al.* [58, 59] went on to investigate the use of an exterior electrical field to induce patterning in a film surface.

Work by Kukta and Kouris [43] simulates the chemical potential driven kinetic processes of deposition and diffusion. The film and substrate surfaces are modelled as truncated Fourier series expansions, with a wetting layer maintained across the surface of the substrate. While this work deals with patterned substrates in particular, it sheds light on issues of island morphology and coalescence on flat substrates. The system morphology was found to be dependant on the relative rates of deposition and surface diffusion with relatively slow deposition resulting in energetically favorable configurations while rapid deposition can result in metastable

system states. Metastabilities were found to occur as islands became locked into apparently energetically unfavorable positions due to an energy barrier along an otherwise admissible pathway. Island coalescence was found to be be favorable in general. Large islands in close proximity were found to be metastable against ripening, while increased separation or a reduction in island size removed this barrier, suggesting that that island metastability against coarsening is caused by elastic interactions.

Pang and Huang [60] looked at the dynamics of film surface evolution and in particular stress and interfacial energy driven effects. The stress field of the system was evaluated using a second order approximation and the interface was modeled by a nonlinear wetting potential which were solved numerically using a spectral method. Instabilities in the stress governed thick film (where the substrate is remote from the film surface) system were identified which result in the formation of two dimensional crack or three dimensional pits in the film surface. These effects were found to be suppressed by the interfacial effects in systems with relatively thin films. Subsequent coarsening and stabilization in these systems was reported, suggesting that a combination of stress field and interface effects can provide a mechanism for the formation of self-assembled islands or quantum dots. The substrate considered was either flat, or remote from the film surface.

Recent work by Pandey and Kukta [61] investigated the role of anisotropy on the formation and positioning of monolayer islands. Island repulsion and directional preference were identified, and it was concluded that moderate levels of anisotropy provided the greatest degree of self-organization amongst islands. Several theoretical and computational investigations have been done very recently to understand the mechanisms by which islands self-organize on patterned substrates [43, 62–65]. All of these investigations focus on substrate topography as the driving force for organization.

1.4 Summary of the Previous Investigation

The previous investigation [62, 66] considered island formation atop square mesa structures to determine if observed organized configurations [2, 3, 33] were likely energetic or kinetic in origin. Free energies were calculated to assess the relative favorability of different morphologies. For analytical convenience, the system was treated in two dimensions (plane strain) where a morphology was characterized by the number of islands atop the mesa, island positions, and the shape of individual islands. Island shapes were restricted to circular arcs and were characterized by volume and height-to-width aspect ratio, similar to the work of Johnson and Freund [9] for islands on a flat substrate. The specific question was whether islands were most likely to form (a) at the edges of the mesa, (b) in the center, or (c) as a combination with islands at the both the edges and at the center. Kitajima *et al.* [2] found that each of these configurations can occur depending on the diameter of the mesa and Jin *et al.* [3] found that either (a) or (c) can occur depending on the amount of material deposited. Free energies of the different configurations with a given volume of deposited material were compared to find the configuration of minimum free energy and determine if it changes as mesa width is decreased or as the amount of material deposited is increased.

The analysis was based on the assumption that the system free energy consists of surface free energy and strain energy, which arises from a lattice mismatch between the island and substrate materials. The island-substrate interface is commensurate and free of defects; in such cases interfacial energy is typically small compared to other energy contributions and was therefore considered negligible. The same assumptions were used in previous two dimensional analyses of island formation on a flat substrate [8, 9, 67, 68].

The nature of the competition between strain energy and surface energy implies how substrate patterning might affect island morphology. For example, consider two configurations; (a) two small islands at the edge of a mesa versus (b) one large island at the center of the mesa as shown in Figure 1. A need to minimize strain

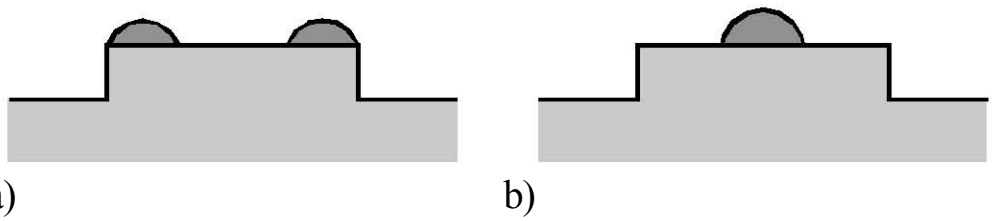

Figure 1: Two competing island formations: a) two small islands at the edge of a mesa (b) one large island at the center of the mesa. An increase in strain energy would favor configuration (a), as islands at the edges would be more effective in relaxing mismatch strain, whereas an increase in surface energy would favor configuration (b), as surface energy is reduced when two islands merge to form a larger island.

energy would favor configuration (a), as islands at the edges would be more effective in relaxing mismatch strain—the mesa edges are more compliant than the centers. On the other hand, a need to minimize surface energy would favor configuration (b), as surface energy is reduced when two islands merge to form a larger island. Consequently, in cases where mismatch strain is large, multiple islands clustered at the mesa edge are expected to be favored, while in cases where surface energy is large a single large island is expected to be favored. This transition was observed in the previous investigation. However, more interesting a second transition was observed such that as mismatch strain is increased or as surface energy is decreased the favored configuration transitions from a single island (b) to two islands (a) and back to a single island (b). Similar transitions were found to occur with decreasing mesa size and with an increasing amount of island material deposited on the substrate. These observation were consistent with published experiments [2, 3]

Additional analysis was conducted to identify possible paths for island coarsening based on the premise that an uncoarsened morphology formed during nucleation of the system will become unstable as deposit volume increases. If a system under such a condition is to coalesce into a coarsened energetically favorable configuration, the activation energy of the transformation must not be prohibitively high. If an energetically feasible path is not available, then the island configuration can

remain trapped in a high energy state. Such metastability could explain a system's resistance to coarsening even as continued deposition makes such persistence of state increasingly unfavorable. The condition for one island to grow at the expense of, or by the consumption of another island is for the chemical potential of the donor island to be higher than that of the recipient island. The chemical potentials of islands in multi-island configurations were compared to determine the feasibility of formation for the single centered island from a system with both edge and centered islands, and for the asymmetric single island from a system with islands at both mesa edges. These systems were selected in order to help understand barriers that may exist which can prevent the transformation of expected nucleation states into otherwise favorable final configurations.

These energetic mechanisms provided a great deal of insight into the behavior of epitaxial systems, but they failed to form a complete model for the formation of epitaxially grown nanostructures. Morphologies observed by experimental researchers [2, 3, 33] often have configurations which are apparently not low energy states. Often the coarsening of multiple small islands into a single larger island lowers free energy, even though experimental results have shown that uncoarsened states can persist, and energetic models may fail to identify a process barrier. Two dimensional kinetic modeling was applied to identify auxiliary or complimentary control mechanisms which may also influence the development and form of nanostructures towards an otherwise unfavorable state. Of special concern was the possibility of kinetic metastability through deposition barriers or surface diffusion barriers, and conditions where the evolution of the system is sufficiently slow that energetically unstable configurations might persist past an annealing period. To provide some insight into these mechanisms, the kinetic processes of deposition and evolution through surface diffusion were simulated. Results lent to the understanding of metastable and slowly evolving configurations, and provided insight for appropriate expansion of concept for future investigation. The kinetic model applied for that analysis was developed by Kukta and Kouris [43].

1.5 Scope of the Current Investigation

The current investigation expands on the previously developed understanding of island formation mechanisms using both an energetic and a kinetic model for three dimensional island formation.

The energetic investigation is an extension of previous work [69] that provided some basic insight into the role of the areal constraint. The current investigation addresses a wider range of possible island configurations and presents equilibrium and metastable configurational phase diagrams that suggest probable states as a function of system parameters. Parameters include that epitaxial system in question, the size of the growth window, and the amount of material deposited. By addressing a wide range of configurations, it is possible to make qualitative comparisons with experimentally observed system configurations from literature [2, 3].

The relative favorability of different deposit material distribution morphologies on areally constrained substrate surfaces was determined. The energetic analysis was used to determine the optimal number of islands for a given set of system parameters. Island shapes were approximated using physically reasonable geometry as described later. This was done while granting the concession that these island shapes may not represent the exact stable configuration for islands on a substrate surface. While island shapes might change if the system could be relaxed, the general trends which are identified (such as the preferred numbers of islands for a given case) will provide a guideline to understand the mechanisms governing the formation of such systems. Due to computational limitation, this problem was not addressed by kinetic simulation.

For the kinetic simulation, the film and substrate surfaces were modeled as truncated two dimensional Fourier expansions. The competing film evolution driving forces of strain energy, surface free energy, and the film/substrate interfacial energy were considered. System free energy was evaluated using a 2nd order approximation, and film surface evolution was calculated spectrally. Using this method unconstrained island shapes were determined. Equilibrium island shapes for a film

on a flat substrate were determined by kinetic evolution for varying system parameters for cases with high areal density. Next, the equilibrium island shapes for a film on a flat substrate were determined by kinetic evolution for varying system parameters for cases with lower areal density as an approximation for isolated islands.

2 The Effects of Areal Constraint

2.1 Areal Constraint Model

There are three essential elements to the mechanics of island formation in Stranski-Krastanov systems. The first is the strain energy associated with a lattice mismatch between the deposited material and the substrate. The strain energy of an island configuration is generally lower than an equivalent flat film configuration, and hence strain energy drives island formation. Surface energy (assumed isotropic), on the other hand, is minimum for the flat film configuration and therefore competes with the driving force for island formation. For an island of a given volume the relative magnitude of surface energy to strain energy determines the height to width aspect ratio of the island. High strain energy and low surface energy leads to a high aspect ratio, while low strain energy and high surface energy leads to a low aspect ratio. During Stranski-Krastanov growth, the first few monolayers of deposited material form a wetting layer on the substrate and hence a third ingredient is needed to inhibit island formation during the early stages of growth. This is typically introduced in the form of a wetting layer potential that penalizes roughness formation at locations where film thickness is small [8, 65, 70, 71]. In terms of energy, the wetting layer potential is characterized by an additional film surface energy that depends on the local thickness of the film. The additional energy becomes large as thickness approaches zero and decays monotonically with increasing thickness.

The wetting layer is taken to be of uniform thickness H. For simplicity an island is considered to be axisymmetric with its shape characterized by its radial size R and aspect ratio $a = h(0)/R$ such that the height of the island above the wetting layer is given by

$$h(r) = \frac{aR}{4}\left(1 - \frac{r^2}{R^2}\right)\left[4 + (4+\pi^2)\frac{r^2}{R^2}\right]\cos^2\left(\frac{\pi r}{2R}\right) \tag{2.1}$$

where r is the radial position. The height function $h(r)$ is chosen such that the island meets the wetting layer with zero slope, as typical of islands with isotropic surface energy [8]. Furthermore, in order to limit the parameter space, curvatures

at $r = 0$ and $r = R$ are taken to vanish. According to (2.1), the volume of an island is given by

$$V_I = 1.18344aR^3 \tag{2.2}$$

The strain energy is calculated semi-analytically under the assumption of isotropic linear elasticity where the island, wetting layer, and substrate are assumed to have the same elastic constants. The substrate is taken to be a half-space. It is noted that while islands are constrained to form on a finite area determined by an open window in a mask, the mask is assumed to have negligible stiffness and can therefore be neglected in the elastic boundary value problem. The film surface is traction-free and, relative to the substrate, the film material supports a homogeneous transformation strain ϵ_0, which accounts for the lattice mismatch. An approximation is made for small values of aspect ratio. A first order approximation is found to miss necessary features and therefore a second order approximation is obtained following the method outlined elsewhere [43, 72]. In the case of no wetting layer ($H = 0$) the total strain energy of a single island system is

$$\begin{aligned} U_I &= V_I M \epsilon_0^2 \Bigg[1 - 1.67425(1+\nu)a \\ &+ \frac{3.04705(1+\nu)(0.87879-\nu)(2.01847+\nu)}{1-\nu} a^2 \Bigg] \end{aligned} \tag{2.3}$$

where $M = 2G(1+\nu)/(1-\nu)$ is the film modulus, ν is Poisson's ratio, and G is the shear modulus. In (2.3), the first term in square brackets is due solely to the mismatch strain, while the second and third terms are respectively the first and second order corrections of the energy associated with the island geometry. The raised nature of an island allows for relaxation of a portion of the mismatch strain thereby reducing the strain energy of the island relative to an equivalent flat film. Note the first order correction (second term) is negative definite for values of $-1 < \nu \leq \frac{1}{2}$, while the second order correction (third term) is positive definite. This indicates that the driving force for an island to increase in aspect ratio decreases with increasing aspect ratio, which is missed by the first order approximation.

The addition of a wetting layer of thickness H over area A of the substrate adds strain energy

$$U_w = AHM\epsilon_0^2 \tag{2.4}$$

to the system. In order to limit the parameter space of this investigation, the energies associated with the wetting layer boundary, where it meets the mask, are omitted. A typical wetting layer is only a few monolayers in thickness. Hence the boundary should be treated as an atomic scale step rather than a continuum level boundary [72, 73]. Energies associated with the boundary include the partial relaxation of mismatch strain near the boundary and a step edge excess energy. Both of these energies require additional constitutive parameters, and to avoid obfuscating the basic result with additional parameters, it is assumed that these energies offset each other; in other words, it is assumed that the energy reduction due to strain relaxation equals the increase associated with step edge excess energy. Detailed consideration for these energies may have significant effect, depending on the specific material system, and should be addressed in future work.

Surface energy per unit area of the film surface is taken to be a constant γ. In the case of a flat film of area A, the total film surface energy is

$$\Gamma_0 = \gamma A \tag{2.5}$$

Introduction of an island adds surface energy

$$\Gamma_I = 3.07842a^2R^2\gamma \tag{2.6}$$

which is an approximation for small values of a, consistent with (2.3). This energy is positive definite and therefore acts as a penalty against the formation of islands. One should note that it represents the first order effect of island shape, similar to the second term in (2.3); both scale as a^2, considering that V_I in (2.3) scales with a. The second order correction to (2.6) vanishes.

The wetting layer potential energy acts to modify the surface energy such that the penalty against island formation is increased for relatively thin films, where the

notion of "thin" is defined by a material length parameter l. The potential energy for a flat film of area A and thickness H is given by

$$\Gamma_{w0} = \gamma_w A e^{-H/l} \tag{2.7}$$

where γ_w is an energy per unit area. This term effectively increases surface energy by the amount of γ_W for $H = 0$ and decays as H becomes large compared to l. An island adds energy

$$\Gamma_{wI} = -\gamma_w \pi R^2 e^{-H/l} + \int_{S_I} \gamma_w e^{-(H+h)/l}\, dS \tag{2.8}$$

to the total wetting layer potential energy, where S_I denotes the surface of the island. Equation (2.8) replaces the energy associated with the island's footprint (first term) by that of the island's surface (second term). Maintaining the current second order approximation in aspect ratio, (2.8) can be written as

$$\Gamma_{wI} = \gamma_w \pi R^2 e^{-H/l} f(a, aR/l) \tag{2.9}$$

where

$$f(a, aR/l) = \frac{1}{R^2} \int_0^R e^{-h(r)/l} \left[2 + h'(r)^2\right] r\, dr - 1 \tag{2.10}$$

is a dimensionless function of dimensionless variables a and aR/l. It is noted that the exponential in (2.10) is not approximated because the exponent $-h(r)/l$ scales as aR/l and the ratio l/R may be similar to or even smaller than a.

The total free energy of a system with n islands is given by

$$\mathcal{F} = n(U_I + \Gamma_I + \Gamma_{wI}) + U_w + \Gamma_0 + \Gamma_{w0} + U_{II}^n \tag{2.11}$$

where U_{II}^n is added to account for the elastic interaction energy between islands. A general semi-analytical result for the second-order approximation of U_{II}^n is difficult to obtain. Therefore, the system will be considered without the effects of the interaction energy. The previous investigation [69] addressed a specific case including the interaction energy and showed that while the effects are of interest, they do not wash out the results found when neglecting the interaction energy term.

2.2 Areal Constraint Analysis

In the case of an unbounded deposition area ($A \to \infty$), the model described in the previous section predicts that a single island configuration is always lower in free energy than an equivalent system with more than one island. The current understanding is that additional physics, such as faceting, is needed to stabilize a multiple island configuration [41,70]. However, it is demonstrated here that constraining deposition to a finite area will also stabilize a multiple number of islands.

For square windows of area A, minimum energy configurations are calculated for a given volume of deposited material. Expanding on the previous work, cases with two-islands, three-islands, four-islands, five-islands, six-islands, seven-islands, eight-islands, and nine-islands were considered so as to provide deeper insight into the possible correlation between areal constraint and observed system configurations. For each case the islands within a particular configuration are assumed to have the same size and shape. In the two-island case, the islands are located at opposite corners of the square growth window. For the three-island case the islands are in a triangular formation within the square growth window. In the four-island case the islands are located at the corners of the square window. For the five-island case there is one island at each corner of the growth window, and a fifth island at the center of the growth window. The six-island case consists of an island at each corner and two islands in the center. The seven and eight-island cases consist of three islands lining two opposite edges of the growth wind with either one or two additional islands in the interior region, repsectively. The nine-island configuration consists of a three by three square array of islands within the growth window. These configurations are shown in Figure (2). The total volume of material deposited in the window is given by

$$V_T = nV_I + AH = AH_0 \tag{2.12}$$

where n is the number of islands, V_I is the volume of an island (2.2), and H is the wetting layer thickness. It is convenient to represent the deposited volume in terms

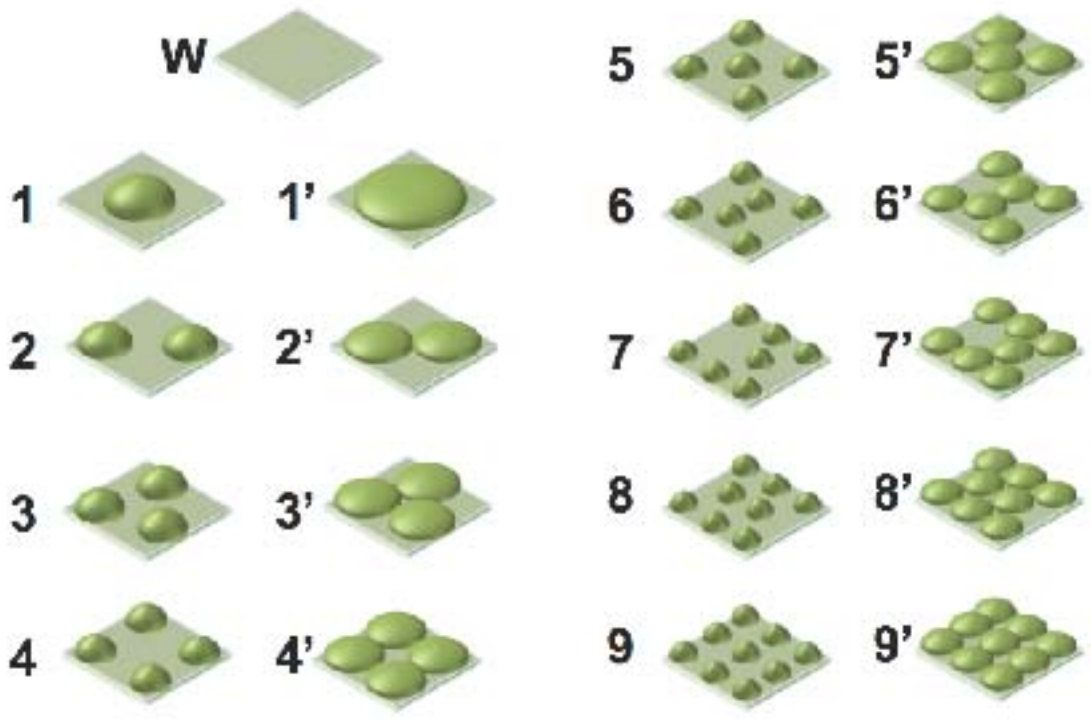

Figure 2: Geometric configurations under consideration with just a wetting layer (W), a single island (1), two islands (2), three islands (3), four islands (4), five islands (5), six islands (6), seven islands (7), eight islands (8), and nine islands (9). The prime state of each island configuration (1',2',3',4',5',6',7',8',9') indicates that the islands within the respective system are of the maximum size allowed by the areal constraint of the growth window.

of the nominal film thickness H_0 which is the thickness of a flat film of the same volume.

For a given area A and nominal thickness H_0, the configuration is defined by the number of islands (1-5), the aspect ratio a and footprint radius R of the island(s), and the wetting layer thickness H. In addition to these geometric variables, the system is characterized by the material constants ϵ_0, M, ν, γ, γ_w and l. The parameter space is reduced considerably by rewriting energy in the dimensionless form

$$\bar{\mathcal{F}} = \frac{\mathcal{F}}{\gamma L_e^2} = \bar{\mathcal{F}}(\bar{H}, \bar{R}, n; \bar{A}, \bar{H}_0, \bar{l}, \bar{\gamma}_w, \nu) \tag{2.13}$$

where

$$L_e = \frac{\gamma}{M\epsilon_0^2} \tag{2.14}$$

is the epitaxial length scale. The dimensionless energy is a function of the dimensionless configuration variables $\bar{H} = H/L_e$, $\bar{R} = R/L_e$, and n and a function of the dimensionless system constants $\bar{A} = A/L_e^2$, $\bar{H}_0 = H_0/L_e$, $\bar{l} = l/L_e$, $\bar{\gamma}_w = \gamma_w/\gamma$, and ν. Certain physical constraints must be imposed on the configurations. Firstly, the wetting layer thickness is bounded by $0 \leq \bar{H} \leq 1$ which excludes a negative thickness and provides that no more than the entire volume is contained in the wetting layer, thereby avoiding any unreasonable physical paradoxes. Additionally the island footprint radius must be non-negative and is also limited such that the island(s) fit completely within the growth window; therefore $0 \leq \bar{R} \leq m_n \bar{A}^{1/2}$ where $m_n = 1/2$ for $n = 1$ (one island), $m_n = 1 - \sqrt{2}/2$ for $n = 2$ (two islands), $m_n = 2/(4 + \sqrt{2} + \sqrt{6})$ for $n = 3$ (three islands), $m_n = 1/4$ for $n = 4$ (four islands), $m_n = 1/(2\sqrt{2} + 2)$ for $n = 5$ (five islands), $m_n = (3 + \sqrt{7})^{-1}$ for $n = 6$ (six islands), $m_n = 1/(2 + \sqrt{2} + \sqrt{6})$ for $n = 7$ (seven islands), $m_n = 1/(2 + \sqrt{2} + \sqrt{6})$ for $n = 8$ (eight islands), $m_n = 1/6$ for $n = 9$ (nine islands).

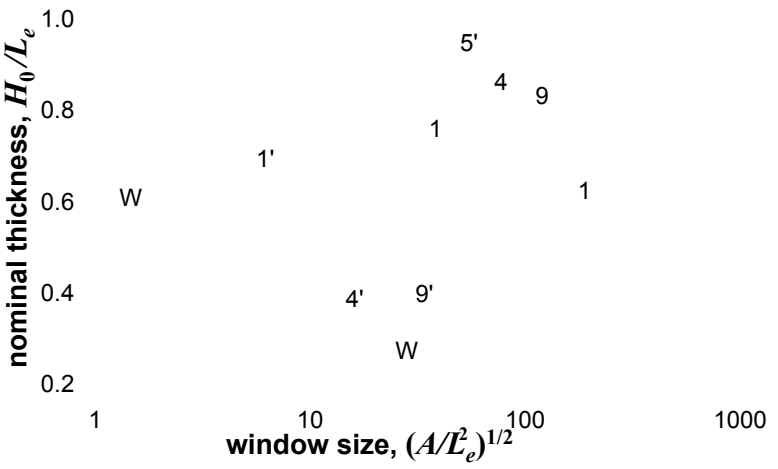

Figure 3: Plot of minimum energy configuration as a function of window size and nominal film thickness for the case $\nu = 0.3$, $\bar{l} = 0.1$, and $\bar{\gamma}_w = 0.5$. The elastic interaction energy between islands is neglected.

2.3 Areal Constraint Results and Discussion

The calculated minimum energy state amongst the zero, one, two, three, four, five, six, seven, eight, and nine-island configurations is plotted in Figure (3) versus nominal film thickness $\bar{H}_0 = H_0/L_e$ and window size $\bar{A}^{1/2} = (A/L_e^2)^{1/2}$. A typical value for Poisson's ratio of $\nu = 0.3$ is used, and the wetting constants of $\bar{l} = l/L_e = 0.1$ and $\bar{\gamma}_w = \gamma_w/\gamma = 0.5$ are chosen and retained throughout the investigation to maintain consistency with the previous analysis [69]. It is noted that these constants were selected somewhat arbitrarily, and while they might be determined empirically based on relevant features of the results, the expected order of magnitude values are sufficient for the current investigation. Similar features are observed for a wide range of values of $\bar{l}$ and $\bar{\gamma}_w$.

Figure (3) can be interpreted as the evolution of the minimum energy configuration as a given material system is deposited; for a given area, one follows the diagram upward towards a increasing amount of deposit meterial. The initial deposition forms a wetting layer with no islands, as is typical of Stranski-Krastanov growth, and provided the window size is large enough, greater than about $(A/L_e^2)^{1/2} = 2.4$, a critical thickness is reached where islands first become energetically favorable. Over a wide range of window sizes, the critical thickness is fairly uniform ranging

between $H_0/L_e = 0.32$ and 0.36. Wetting parameters were not refined to provide physically reasonable results, however it is instructive to provide a physical estimate of this thickness. Taking film modulus $M = 180$ GPa, surface energy density $\gamma = 1\text{J/m}^2$, and mismatch strain $\epsilon_0 = 4\%$, which are reasonable values for Ge and Si or similar semiconductor material systems, the epitaxial length scale is calculated as $L_e = 3.5$ nm. This implies a critical thickness for islanding in the range of $H_0 = 1.12$ nm to 1.26 nm which corresponds to a few monolayers of growth. The thickness can be adjusted to match experimental values by altering the parameters l and γ_w. It is noted that the model adopts a continuum viewpoint of the wetting layer thickness, whereas it would be more physically accurate to admit only discrete thicknesses as integer multiples of a monolayer thickness. Further work along these lines should certainly be pursued, however the continuum assumption is not so severe. On the length scale of this model, there is in fact a continuous reservoir for material in the form of adsorbed atoms (adatoms) atop the wetting layer. In order to alter this model to admit only discrete wetting layer thicknesses, it would likely prove necessary to include an adatom phase to account for an incomplete monolayer. In this context, the current model simply adopts the same constitutive behavior for the wetting layer and adatom phases. A more general model could be built to differentiate the two phases, however that is left for future work.

While two, three, six, seven, and eight-island configurations were considered in the calculation of Figure (3), they do not occur as minimum energy states. The possibility of these occurring as metastable states is addressed later. It is found that each of the one, four, five, and nine-island configurations occur as minimum energy states. Up to a point, configurations with a greater number of islands are favored at larger window sizes, but for very large windows a single island becomes favored. This implies that windows of modest size provide some resistance to coarsening. Without the areal constraint, it is well known that this model of Stranski-Krastanov growth suggests that a single large island is of lower energy than multiple small islands of the same total volume (*e.g.* [8]). This behavior is observed in Figure (3) in the case of a sufficiently large window size. It is also noted that window size is not the only fac-

tor that affects coarsening; the ratio of nominal film thickness to window size plays an important role. For instance, at a windows size of $(A/L_e^2)^{1/2} = 100$ coarsening occurs below a nominal film thickness of $H_0/L_e \approx 0.6$, but for $(A/L_e^2)^{1/2} = 60$ coarsening occurs below $H_0/L_e \approx 0.45$. For window sizes less than about $(A/L_e^2)^{1/2} = 40$, greater nominal film thickness promotes coarsening. For example, consider a windows size of $(A/L_e^2)^{1/2} \approx 45$. As the nominal film thickness is increased from zero Figure (3) indicates that up until approximately $H_0/L_e = 0.36$ all of the material will form in a wetting layer with no island formation (W). As the nominal film thickness is increased further, configuration (9) will become favorable. With further deposition the footprint of the nine islands increases in size until they touch ($9'$). With additional material deposition the system coarsens to configuration ($5'$) and then (4), followed by the four impinging islands ($4'$). Finally, at high nominal film thicknesses the system will favor the coalescence of all islands into a single island (1).

Jin *et al.* [3] investigated island formation on square mesas with mesa dimensions in the 1μm to 1.2μm range and found that for smaller mesa dimensions four islands located at the mesa corners were observed (4), while for the slightly larger mesa size a fifth island at the mesa center was also observed (5 of $5'$). Referring to Figure (3) this same trend is observed with the formation of a fifth island in the center of the growth window being favored as the window size increases. Kitajima *et al.* [2] investigated self-assembly of Ge islands on patterned silicon substrates by depositing material on raised square substrate mesas via molecular beam epitaxy. The experiment was repeated with square mesa dimensions of 500nm, 300nm, and 140nm. For the 500nm case a four island configuration was observed with one island at each corner of the mesa (configuration 4). For the 140nm case only a single island on the mesa top was observed (1 or $1'$). A strong correlation is found between the experimentally reported results and the trends predicted by Figure (3). For example, fixing the nominal film thickness at $H_0/L_e = 0.6$ and considering increasing window sizes from $(A/L_e^2)^{1/2} \approx 30$ to 100 the configuration changes from a single island (1) to four ($4'$). With further increase in window size the four islands no

longer impinge (4). This is followed by the five impinging islands (5′). For very large growth window dimensions the system transitions back to the single island case (1), which is consistent with the unbounded case.

It is important to note that the system will not necessarily reach its minimum energy state, as there are likely many metastable states that might be reached during the growth process. Furthermore, transitions between two states during deposition might not occur as indicated by Figure (3). For a transition to occur, there must be a kinetically admissible pathway that follows the restrictions set by the mode of mass transport, in this case either surface diffusion or condensation-evaporation. Unless there is an energetically favorable pathway, a given state may persist to a much larger nominal thickness than predicted by Figure (3). For example consider a slow rate of deposition on a window of size $(A/L_e^2)^{1/2} = 100$. Initially a wetting layer forms followed by a single island atop the wetting layer, as predicted by equilibrium. After a certain amount of growth, Figure (3) suggests the system will transform into a nine island configuration. However, this process most likely occurs with a large activation barrier. Determination of the activation barrier is a subject of future work, but it is sufficient to note that while island ripening and coalescence is commonly observed, the separation of a single island into two or more islands has not been observed either computationally or experimentally to the authors' knowledge. At high rates of deposition, multiple islands tend to nucleate followed by ripening or coalescence [4, 43]. Hence to achieve the the nine island configuration on a window size of $(A/L_e^2)^{1/2} = 100$, it is likely best to deposit material fairly quickly until the nominal thickness reaches an amount where that state is favored. Once deposition is stopped, ripening will occur. While it is possible that a metastable state will arise, it is more likely that the multiple island configuration will occur through ripening of many unstable islands than by the dissociation of a single island. Similarly, one might achieve a metastable state by depositing to a certain nominal thickness, annealing, and depositing additional material. For example with a window size of $(A/L_e^2)^{1/2} = 15$, one might grow to a thickness of $H_0/L_e \approx 0.4$ where a four island configuration is favored. After establishing this configuration with a sufficiently long

annealing step, one might resume deposition to a thickness where a single island is favored. Provided the activation barrier is large enough, the four island configuration could remain as a metastable state.

Given that metastable configurations are likely to occur and might even be desired to achieve arrangements of technological interest, it is useful to consider configurations that represent local energy minima. As the process of an island dissociating into two or more islands likely occurs with a large activation barrier, it is assumed that a small number of islands is always metastable relative to a larger number of islands. For example a system with two islands might spontaneously ripen into a single island, but it is less likely to transform into three of more islands. Accordingly, metastable configuration phase diagrams are constructed by considering only (a) zero and one island, (b) zero, one, and two islands, (c) zero through three islands, (d) zero through four islands, (e) zero through five islands, (f) zero through six islands, (g) zero through seven islands, and (h) zero through eight islands . Each of these cases is plotted in Figure (4).

While the cases of two and three islands do not appear as global energy minima, it is found that they may occur as configurations that resist coarsening. To understand the sequence of plots in Figure (4), consider the point $(A/L_e^2)^{1/2} = 35$ and $H_0/L_e = 0.5$ shown by the dots in Figure (4a) through Figure (4d) (the phase region occupied by the dot does not change as metastable configurations of more than four islands are included). The minimum energy configuration is $(4')$ in Figure (4d), which is also the case in Figure (3). This is the global minimum (considering a maximum of nine islands). In Figure (4c), configuration $(3')$ is the minimum energy configuration. It has a lower free energy than a zero, one, or two island configuration, but higher energy than the $(4')$ configuration. In Figure (4b), configuration (2) is the minimum energy configuration. While this configuration will not coarsen into a single island, the $(3')$ and $(4')$ configuration are more stable. Finally, the (1) configuration is the minimum energy state in Figure (4a), but the (2), $(3')$ and $(4')$ configurations are progressively more stable.

It is likely that certain configurations observed by Kitajima *et al.* [2] repre-

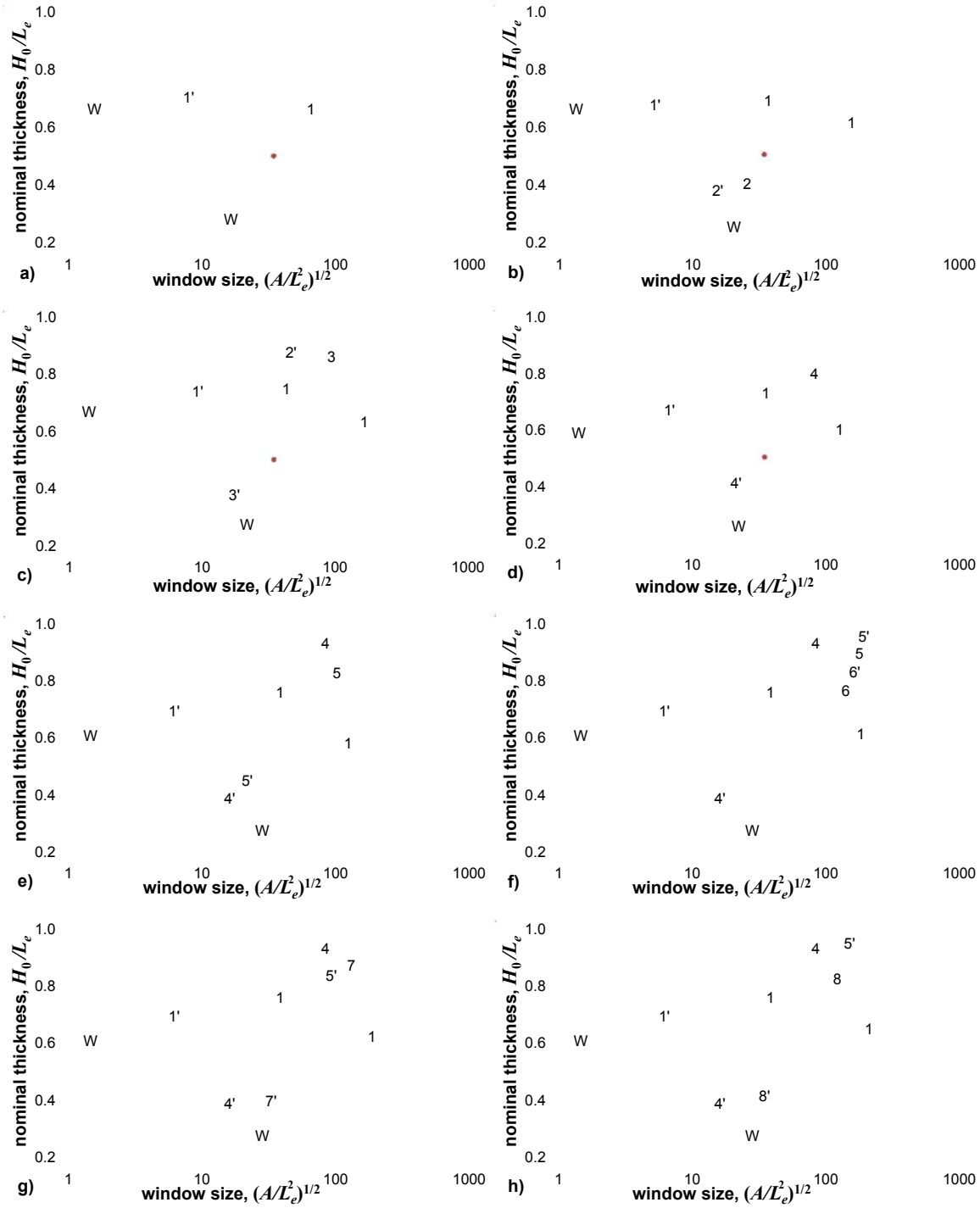

Figure 4: Minimum energy configuration when considering a) zero and one island, b) zero, one, and two islands, c) zero through three islands, d) zero through four islands, e) zero through five islands, f) zero through six islands, g) zero through seven islands, and h) zero through eight islands. These represent states that are stable with respect to coarsening. The dot in plots a) to d) corresponds to the point where $(A/L_e^2)^{1/2} = 35$ and $H_0/L_e = 0.5$.

sented such metastable states. For example for growth on a mesa of size 300nm, they observed a configuration of three tightly spaced islands in a triangular formation. The closely spaced three-island configuration corresponds to state $(3')$. While a direct correlation with Figure (4) is not possible because no attempt has been made to refine modeling constants, it was found that for a wide range of cases, the three island configuration never occurred as a global minimum. Typically a four island configuration is more stable as in Figure (4).

3 Arbitrary Island Morphology Kinetic Model

While the areal constraint analysis provides an excellent first step towards understanding the mechanisms governing nanoscale structure self assembly in epitaxial systems, it does have some important limitations. Chief among them is the reliance on a regular and strictly defined island profile. It is therefore of interest to obtain a better sense of favorable island shapes and morphologies using a kinetic simulation.

The model being considered for this portion of the investigation uses a second order approximation for the strain energy and surface free energy solutions needed to evaluate chemical potential across the film surface. The film and substrate surfaces are modeled using two dimensional truncated Fourier expansions, and the evolution of the film surface is carried out spectrally. This allows for a great deal of variation in island and substrate morphology, limited only by the resolution constraints brought about by the available computational resources. A two dimensional Fast Fourier Transform (2D-FFT) is used to switch between spacial coordinates and spectral coordinates. The evolution of the film is driven by the chemical potential profile such that material migrates from areas of high chemical potential to areas of lower chemical potential via a kinematically admissible pathway. That is to say, material cannot pass through areas of higher chemical potential in order to reach locations with a lower ultimate chemical potential. This model is therefore more closely analogous to a surface diffusion process than an evaporation-condensation process. The film/substrate interfacial energy is also considered and incorporated into the chemical potential calculation to ensure that the model respects the nature of that boundary, namely that the film surface cannot reasonably pass through the substrate surface. The complete and explicitly detailed derivation of the mathematical model developed here is shown in Appendix A. The system being considered is shown in Figure (5).

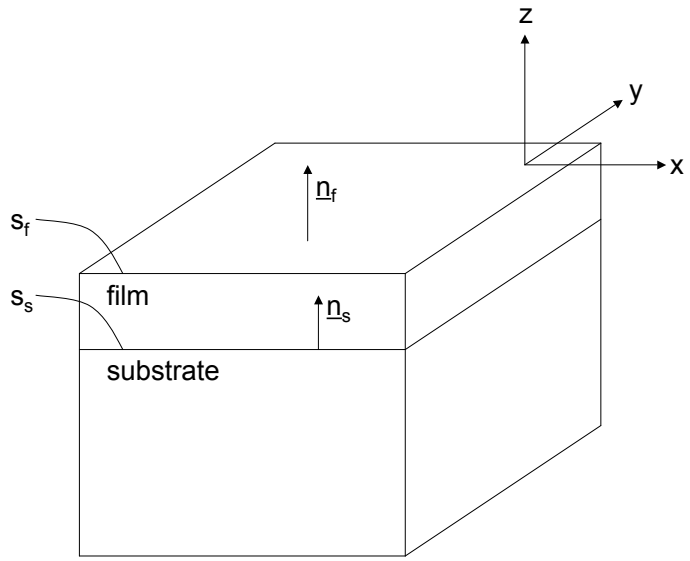

Figure 5: The system being considered.

The film surface profile can be expressed as the Fourier series

$$z_f(x,y) = \sum_{p,q=-N}^{N} a_{pq} e^{2\pi i(p\frac{x}{\lambda_x} + q\frac{y}{\lambda_y})} \tag{3.1}$$

and the substrate surface profile can be expressed as the Fourier series

$$z_s(x,y) = \sum_{p,q=-N}^{N} b_{pq} e^{2\pi i(p\frac{x}{\lambda_x} + q\frac{y}{\lambda_y})} \tag{3.2}$$

where N is order of the Fourier series representations, and a_{pq} and b_{pq} are the Fourier coefficients for the film and substrate, respectively. The values of these coefficients are required to be small, with the exception of the a_{00} and b_{00} terms which express the nominal film thickness.

3.1 Elastic Strain Energy

The elastic strain energy caused by the mismatch between the atomic lattice spacing of the film and substrate materials must be evaluated as part of the chemical potential of each location on the film surface. This elastic strain energy will drive

the film material to locations within the system that have lower elastic constraint between the film and the substrate. An example of this type of location could either be an less constrained substrate feature such as the edge of a raised mesa as shown for two dimensions as part of the earlier work [62]. The film material could also form a raised island structure in order to escape the constraint of the substrate vertically.

The film surface is traction free, with

$$\sigma_{ij} n_j^f = 0 \tag{3.3}$$

and the tractions on the substrate surface are induced by the difference between the stress fields of the film and substrate. This difference can be expressed as

$$[\![\sigma_{ij}]\!] n_j^s = (\sigma_{ij}^f - \sigma_{ij}^s) n_j^s = 0 \tag{3.4}$$

where the bracketed term denotes the field resulting from the difference between the film and substrate fields. The combined strain field can also be written as

$$[\![\epsilon_{ij}]\!](\delta_{jk} - n_j^s n_k^s) = \epsilon_{ik}^0 \tag{3.5}$$

where $(\delta_{jk} - n_j^s n_k^s)$ is the projection onto the substrate surface, and ϵ_{ik}^0 is the mismatch strain that results from the discontinuity in strain at the substrate/film interface.

The goal is to find an expression for the energy, U, as a function of the Fourier coefficients of the film and substrate, $U(a_{pq}, b_{pq})$, as an approximation for small slopes. This implies

$$\frac{a_{pq} p}{\lambda_x} \sim \frac{a_{pq} q}{\lambda_y} \sim \frac{b_{pq} p}{\lambda_x} \sim \frac{b_{pq} q}{\lambda_y} \sim \alpha \tag{3.6}$$

where α is small, with the exception of

$$a_{00}, b_{00} \sim O(1) \tag{3.7}$$

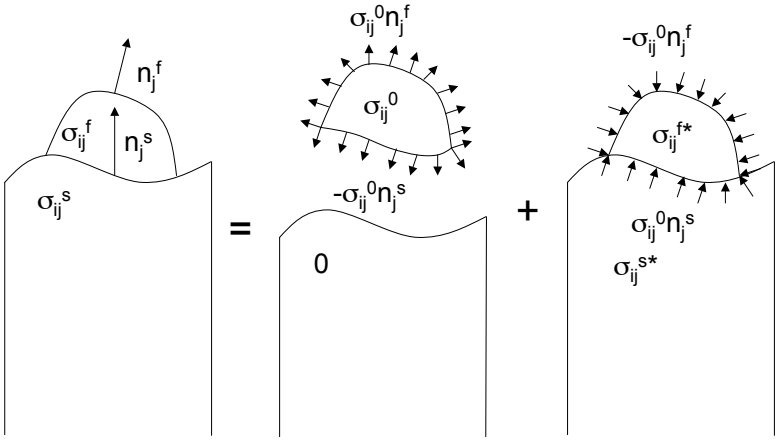

Figure 6: The elastic field superposition.

which is not small. b_{00} can be taken to be zero, while a_{00} controls the nominal film thickness.

A first order approximation would follow as

$$u \approx u + O(\alpha)^2, \qquad U \approx U + O(\alpha)^3. \tag{3.8}$$

For this investigation, a second order approximation is desired, with the displacement and energy terms governed respectively by

$$u \approx u + O(\alpha)^3, \qquad U \approx U + O(\alpha)^4 \tag{3.9}$$

where α is small. The elastic field can be represented by a superposition of a known field induced by mismatch between the film and substrate, and an unknown field due to certain applied forces, as shown in Figure (6), and as expressed by

The elastic field can be represented by a superposition of a known field induced by mismatch between the film and substrate, and an unknown field due to certain applied forces, as shown in Figure (6), and as expressed by

$$\sigma_{ij}^{f} = \sigma_{ij}^{0} + \sigma_{ij}^{f*} \tag{3.10}$$

and

$$\sigma_{ij}^{s} = \sigma_{ij}^{s*}. \tag{3.11}$$

On the film surface

$$\sigma_{ij}^{f*} n_j^f = -\sigma_{ij}^{0} n_j^f \tag{3.12}$$

while on the substrate surface

$$[\![\sigma_{ij}^{*}]\!] n_j^s = (\sigma_{ij}^{f*} - \sigma_{ij}^{s*}) n_j^s = -\sigma_{ij}^{0} n_j^s \tag{3.13}$$

with a strain field expressed as

$$[\![\epsilon_{ij}^{*}]\!](\delta_{jk} - n_j^s n_k^s) = 0 \tag{3.14}$$

and a displacement continuity constraint,

$$[\![u_i^{*}]\!] = 0 \tag{3.15}$$

or

$$(u_i^{*})^{+} = (u_i^{*})^{-} \tag{3.16}$$

The total strain energy of the system can be expressed as

$$
\begin{aligned}
U_{tot} &= \frac{1}{2}\int_{V_f}(\sigma_{ij}^0+\sigma_{ij}^*)(\epsilon_{ij}^0+\epsilon_{ij}^*)\,dV + \frac{1}{2}\int_{V_s}\sigma_{ij}^*\epsilon_{ij}^*\,dV \\
&= \frac{1}{2}\int_{V_f}\sigma_{ij}^0\epsilon_{ij}^0\,dV + \int_{V_f}\sigma_{ij}^0\epsilon_{ij}^*\,dV + \frac{1}{2}\int_{V_f}\sigma_{ij}^*\epsilon_{ij}^*\,dV + \frac{1}{2}\int_{V_s}\sigma_{ij}^*\epsilon_{ij}^*\,dV \\
&= w^0V_f + \int_{V_f}(\sigma_{ij}^0u_i^*)_{,j}\,dV + \frac{1}{2}\int_{V_f}(\sigma_{ij}^*u_i^*)_{,j}\,dV + \frac{1}{2}\int_{V_s}(\sigma_{ij}^*u_i^*)_{,j}\,dV \\
&= w^0V_f + \int_{s_f}(\sigma_{ij}^0n_j^fu_i^* + \frac{1}{2}\sigma_{ij}^*n_j^fu_i^*)\,dA \\
&\qquad + \int_{s_s}(-\sigma_{ij}^0n_j^su_i^* - \frac{1}{2}\sigma_{ij}^{f*}n_j^su_i^* + \frac{1}{2}\sigma_{ij}^{s*}n_j^su_i^*)\,dA. \qquad (3.17)
\end{aligned}
$$

Substituting Equations (A.12) and (A.13) into Equation (A.17) yields

$$
U_{tot} = w^0V_f + \frac{1}{2}\int_{s_f}\sigma_{ij}^0n_j^fu_i^*\,dA - \frac{1}{2}\int_{s_s}\sigma_{ij}^0n_j^su_i^*\,dA. \qquad (3.18)
$$

For this solution, the displacement field u_i^*, periodic in x and y, is needed. Papkovitch-Neuber potentials will be utilized.

From the linearly elastic stress-displacment relationship

$$
\sigma_{ij} = \lambda u_{k,k}\delta_{ij} + \mu(u_{i,j}+u_{j,i}) \qquad (3.19)
$$

and equilibrium condition

$$
\sigma_{ij,j} = 0 \qquad (3.20)
$$

the constraint

$$
(\lambda+\mu)u_{i,ij} + \mu u_{j,ii} = 0 \qquad (3.21)
$$

can be determined. Applying the Papkovitch-Neuber potentials yields

$$
u_i = \phi_i - \frac{1}{4(1-\nu)}(\phi_0 + x - j\phi_j)_{,i}. \qquad (3.22)
$$

Working through the solution for the potential functions, shown in Appendix B, it is found that

$$
\begin{aligned}
\phi_0^f &= \sum_{\substack{p,q=-\infty \\ (p,q)\neq(0,0)}}^{\infty} \Big\{ A_{0pq} e^{2\pi z\sqrt{\frac{p^2}{\lambda_x}+\frac{q^2}{\lambda_y}}} + B_{0pq} e^{-2\pi z\sqrt{\frac{p^2}{\lambda_x}+\frac{q^2}{\lambda_y}}} \\
&+ \frac{\frac{i}{4} A_{1pq} e^{2\pi z\sqrt{\frac{p^2}{\lambda_x}+\frac{q^2}{\lambda_y}}} \lambda_x \lambda_y^2 p \left(-1 + 4\pi z\sqrt{\frac{p^2}{\lambda_x}+\frac{q^2}{\lambda_y}}\right)}{\pi\left(\lambda_y^2 p^2 + \lambda_x^2 q^2\right)} \\
&+ \frac{\frac{-i}{4} B_{1pq} \lambda_x \lambda_y^2 p \left(1 + 4\pi z\sqrt{\frac{p^2}{\lambda_x}+\frac{q^2}{\lambda_y}}\right)}{e^{2\pi z\sqrt{\frac{p^2}{\lambda_x}+\frac{q^2}{\lambda_y}}} \pi\left(\lambda_y^2 p^2 + \lambda_x^2 q^2\right)} \\
&+ \frac{\frac{i}{4} A_{2pq} e^{2\pi z\sqrt{\frac{p^2}{\lambda_x}+\frac{q^2}{\lambda_y}}} \lambda_x^2 \lambda_y q \left(-1 + 4\pi z\sqrt{\frac{p^2}{\lambda_x}+\frac{q^2}{\lambda_y}}\right)}{\pi\left(\lambda_y^2 p^2 + \lambda_x^2 q^2\right)} \\
&+ \frac{\frac{-i}{4} B_{2pq} \lambda_x^2 \lambda_y q \left(1 + 4\pi z\sqrt{\frac{p^2}{\lambda_x}+\frac{q^2}{\lambda_y}}\right)}{e^{2\pi z\sqrt{\frac{p^2}{\lambda_x}+\frac{q^2}{\lambda_y}}} \pi\left(\lambda_y^2 p^2 + \lambda_x^2 q^2\right)} \\
&- x\left(A_{1pq} e^{2\pi z\sqrt{\frac{p^2}{\lambda_x}+\frac{q^2}{\lambda_y}}} + B_{1pq} e^{-2\pi z\sqrt{\frac{p^2}{\lambda_x}+\frac{q^2}{\lambda_y}}}\right) \\
&- y\left(A_{2pq} e^{2\pi z\sqrt{\frac{p^2}{\lambda_x}+\frac{q^2}{\lambda_y}}} + B_{2pq} e^{-2\pi z\sqrt{\frac{p^2}{\lambda_x}+\frac{q^2}{\lambda_y}}}\right) \Big\} e^{2\pi i\left(p\frac{x}{\lambda_x}+q\frac{y}{\lambda_y}\right)}, \qquad (3.23)
\end{aligned}
$$

$$
\phi_x^f = \sum_{\substack{p,q=-\infty \\ (p,q)\neq(0,0)}}^{\infty} \Big\{ A_{1pq} e^{2\pi z\sqrt{\frac{p^2}{\lambda_x}+\frac{q^2}{\lambda_y}}} + B_{1pq} e^{-2\pi z\sqrt{\frac{p^2}{\lambda_x}+\frac{q^2}{\lambda_y}}} \Big\} e^{2\pi i\left(p\frac{x}{\lambda_x}+q\frac{y}{\lambda_y}\right)}, \qquad (3.24)
$$

$$
\phi_y^f = \sum_{\substack{p,q=-\infty \\ (p,q)\neq(0,0)}}^{\infty} \Big\{ A_{2pq} e^{2\pi z\sqrt{\frac{p^2}{\lambda_x}+\frac{q^2}{\lambda_y}}} + B_{2pq} e^{-2\pi z\sqrt{\frac{p^2}{\lambda_x}+\frac{q^2}{\lambda_y}}} \Big\} e^{2\pi i\left(p\frac{x}{\lambda_x}+q\frac{y}{\lambda_y}\right)}, \qquad (3.25)
$$

$$
\phi_z^f = \sum_{\substack{p,q=-\infty \\ (p,q)\neq(0,0)}}^{\infty} \Big\{ A_{3pq} e^{2\pi z\sqrt{\frac{p^2}{\lambda_x}+\frac{q^2}{\lambda_y}}} + B_{3pq} e^{-2\pi z\sqrt{\frac{p^2}{\lambda_x}+\frac{q^2}{\lambda_y}}} \Big\} e^{2\pi i\left(p\frac{x}{\lambda_x}+q\frac{y}{\lambda_y}\right)}, \qquad (3.26)
$$

$$
\begin{aligned}
\phi_0^s &= \sum_{\substack{p,q=-\infty \\ (p,q)\neq(0,0)}}^{\infty} \Big\{ C_{0pq} e^{2\pi z\sqrt{\frac{p^2}{\lambda_x}+\frac{q^2}{\lambda_y}}} \\
&+ \frac{\frac{i}{4} C_{1pq} e^{2\pi z\sqrt{\frac{p^2}{\lambda_x}+\frac{q^2}{\lambda_y}}} \lambda_x \lambda_y^2 p \left(-1 + 4\pi z\sqrt{\frac{p^2}{\lambda_x}+\frac{q^2}{\lambda_y}}\right)}{\pi\left(\lambda_y^2 p^2 + \lambda_x^2 q^2\right)} \\
&+ \frac{\frac{i}{4} C_{2pq} e^{2\pi z\sqrt{\frac{p^2}{\lambda_x}+\frac{q^2}{\lambda_y}}} \lambda_x^2 \lambda_y q \left(-1 + 4\pi z\sqrt{\frac{p^2}{\lambda_x}+\frac{q^2}{\lambda_y}}\right)}{\pi\left(\lambda_y^2 p^2 + \lambda_x^2 q^2\right)} \\
&- x C_{1pq} e^{2\pi z\sqrt{\frac{p^2}{\lambda_x}+\frac{q^2}{\lambda_y}}} - y C_{2pq} e^{2\pi z\sqrt{\frac{p^2}{\lambda_x}+\frac{q^2}{\lambda_y}}} \Big\} e^{2\pi i\left(p\frac{x}{\lambda_x}+q\frac{y}{\lambda_y}\right)}, \qquad (3.27)
\end{aligned}
$$

$$
\phi_x^s = \sum_{\substack{p,q=-\infty \\ (p,q)\neq(0,0)}}^{\infty} \Big\{ C_{1pq} e^{2\pi z\sqrt{\frac{p^2}{\lambda_x}+\frac{q^2}{\lambda_y}}} \Big\} e^{2\pi i\left(p\frac{x}{\lambda_x}+q\frac{y}{\lambda_y}\right)}, \qquad (3.28)
$$

$$
\phi_y^s = \sum_{\substack{p,q=-\infty \\ (p,q)\neq(0,0)}}^{\infty} \Big\{ C_{2pq} e^{2\pi z\sqrt{\frac{p^2}{\lambda_x}+\frac{q^2}{\lambda_y}}} \Big\} e^{2\pi i\left(p\frac{x}{\lambda_x}+q\frac{y}{\lambda_y}\right)}, \qquad (3.29)
$$

and

$$
\phi_z^s = \sum_{\substack{p,q=-\infty \\ (p,q)\neq(0,0)}}^{\infty} \Big\{ C_{3pq} e^{2\pi z\sqrt{\frac{p^2}{\lambda_x}+\frac{q^2}{\lambda_y}}} \Big\} e^{2\pi i\left(p\frac{x}{\lambda_x}+q\frac{y}{\lambda_y}\right)}. \qquad (3.30)
$$

The expressions for all coefficients are provided in Appendix C.

Therefore, solving for the total strain energy of the system given in Equation (A.18) yields

$$
\begin{aligned}
U_{tot} &= \frac{\sqrt{\lambda_x\lambda_y}^3\pi\sigma_0^2\left(1-2\nu\right)^2}{\mu\left(1-\nu\right)}\Bigg\{\frac{\bar{a}_{00}}{2\pi\left(1+\nu\right)} \\
&- \sum_{\substack{r,s=-\infty \\ (r,s)\neq(0,0)}}^{\infty}\sqrt{R^2+S^2}\left(\bar{a}_{(-r,-s)}-\frac{\bar{b}_{(-r,-s)}}{e^{2\bar{a}_{00}\pi\sqrt{R^2+S^2}}}\right)\left(\bar{a}_{(r,s)}-\frac{\bar{b}_{(r,s)}}{e^{2\bar{a}_{00}\pi\sqrt{R^2+S^2}}}\right) \\
&+ 2\pi\sum_{\substack{r,s=-\infty \\ (r,s)\neq(0,0)}}^{\infty}\sum_{\substack{p,q=-\infty \\ (p,q)\neq(0,0)\neq(r,s)}}^{\infty}\sqrt{P^2+Q^2}\left(\bar{a}_{(p,q)}-\frac{\bar{b}_{(p,q)}}{e^{2\bar{a}_{00}\pi\sqrt{P^2+Q^2}}}\right)\Big(2\sqrt{R^2+S^2}\left(1\right. \\
&- \left.\frac{\left(1-\nu\right)\left(PS-QR\right)^2}{\left(P^2+Q^2\right)\left(R^2+S^2\right)}\right)\bar{a}_{(r-p,s-q)}\left(\bar{a}_{(-r,-s)}-\frac{\bar{b}_{(-r,-s)}}{e^{2\bar{a}_{00}\pi\sqrt{R^2+S^2}}}\right) \\
&- \sqrt{P^2+Q^2}\left(\bar{a}_{(-r,-s)}\bar{a}_{(r-p,s-q)}-\frac{\bar{b}_{(-r,-s)}\bar{b}_{(r-p,s-q)}}{e^{2\bar{a}_{00}\pi\sqrt{P^2+Q^2}}}\right)\Big)\Bigg\} \qquad (3.31)
\end{aligned}
$$

where $P=p\sqrt{\lambda_y/\lambda_x}$, $Q=q\sqrt{\lambda_x/\lambda_y}$, $R=r\sqrt{\lambda_y/\lambda_x}$, and $S=s\sqrt{\lambda_x/\lambda_y}$.

Normalizing the total strain energy yields

$$\bar{U}_{tot}=U_{tot}\frac{\mu\left(1-\nu\right)}{\sqrt{\lambda_x\lambda_y}^3\pi\sigma_0^2\left(1-2\nu\right)^2}. \qquad (3.32)$$

where μ is the relevant elastic modulus of the system, ν is Poisson's ratio, σ_0 is the epitaxial mismatch in the system, and λ_x and λ_y are the wavelengths of the periodic cell prior to normalization. The elastic properties of the film and substrate are taken to be the same. From the normalized total strain energy of the system defined as a function of the film surface Fourier coefficients, $U_{tot}=U_{tot}\left(a_{pq}\right)$, the change in energy with respect to time can be expressed as

$$\frac{d\bar{U}_{tot}}{dt}=\int_0^1\int_0^1\bar{\chi}\frac{d\bar{z}_f}{dt}\,d\bar{x}\,d\bar{y}. \qquad (3.33)$$

where

$$\bar{\chi}=\frac{M\left(1-\nu\right)}{\pi\sigma_0^2\left(1-2\nu\right)^2}\chi=\sum_{m,n=-\infty}^{\infty}\bar{X}_{mn}e^{2\pi i(m\bar{x}+n\bar{y})} \qquad (3.34)$$

is the normalized chemical potential with complex Fourier coefficients $\bar{X}\left(p,q\right)$.

Taking the function $\bar{U}_{tot}$ given in Equation (A.103),

$$\begin{aligned}\frac{d\bar{U}_{tot}}{dt} &= \sum_{m,n=-\infty}^{\infty} \frac{d\bar{U}_{tot}}{d\bar{a}_{mn}} \frac{d\bar{a}_{mn}}{dt} \\ &= \sum_{m,n=-\infty}^{\infty} \frac{d\bar{a}_{mn}}{dt} \int_0^1 \int_0^1 \left\{ \bar{\chi} e^{2\pi i(m\bar{x}+n\bar{y})} \right\} d\bar{x}\, d\bar{y} \\ &= \sum_{m,n=-\infty}^{\infty} \bar{X}(-m,-n) \frac{d\bar{a}_{mn}}{dt}. \end{aligned} \tag{3.35}$$

where

$$\bar{a}_{m,n} = \frac{a_{m,n}}{\sqrt{\lambda_x \lambda_y}}. \tag{3.36}$$

Therefore

$$\bar{X}(-m,-n) = \frac{d\bar{U}_{tot}}{d\bar{a}(m,n)}. \tag{3.37}$$

Since the chemical potential is real, as are the film and substrate surfaces,

$$\bar{X}(m,n) = \bar{X}_R(m,n) + i\bar{X}_I(m,n) \tag{3.38}$$

$$\begin{gathered} \bar{X}_I(-m,n) = -\bar{X}_I(m,-n) \\ \bar{X}_I(-m,-n) = -\bar{X}_I(m,n) \\ \bar{X}_R(-m,n) = \bar{X}_R(m,-n) \\ \bar{X}_R(-m,-n) = \bar{X}_R(m,n) \\ \bar{X}_I(0,0) = 0. \end{gathered} \tag{3.39}$$

From $\bar{U}_{tot} = \bar{U}_{tot}(\bar{a}_{pq}) = \bar{U}_{tot}(\bar{a}_R(p,q), \bar{a}_I(p,q))$ and the inverse Fourier transform and the relations found in Equations (3.39),

$$\frac{d\bar{U}_{tot}}{d\bar{a}_R(p,q)} = \int_0^1 \int_0^1 \bar{\chi}(x,y) \cos 2\pi i(p\bar{x}+q\bar{y})\, d\bar{x}\, d\bar{y} = \frac{\bar{X}_R(p,q) + \bar{X}_R(-p,-q)}{2} \tag{3.40}$$

and

$$\frac{d\bar{U}_{tot}}{d\bar{a}_I(p,q)} = \int_0^1 \int_0^1 -\bar{\chi}(x,y) \sin 2\pi i(p\bar{x}+q\bar{y})\, d\bar{x}\, d\bar{y} = \frac{\bar{X}_I(p,q) - \bar{X}_I(-p,-q)}{2}. \tag{3.41}$$

From Equations (3.39), (3.40), and (3.41) it is concluded that

$$\bar{X}_R(p,q) = \frac{d\bar{U}_{tot}}{d\bar{a}_R(p,q)} \tag{3.42}$$

and

$$\bar{X}_I(p,q) = \frac{d\bar{U}_{tot}}{d\bar{a}_I(p,q)}. \tag{3.43}$$

3.2 Surface Free Energy

There is an energy associated with the formation of any free surface in a system. This surface free energy will drive a system towards the configuration that has the lowest possible surface area. In the case of a freely suspended system, this would be the configuration with the lowest surface to volume ratio; namely a sphere. In the case of a film that is constrained to a substrate, the configuration with the lowest surface area is that of a flat film. This differs from the freely suspended case in that the bottom side of the film interfaces with the upper surface of the substrate, eliminating the surface free energy of those two surfaces (and introducing an interfacial energy in their place, as discussed later).

The contribution of the surface energy to the chemical potential must also be considered. In the interest of simplicity, the case where the surface energy density, γ, is constant and isotropic is considered. The normalized surface free energy can then be expressed as

$$\begin{aligned}\overline{\gamma S} &= \frac{\mu(1-\nu)\gamma}{\sqrt{\lambda_x\lambda_y}\pi\sigma_0^2(1-2\nu)^2}\Big(1+2\pi^2\sum_{p,q=-\infty}^{\infty}\big[\bar{a}_R(-p,-q)\bar{a}_R(p,q) \\ &\quad -\bar{a}_I(-p,-q)\bar{a}_I(p,q)\big]\big(\frac{\lambda_y}{\lambda_x}p^2+\frac{\lambda_x}{\lambda_y}q^2\big)\Big).\end{aligned} \tag{3.44}$$

The derivatives of the normalized surface energy with respect to the real and imaginary surface Fourier coefficients can then be evaluated,

$$\frac{\overline{\gamma S}}{d\bar{a}_R(m,n)} = \frac{4\mu(1-\nu)\gamma\pi}{\sqrt{\lambda_x\lambda_y}\sigma_0^2(1-2\nu)^2}\big(\frac{\lambda_y}{\lambda_x}m^2 + \frac{\lambda_x}{\lambda_y}n^2\big)\bar{a}_R(-m,-n) \tag{3.45}$$

and

$$\frac{\overline{\gamma S}}{d\bar{a}_I(m,n)} = \frac{-4\mu(1-\nu)\gamma\pi}{\sqrt{\lambda_x\lambda_y}\sigma_0^2(1-2\nu)^2}\big(\frac{\lambda_y}{\lambda_x}m^2 + \frac{\lambda_x}{\lambda_y}n^2\big)\bar{a}_I(-m,-n). \tag{3.46}$$

It is further noted that the mismatch stress, σ_0, can be expressed in terms of more readily useful mismatch strain, ϵ_0, as per the constitutive relation

$$\sigma_0 = \frac{\mu(1-\nu)}{(1-2\nu)^2}\epsilon_0. \tag{3.47}$$

Equations (3.45) and (3.46) can then be expressed in terms of the mismatch strain,

$$\frac{\overline{\gamma S}}{d\bar{a}_R(m,n)} = \frac{4(1-2\nu)^2\gamma\pi}{\sqrt{\lambda_x\lambda_y}\mu(1-\nu)\epsilon_0^2}\big(\frac{\lambda_y}{\lambda_x}m^2 + \frac{\lambda_x}{\lambda_y}n^2\big)\bar{a}_R(-m,-n) \tag{3.48}$$

and

$$\frac{\overline{\gamma S}}{d\bar{a}_I(m,n)} = \frac{4(1-2\nu)^2\gamma\pi}{\sqrt{\lambda_x\lambda_y}\mu(1-\nu)\epsilon_0^2}\big(\frac{\lambda_y}{\lambda_x}m^2 + \frac{\lambda_x}{\lambda_y}n^2\big)\bar{a}_I(-m,-n). \tag{3.49}$$

3.3 Combined Elastic Strain and Surface Free Energy

Having determined the form of the elastic strain energy and surface free energy of the film/substrate system, it is next necessary to combine the two to find the total chemical potential which will drive the evolution of the film. It is the competition between these two energies that can result in the formation of stable island configurations. While the strain energy would favor a system with film material as completely removed from the substrate as possible, the high aspect ratio of such configurations would result in large increases in free surface area which would be opposed by the surface free energy. It is only when these two energies come into

balance that equilibrium will be achieved and system evolution will stabilize. It is really very Zen.

The form of the chemical potential coefficients can then be expanded to include the surface free energy:

$$\bar{X}_R(p,q) = \frac{d\bar{U}_{tot}}{d\bar{a}_R(p,q)} + \frac{\overline{\gamma S}}{d\bar{a}_R(p,q)} \tag{3.50}$$

and

$$\bar{X}_I(p,q) = \frac{d\bar{U}_{tot}}{d\bar{a}_I(p,q)} + \frac{\overline{\gamma S}}{d\bar{a}_I(p,q)}. \tag{3.51}$$

This can in turn be expanded to

$$\bar{X}_R(p,q) = \frac{d\bar{U}_{tot}}{d\bar{a}_R(p,q)} + \bar{L^*}\big(\frac{\lambda_y}{\lambda_x}m^2 + \frac{\lambda_x}{\lambda_y}n^2\big)\bar{a}_R(-m,-n) \tag{3.52}$$

and

$$\bar{X}_I(p,q) = \frac{d\bar{U}_{tot}}{d\bar{a}_I(p,q)} + \bar{L^*}\big(\frac{\lambda_y}{\lambda_x}m^2 + \frac{\lambda_x}{\lambda_y}n^2\big)\bar{a}_I(-m,-n) \tag{3.53}$$

where

$$\bar{L^*} = \frac{4(1-2\nu)^2\gamma\pi}{\sqrt{\lambda_x\lambda_y}\mu(1-\nu)\epsilon_0^2}. \tag{3.54}$$

The normalized characteristic length, $\bar{L^*}$, specifies the balance point between surface free energy and elastic strain energy. For example, a higher value of $\bar{L^*}$ could imply that either the surface energy density, γ, has increased, or else the mismatch strain, ϵ_0, has been reduced, in either case leading to an increased influence of surface free energy over elastic strain energy. Inversely, a decrease in $\bar{L^*}$ could imply a drop in surface energy density, or an increase in mismatch strain, in both cases resulting in an increased importance of elastic strain energy over surface free energy. By comparing the behavior and response of a system to a range of $\bar{L^*}$ values, the relative effects of surface free energy and elastic strain energy can be evaluated and analyzed.

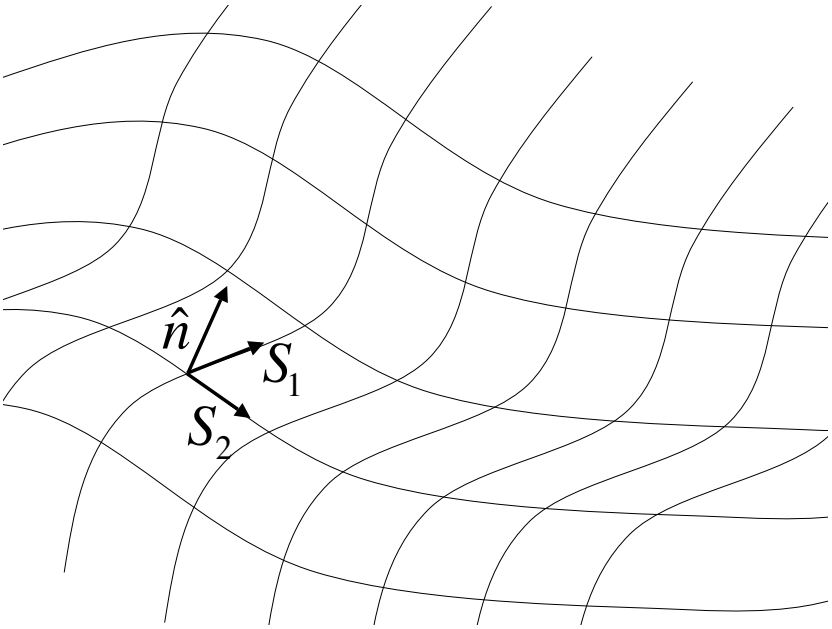

Figure 7: An orthogonal system on the film surface.

To determine the relationship between chemical potential and surface velocity, an orthogonal system on the film surface (S_1, S_2) is selected, including the normal to the film surface $(\hat{n})$, as shown in Figure (7).

The directions S_1 and S_2 are selected such that

$$S_1 = S_1(x, z_f) \tag{3.55}$$

and

$$S_2 = S_2(y, z_f). \tag{3.56}$$

From the Pythagorean theorem

$$\frac{dS_1}{dx} = \sqrt{\left(\frac{dz_f}{dx}\right)^2 + \left(\frac{dx}{dx}\right)^2} = \sqrt{\left(\frac{dz_f}{dx}\right)^2 + 1} \tag{3.57}$$

and similarly

$$\frac{dS_2}{dy} = \sqrt{\left(\frac{dz_f}{dy}\right)^2 + \left(\frac{dy}{dy}\right)^2} = \sqrt{\left(\frac{dz_f}{dy}\right)^2 + 1}. \tag{3.58}$$

The film surface is defined by $z_f = z_f(x, y)$, therefore the normal to the film surface is

$$\hat{n} = \frac{\nabla z_f}{|\nabla z_f|} = \frac{\left(\frac{dz_f}{dx}, \frac{dz_f}{dy}, 1\right)}{\sqrt{\left(\frac{dz_f}{dx}\right)^2 + \left(\frac{dz_f}{dy}\right)^2 + 1}} \tag{3.59}$$

The film surface velocity in the normal direction is given by

$$\begin{aligned} v_n &= M_s \nabla_s^2 \chi \\ &= M_s \left\{ \frac{\partial^2 \chi}{\partial x^2} \left(\frac{1}{\left(\frac{dz_f}{dx}\right)^2 + 1} \right) + \frac{\partial^2 \chi}{\partial y^2} \left(\frac{1}{\left(\frac{dz_f}{dy}\right)^2 + 1} \right) \right\} \end{aligned} \tag{3.60}$$

where M_s is the surface mobility coefficient.

The component of the surface velocity in the vertical direction is

$$v_z = M_s \left\{ \frac{\partial^2 \chi}{\partial x^2} + \frac{\partial^2 \chi}{\partial y^2} \right\} + O(\alpha)^3. \tag{3.61}$$

Conducting the same normalization procedure as used previously yields

$$\frac{d\bar{z}_f}{d\bar{t}} = \left(\frac{\lambda_y}{\lambda_x} \frac{d^2 \bar{\chi}}{d\bar{x}^2} + \frac{\lambda_x}{\lambda_y} \frac{d^2 \bar{\chi}}{d\bar{y}^2} \right) \tag{3.62}$$

where

$$\bar{t} = \frac{t}{\tau}. \tag{3.63}$$

and the time normalization factor is

$$\tau = \frac{(1 - 2\nu)^2 (\lambda_x \lambda_y)^{\frac{3}{2}}}{M_s \mu (1 - \nu) \pi \epsilon_0^2}. \tag{3.64}$$

The required second derivative terms appearing in Equation (3.62) can be evaluated as

$$\begin{aligned}\frac{d^2\bar{\chi}}{d\bar{x}^2} &= 2\sum_{m=1}^{NN} 4M^2\pi^2\big(\bar{X}_I(m,0)\sin 2M\pi\bar{x} - \bar{X}_R(m,0)\cos 2M\pi\bar{x}\big) \\ &+ 2\sum_{m,n=1}^{NN} 4M^2\pi^2\big(\bar{X}_I(m,-n)\sin 2\pi(M\bar{x}-N\bar{y}) + \bar{X}_I(m,n)\sin 2\pi(M\bar{x}+N\bar{y}) \\ &\quad -\bar{X}_R(m,-n)\cos 2\pi(M\bar{x}-N\bar{y}) - \bar{X}_R(m,n)\cos 2\pi(M\bar{x}+N\bar{y})\big) \qquad (3.65)\end{aligned}$$

and

$$\begin{aligned}\frac{d^2\bar{\chi}}{d\bar{y}^2} &= 2\sum_{n=1}^{NN} 4N^2\pi^2\big(\bar{X}_I(0,n)\sin 2N\pi\bar{y} - \bar{X}_R(0,n)\cos 2N\pi\bar{y}\big) \\ &+ 2\sum_{m,n=1}^{NN} 4N^2\pi^2\big(\bar{X}_I(m,-n)\sin 2\pi(M\bar{x}-N\bar{y}) + \bar{X}_I(m,n)\sin 2\pi(M\bar{x}+N\bar{y}) \\ &\quad -\bar{X}_R(m,-n)\cos 2\pi(M\bar{x}-N\bar{y}) - \bar{X}_R(m,n)\cos 2\pi(M\bar{x}+N\bar{y})\big). \qquad (3.66)\end{aligned}$$

Substituting Equations (3.65) and (3.66) into Equation (3.62) yields

$$\begin{aligned}\frac{d\bar{z}_f}{d\bar{t}} &= \left(\frac{\lambda_y}{\lambda_x}\frac{d^2\bar{\chi}}{d\bar{x}^2} + \frac{\lambda_x}{\lambda_y}\frac{d^2\bar{\chi}}{d\bar{y}^2}\right) \\ &= 2\sum_{m=1}^{NN} 4\frac{\lambda_y}{\lambda_x}M^2\pi^2\big(\bar{X}_I(m,0)\sin 2M\pi\bar{x} - \bar{X}_R(m,0)\cos 2M\pi\bar{x}\big) \\ &+ 2\sum_{n=1}^{NN} 4\frac{\lambda_x}{\lambda_y}N^2\pi^2\big(\bar{X}_I(0,n)\sin 2\frac{\lambda_x}{\lambda_y}N\pi\bar{y} - \bar{X}_R(0,n)\cos 2N\pi\bar{y}\big) \\ &+ 2\sum_{m,n=1}^{NN} \frac{4(\lambda_y^2M^2+\lambda_x^2N^2)\pi^2}{\lambda_x\lambda_y}\big\{ -\bar{X}_R(m,-n)\cos 2\pi(M\bar{x}-N\bar{y}) \\ &\qquad -\bar{X}_R(m,n)\cos 2\pi(M\bar{x}+N\bar{y}) \\ &\qquad +\bar{X}_I(m,-n)\sin 2\pi(M\bar{x}-N\bar{y}) \\ &\qquad +\bar{X}_I(m,n)\sin 2\pi(M\bar{x}+N\bar{y})\big\}. \qquad (3.67)\end{aligned}$$

The vertical velocity of the film surface can also be evaluated as the time derivative of the Fourier expansion given in Equation (3.1)

$$
\begin{aligned}
\frac{d\bar{z}_f}{d\bar{t}} &= \frac{\bar{a}_R(0,0)}{d\bar{t}} \\
&+ 2\sum_{n=1}^{NN}\left[\frac{\bar{a}_R(0,n)}{d\bar{t}}\cos 2n\pi\bar{y} - \frac{\bar{a}_I(0,n)}{d\bar{t}}\sin 2n\pi\bar{y}\right] \\
&+ 2\sum_{m=1}^{NN}\left[\frac{\bar{a}_R(m,0)}{d\bar{t}}\cos 2m\pi\bar{x} - \frac{\bar{a}_I(m,0)}{d\bar{t}}\sin 2m\pi\bar{x}\right] \\
&+ 2\sum_{m,n=1}^{NN}\Big\{\frac{\bar{a}_R(m,-n)}{d\bar{t}}\cos 2\pi(M\bar{x}-N\bar{y}) \\
&\qquad + \frac{\bar{a}_R(m,n)}{d\bar{t}}\cos 2\pi(M\bar{x}+N\bar{y}) \\
&\qquad - \frac{\bar{a}_I(m,-n)}{d\bar{t}}\sin 2\pi(M\bar{x}-N\bar{y}) \\
&\qquad - \frac{\bar{a}_I(m,n)}{d\bar{t}}\sin 2\pi(M\bar{x}+N\bar{y})\Big\}. \quad (3.68)
\end{aligned}
$$

By comparing the terms in Equations (3.67) and (3.68) it is determined that

$$\frac{\bar{a}_R(m,n)}{d\bar{t}} = -\frac{4(\lambda_y^2M^2+\lambda_x^2N^2)\pi^2}{\lambda_x\lambda_y}\bar{X}_R(m,n) \quad (3.69)$$

and

$$\frac{\bar{a}_I(m,n)}{d\bar{t}} = -\frac{4(\lambda_y^2M^2+\lambda_x^2N^2)\pi^2}{\lambda_x\lambda_y}\bar{X}_I(m,n). \quad (3.70)$$

The evolution of the film can then be conducted spectrally using the results in Equations (3.69) and (3.70) along with a desired time stepping routine.

3.4 Film/Substrate Interfacial Interaction Energy

In order to insure that the film evolution responds appropriately to the substrate surface, and a wetting layer typical for SK growth is maintained, a film/substrate interface interaction contribution to the chemical potential is also considered. The model employed to account for this effect was reported previously [7, 57–59]. The energy density of the film and substrate interface is first taken as

$$g(z_f) = \frac{g_0 l^p}{(z_f - z_s + l)^p} \tag{3.71}$$

where g_0 and l are material properties. The exponent term p varies depending on the interaction mechanism being considered [7, 57–59].

The contribution of this interaction energy to the chemical potential is

$$\bar{\chi}_{int} = \Omega n_z \frac{\partial g(z_f)}{\partial z_f} = \frac{-\Omega g_0 l}{\sqrt{\left(\frac{dz_f}{dx}\right)^2 + \left(\frac{dz_f}{dy}\right)^2 + 1}\left(z_f - z_s + l\right)^2} \tag{3.72}$$

Where Ω is the atomic volume, g_0 is the atomic density of the interface, and l is the relevant length scale factor. Equation (3.72) can be expressed in terms of the normalized surface profiles as

$$\bar{\chi}_{int} = \frac{-\Omega g_0 \bar{l}}{\sqrt{\left(\frac{\lambda_y}{\lambda_x}\frac{d\bar{z}_f}{d\bar{x}}\right)^2 + \frac{\lambda_x}{\lambda_y}\left(\frac{d\bar{z}_f}{d\bar{y}}\right)^2 + 1}\left(\bar{z}_f - \bar{z}_s + \bar{l}\right)^2 \sqrt{\lambda_x \lambda_y}} \tag{3.73}$$

where

$$\bar{l} = \frac{l}{\sqrt{\lambda_x \lambda_y}}. \tag{3.74}$$

The contribution of the interface to the chemical potential can then be incorporated into the evolution process, noting that due to the inverse dependence on the film thickness, the term will only be significantly expressed for instances where the film has become very thin.

4 Kinetic Island Evolution

The first step in this investigation is to begin to form an understanding of kinetic island evolution, beginning with flat substrate systems. Cases of both high and lower areal density are considered, and the resulting island shapes are analyzed in the context of established and expected phenomena to provide a starting point for further energetic analysis. The high areal density case represents systems of islands which are closely spaced on the substrate surface, while the lower areal density case represents more sparsely spaced islands. In the course of executing these simulations it was determined that kinetic simulations with a higher degree of refinement would not be computationally feasible, and what was originally planned as a kinetic evolution analysis of islands on patterned substrates was modified to an energetic analysis in recognition of this limitation.

For the simulations of high areal density kinetic island evolution on a flat substrate, a film with a nominal normalized thickness of 0.10 is applied to a unit periodic cell (i.e. normalized dimensions of 1.0x1.0) with an initial sinusoidal perturbation. It was found that initially flat films resisted evolution, even in cases where island evolution would be expected, because the mathematical flatness of the film resulted in a null chemical potential gradient across the surface. Relying on computational tolerances in the numerical values to start the evolution of the film was not effective, as the numerical accuracy was too high to create a large enough potential difference for the process to begin. Figure (8) shows a typical initially perturbed film evolving into an island, in this case for a normalized characteristic length of $\bar{L}^* = 0.35$. Figure (8a) shows the initially sinusoid perturbation of the film surface. In Figure (8b) the lower portions of the film are unfavorable due to higher elastic constraint from the substrate, and so this material migrates towards the more raised section resulting in an initial flattening of the overall profile. In Figure (8c) material begins to move inward, raising the center of the film and starting to form an island. Figure (8d) shows the continuation of island initialization, with additional material accumulating in the center of the structure. In Figure (8e) vertical island

growth slows as increased surface energy from the raised shape begins to balance the strain energy reduction associated with removing additional material from the elastic constraint of the substrate. The final stable island configuration is achieved when strain energy and surface free energy come into equilibrium, resulting in the cessation of the kinetic evolution, as shown in Figure (8f).

In the interest of expediency, for the case of the low areal density kinetic island evolution study, a previously established island shape from the high areal density kinetic evolution was scaled down and placed on the substrate with a more highly refined resolution, and then allowed to relax kinetically. This shortcut allowed the more sparse system to reach its equilibrium state more quickly, which was necessary because of the increased computational intensity brought about by the refined resolution. The refinement of the resolution for this part of the analysis was necessary to capture the desired details of island shape since the island was proportionally smaller compared to the unit cell on which it sits. After observing the required processing time for these simulations, it was determined that the further refinement in resolution of the kinetic simulation that would be required for more highly detailed investigations, such as the location of islands on a patterned substrate and the inclusion of multiple sparsely spaced islands, would not be feasible due to the computational requirements. The energetic comparison of systems with differing island configurations and arrangements will be substituted instead, allowing critical questions of morphological favorability to be answered while still constraining the analysis to a slightly reasonable timescale for execution.

4.1 High Areal Density Island Evolution

High areal density islands on a flat substrate are interesting in their own right, as such regular arrays of quantum dots have compelling uses in both electronic and optical applications. It was found that the simulation developed for this investigation effectively models the formation of such quantum dot arrays, and that varying system parameters can be used to control the shape of the islands in the arrays. Note

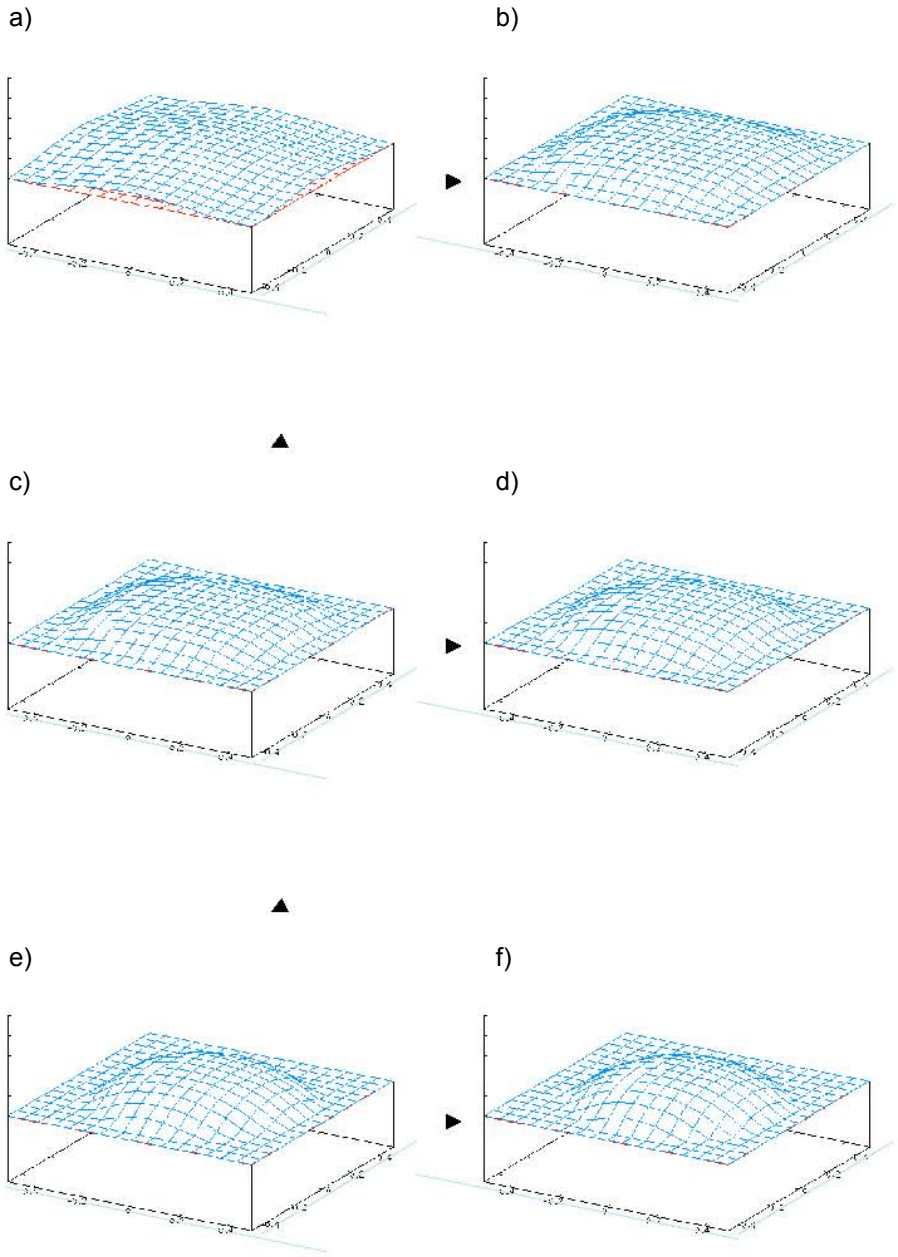

Figure 8: A typical initially perturbed film evolving into an island for normalized characteristic length $\bar{L}^* = 0.35$. a) Initial film surface b) Initial evolution of material away from highly constrained areas c) Island formation begins d) Island formation continues e) Island formation slows as surface and strain energy begin to balance f) The final stable island shape is reached when surface free energy and strain energy are in equilibrium.

that for all images show, the boundary conditions for each system cell are periodic, and hence the single island shown is repeated indefinitely along the plane of a infinite substrate/film system, making up the regular array of structures. Figure (9) shows the progression of island shapes with varying normalized characteristic length from $\bar{L}^* = 0.35$ to $\bar{L}^* = 0.50$. It is observed that as the normalized characteristic length increases the island becomes flatter. This is expected, as the increase in surface energy density/reduction in mismatch strain would result in a more pronounced energetic benefit for a reduction in free surface area, whereas higher mismatch strain and lower surface energy density would be expected to favor the removal of material from the constraint of the substrate in the form of higher islands, as is observed.

The trend of increasing normalized free energy with increasing normalized characteristic length is shown in Figure (10). It is important to note that, in order to eliminate troublesome roundoff errors, the normalized characteristic lengths reported do not include the energy of the flat film (the constant portion of the Fourier expansion representation of the solution). This was done to eliminate the possibility of the small incremental changes in energy between iterations being lost in the round off of the much larger constant term. This explains why the values reported are negative; the island configurations of the film have lower free energy than the flat film, which makes eminent good sense as they could not otherwise be energetically admissible as viable morphological configurations.

Figure (11) shows the trend of normalized free energy versus island aspect ratio. The aspect ratio of an island describes the relationship between the width at its base and its maximum height. While this metric does not describe the overall shape of the islands, it does provide an overview of the general island shape.

For a more direct understanding of how system parameters effect island shape, Figure (12) plots aspect ratio versus normalized characteristic length. Recalling Equation (3.54), it is clear that an increase in the normalized characteristic length can be interpreted as either an increase in surface energy density or a decrease in lattice mismatch strain, while a decrease in normalized characteristic length can correspond to a decrease in surface energy density or an increase in lattice mis-

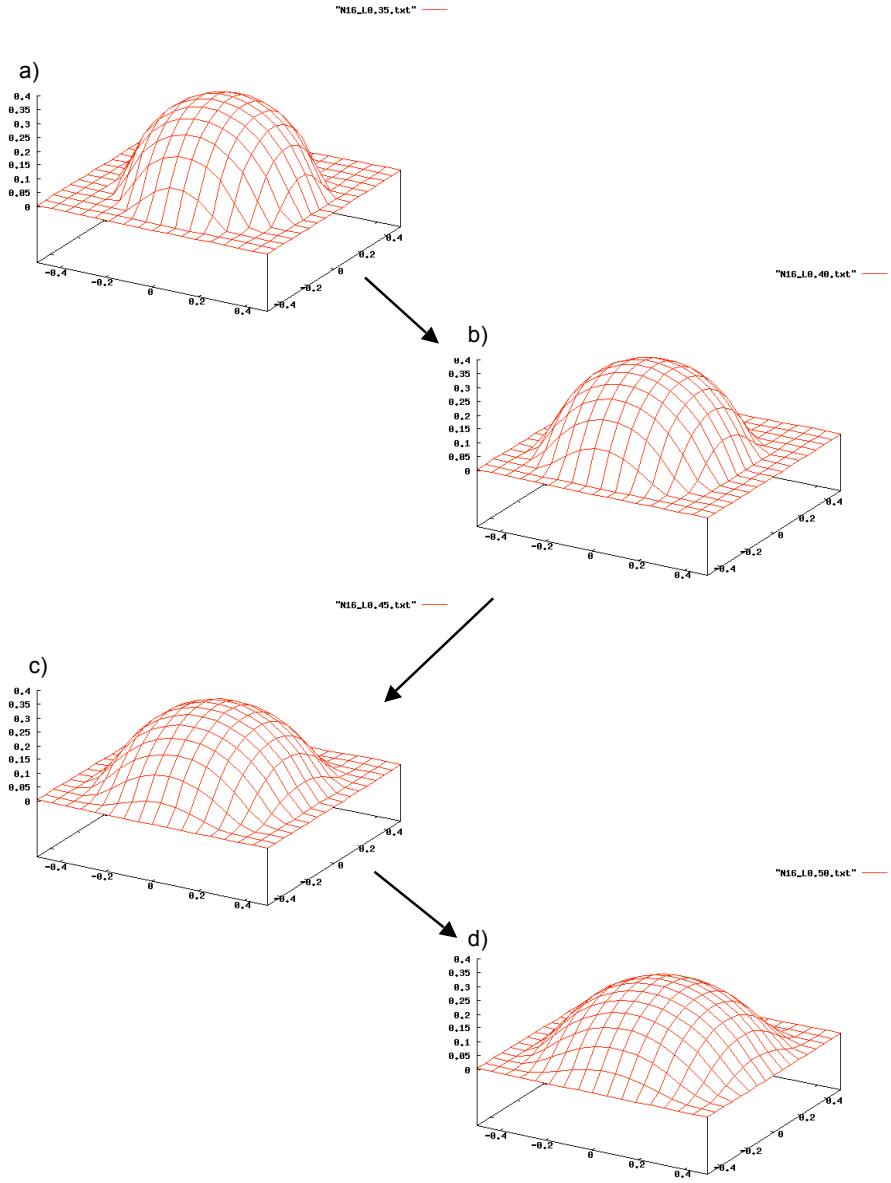

Figure 9: High areal density island shapes. The progression shows the change in island shapes with increasing normalized characteristic length, which corresponds to increasing surface energy density, or decreasing mismatch strain. It is noted that as the normalized characteristic length increases from a) $\bar{L}^* = 0.35$, to b) $\bar{L}^* = 0.40$, to c) $\bar{L}^* = 0.45$, and then to d) $\bar{L}^* = 0.50$, the island becomes flatter. This is as expected, as the increase in surface energy density/reduction in mismatch strain would result in a more pronounced energetic benefit for a reduction in free surface area, whereas higher mismatch strain and lower surface energy density would be expected to favor the removal of material from the constraint of the substrate in the form of higher islands, as observed.

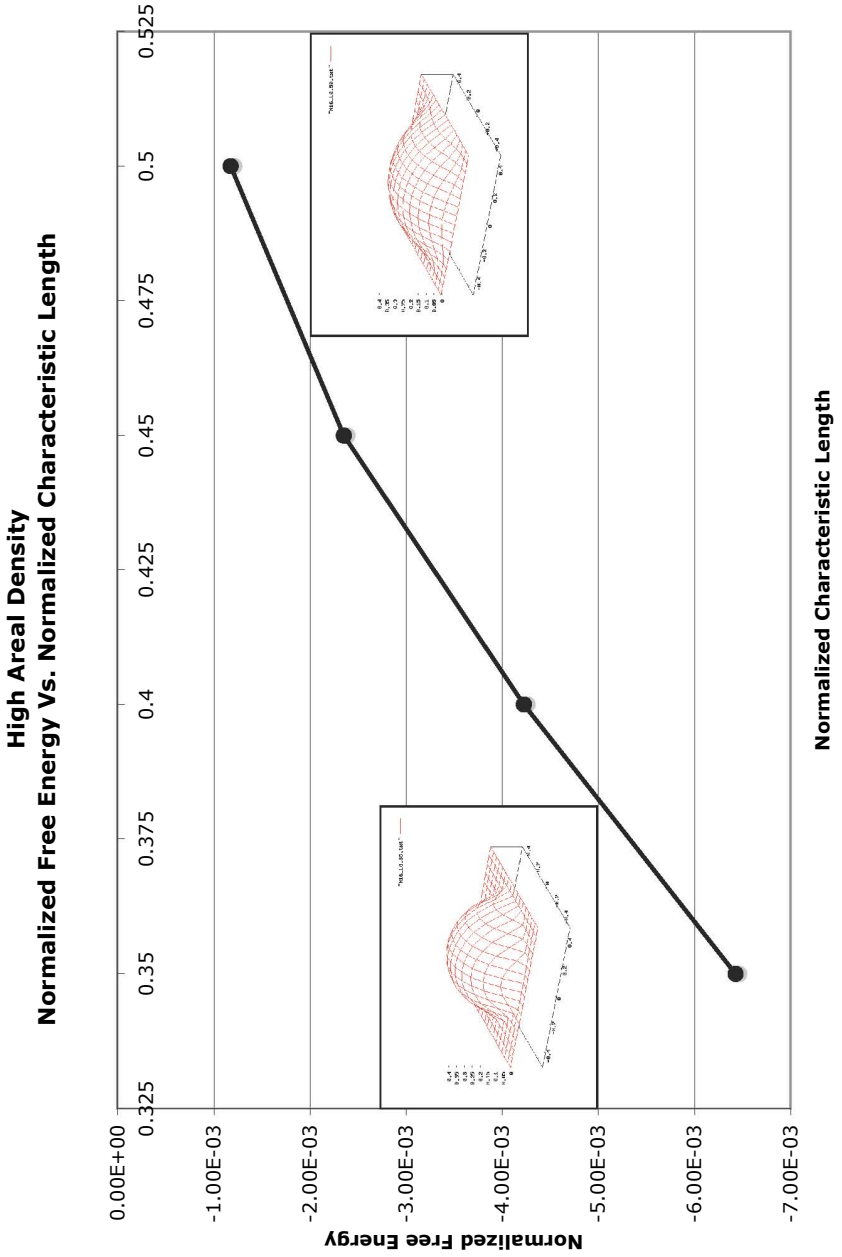

Figure 10: High areal density island normalized free Energy $\bar{U}$ versus normalized characteristic length $\bar{L^*}$.

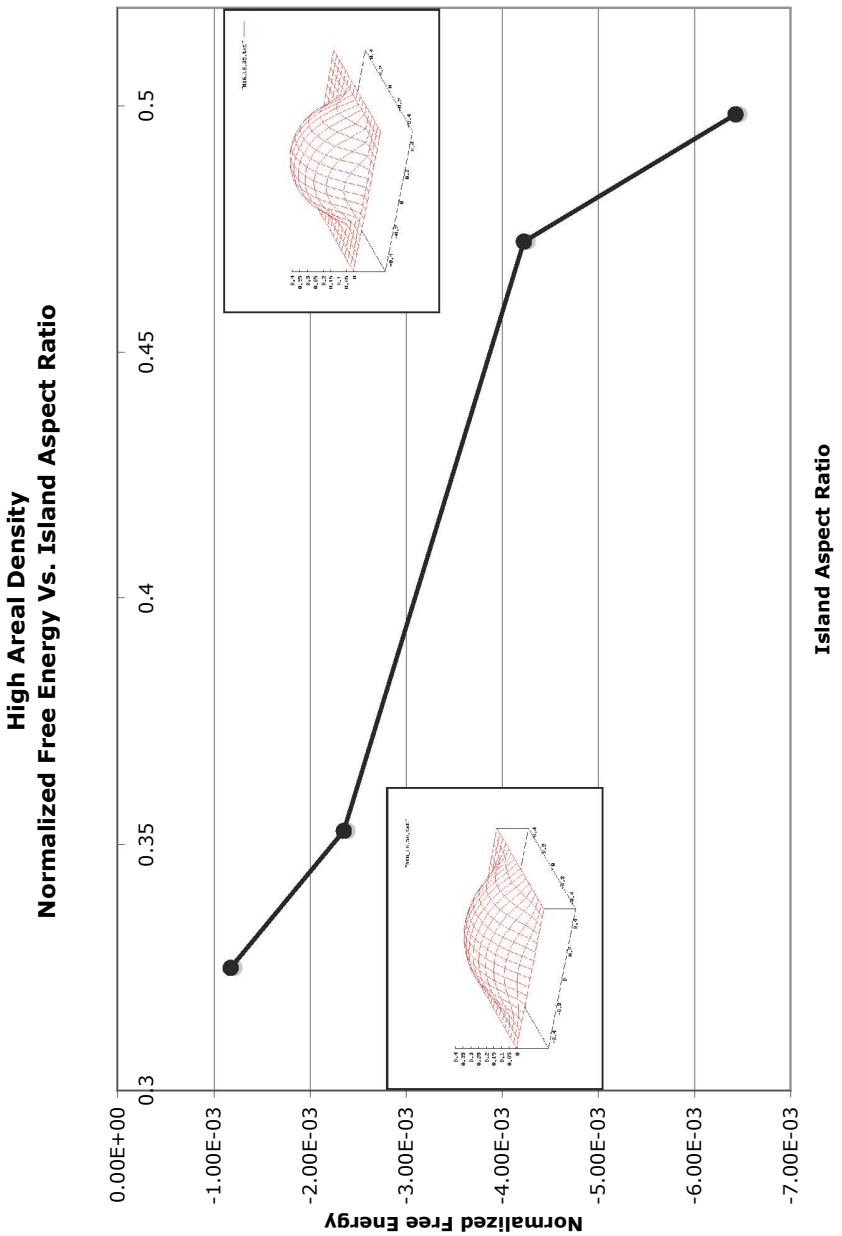

Figure 11: High areal density island normalized free Energy $\bar{U}$ versus aspect ratio α.

match strain. This means that higher normalized characteristic lengths are expected to result in a greater significance of surface energy over strain energy, while lower characteristic lengths are expected to result in a greater significance of strain energy over surface energy. Figure (12) shows that this is indeed the case. As the normalized characteristic length increases, the island's aspect ratio decreases, or the island becomes flatter, which is consistent with a system where surface energy plays a more prevalent role since the flatter island has a lower surface area than a higher aspect ratio island. If the normalized characteristic length is decreased, the aspect ratio of the island increases, which is consistent with a system where strain energy is more prevalent, since the more raised island morphology allows more material to escape the elastic constraint of the substrate.

Of additional interest is the relationship between the minimum film thickness and the normalized characteristic length, shown in Figure (13). This is tied back to the tendency of higher strain energy to favor taller islands while higher surface energy density favors flatter islands. As islands become flatter, there is a greater amount of material that is distributed over the substrate surface rather than accumulating in the localized mass of the island, which results in greater minimum film thicknesses for high normalized characteristic lengths. As the normalized characteristic length continues to increase, representing further dominance of surface free energy over strain energy, the general trend is that the minimum film thickness will increase as more and more material remains distributed over the film. Figure (14) shows the ratio of minimum to maximum film thickness versus normalized characteristic length which clearly illustrates the monotonic tendency of minimum film thickness to increase relative to maximum film thickness with increasing $\bar{L}^*$. Together these figures support the understood phenomena of surface energy dominated systems favoring flatter island shapes, and also show that, to a degree, this tendency towards flatter films results in not just a change to flatter island shapes, but also the deallocation of material from the island configuration back towards that of the uniformly distributed film.

When $\bar{L}^*$ was increased further, the island shape collapsed and the initial

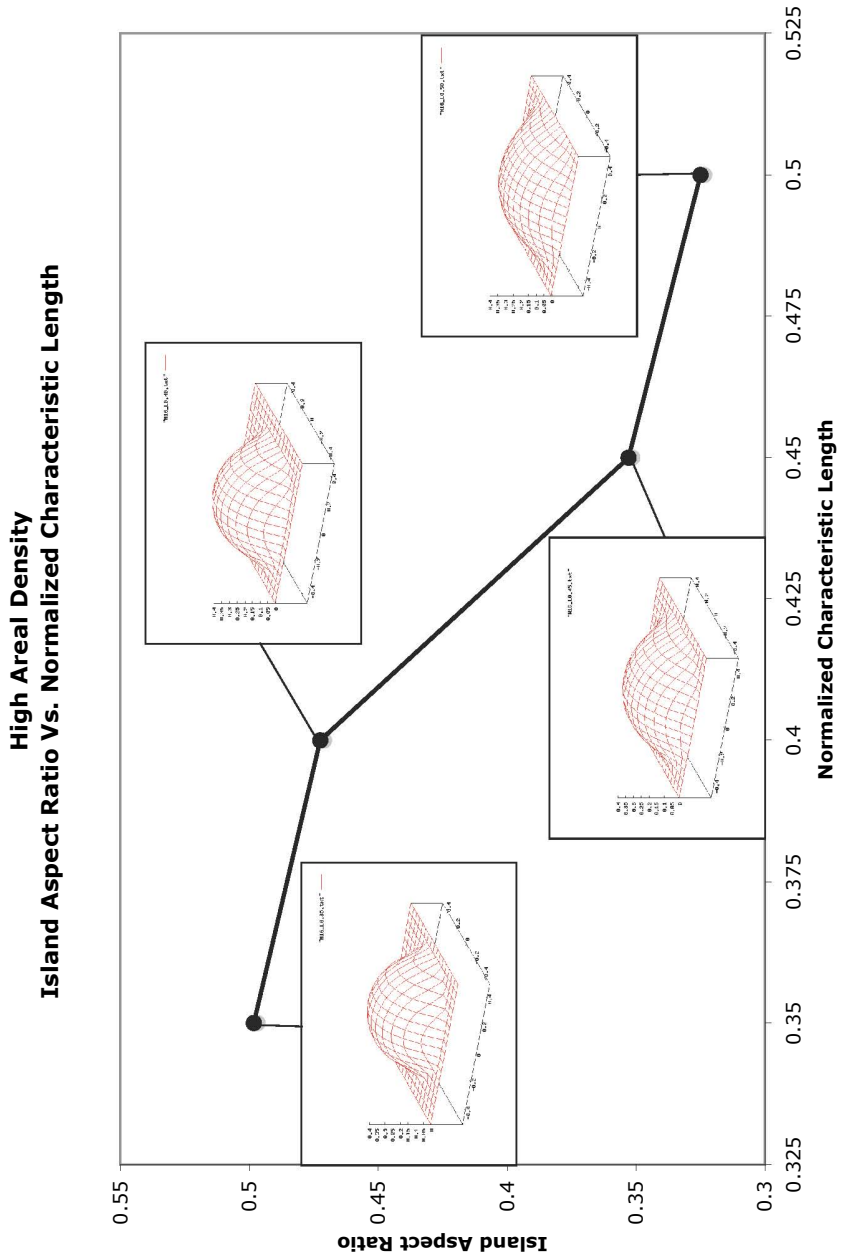

Figure 12: High areal density island aspect ratio α versus normalized characteristic length $\bar{L}^*$.

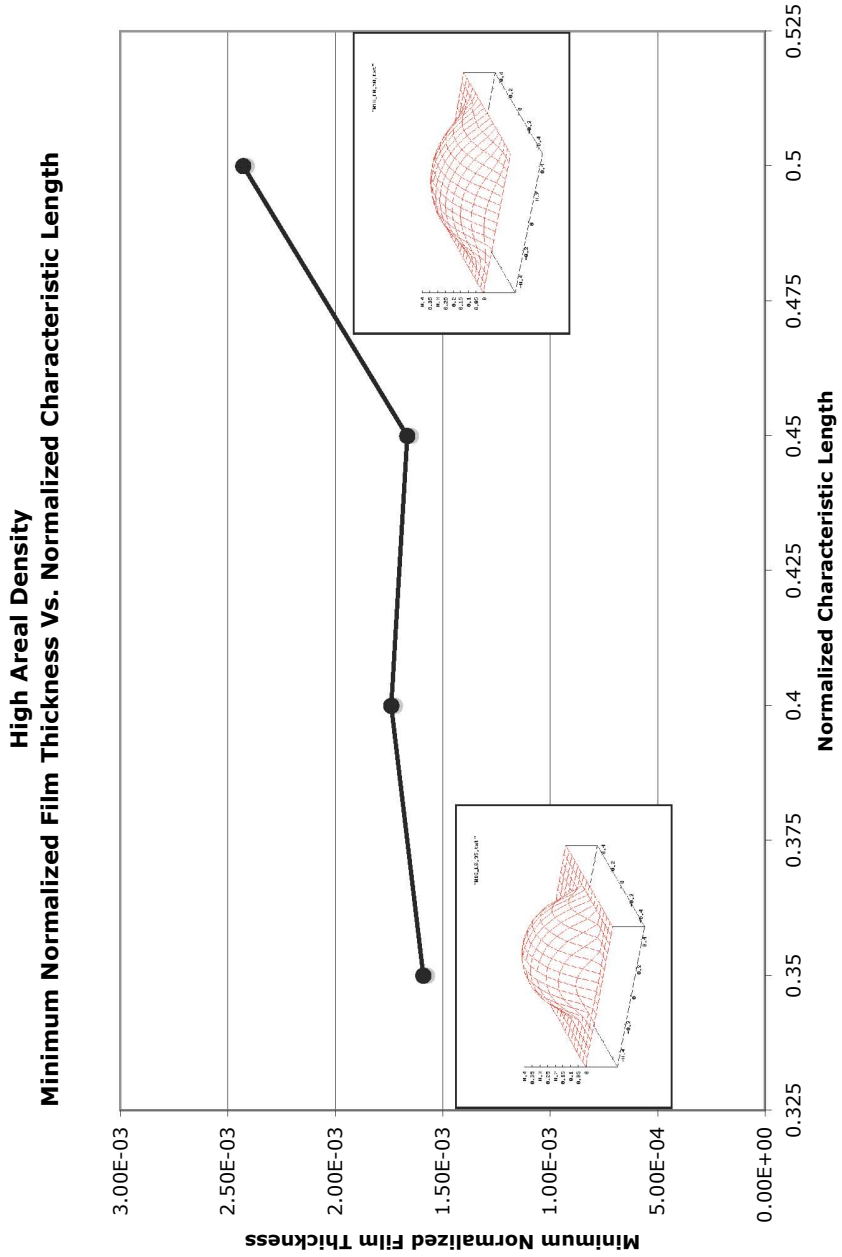

Figure 13: High areal density minimum film thickness versus normalized characteristic length $\bar{L}^*$.

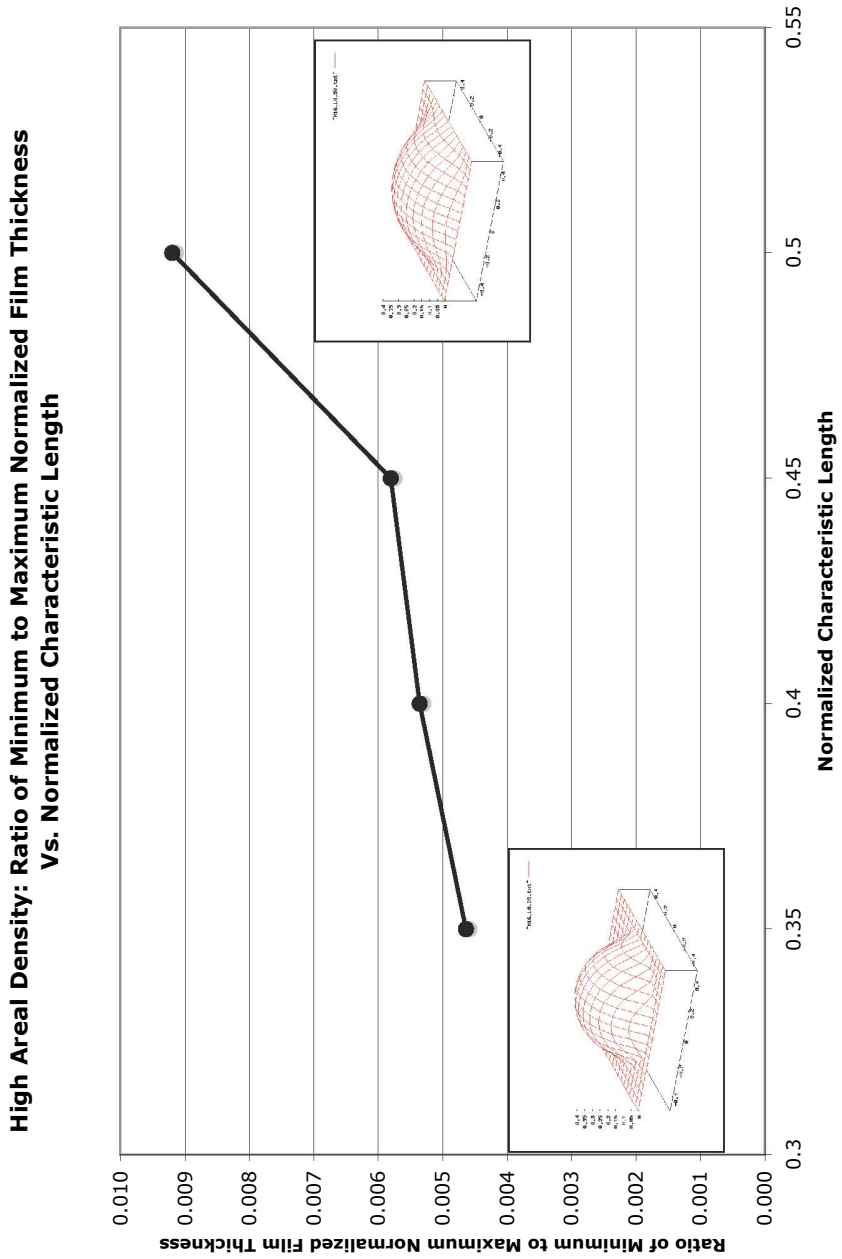

Figure 14: High areal density ratio of minimum to maximum film thickness versus normalized characteristic length $\bar{L}^*$.

perturbation to the film evolved into a perfectly flat and uniformly distributed film. This occurred because the critical value of the normalized characteristic length had been exceeded, resulting in a characteristic wavelength for the system that exceeded the unit size of the periodic cell, thereby suppressing island growth. The characteristic wavelength is the wavelength at which a particular system will grow preferentially [43].

4.2 Low Areal Density Island Evolution

While high areal density epitaxial island formations offer significant promise as electronic and optical quantum dot arrays, the formation of low areal density island configurations is also of interest for the understanding of discrete island characteristics which can be gained. Closely spaced islands have a self energy associated with the geometry and system properties of the island, and an island-island interaction energy with each and every one of its neighboring islands (out through the infinite space of periodically repeating islands in the case of the particular model used here). Without some form of reference to the island self energy, it can be difficult to discern between those two energies, and it is thus desirable to find the energy of a single island alone on the infinite substrate, or in a more numerically reasonable sense, far enough away from any other islands such that the island-island interaction will be negligible.

In order to consider this analysis, it is necessary to increase the periodic cell size of the system so that the repeated patterns will be sufficiently spaced so as to rule out island-island interaction energy. Ideally, a convergence analysis should be conducted to determine the distance at which only the island self energy remains. Due to computational constraints, this will not be possible. However, the periodic cell size can be doubled (four times the area) with only slightly unreasonable computational requirements. Further increase of the cell size will not be possible due to excessive time that such simulations would require. It will therefore be necessary to look at these lower areal density island evolutions as approximations

for the isolated island case, bearing in mind that this assumption will only be able to indicate trends rather than specific values. It is important to note that the nature of the Fourier series representation of the film and substrate surfaces requires that the cell size scale with powers of two, which is a requirement of the Fast Fourier Transform used to go between spectral and spacial coordinates.

As discussed previously, to maximize the efficiency of this more computationally demanding simulation, an island shape from the high areal density analysis was scaled appropriately and placed onto the larger periodic cell, and then allowed to relax kinetically such that it sought out its equilibrium morphology. By starting off with a raised island shape for the film, the initial stages of the simulation where the film has only a slight perturbation is omitted, thereby avoiding a portion of the calculation which would evolve very slowly due to very low chemical potential gradients.

Figure (15) shows the progression of island shapes with varying normalized characteristic length from $\bar{L}^* = 0.14$ to $\bar{L}^* = 0.20125$. It is observed that as the normalized characteristic length increases the island becomes flatter. This is expected, as with the high areal density case, as the increase in surface energy density/reduction in mismatch strain would result in a more pronounced energetic benefit for a reduction in free surface area, whereas higher mismatch strain and lower surface energy density would be expected to favor the removal of material from the constraint of the substrate in the form of higher islands, as is observed. The general trends seen for the high areal density case and shown in Figure (10) through Figure (14) are also seen for the low areal density analysis. The trend of increasing normalized free energy with increasing normalized characteristic length is shown in Figure (16). Figure (17) shows the trend of normalized free energy versus island aspect ratio. Figure (18) plots aspect ratio versus normalized characteristic length. Figure (19) show the relationship between the minimum film thickness and the normalized characteristic length. Figure (20) shows the ratio of minimum to maximum film thickness versus normalized characteristic length.

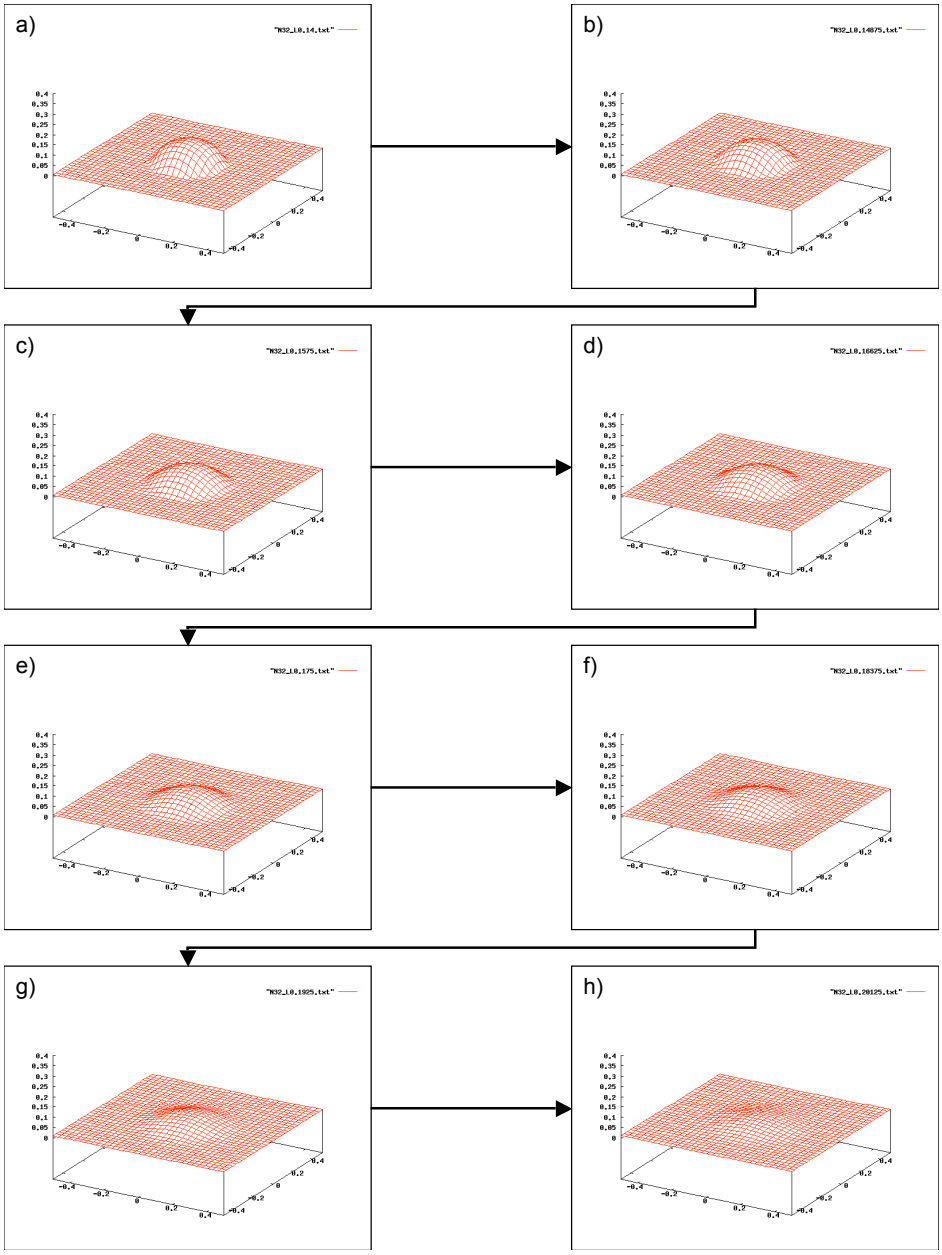

Figure 15: Low areal density island shapes. The progression shows the change in island shapes with increasing normalized characteristic length, which corresponds to increasing surface energy density, or decreasing mismatch strain. It is noted that as the normalized characteristic length increases from a) $\bar{L}^* = 0.14$, to b) $\bar{L}^* = 0.14875$, to c) $\bar{L}^* = 0.1575$, d) $\bar{L}^* = 0.16625$, to e) $\bar{L}^* = 0.175$, to f) $\bar{L}^* = 0.18375$, g) $\bar{L}^* = 0.1925$,and then to h) $\bar{L}^* = 0.20125$, the island becomes flatter. This is as expected, as the increase in surface energy density/reduction in mismatch strain would result in a more pronounced energetic benefit for a reduction in free surface area, whereas higher mismatch strain and lower surface energy density would be expected to favor the removal of material from the constraint of the substrate in the form of higher islands, as observed.

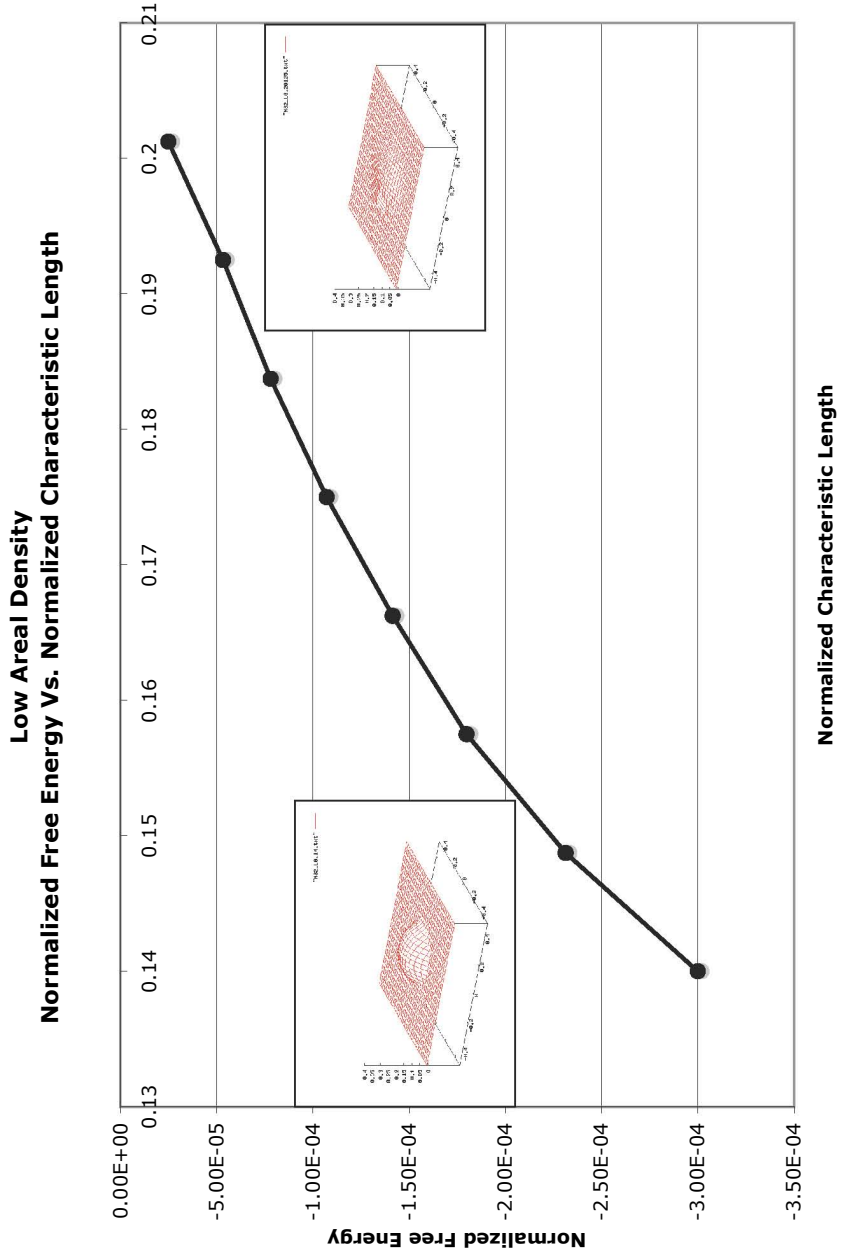

Figure 16: Low areal density island normalized free Energy $\bar{U}$ versus normalized characteristic length $\bar{L^*}$.

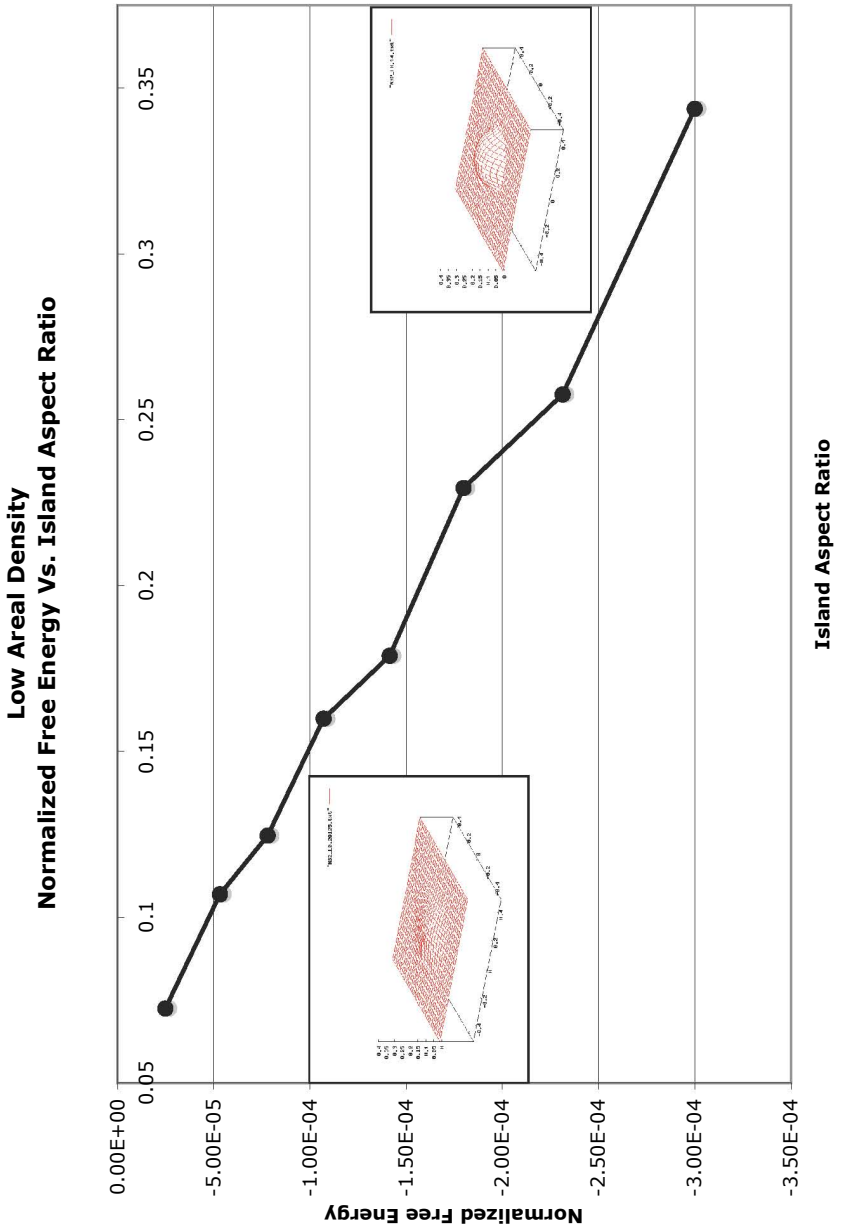

Figure 17: Low areal density island normalized free Energy $\bar{U}$ versus aspect ratio α.

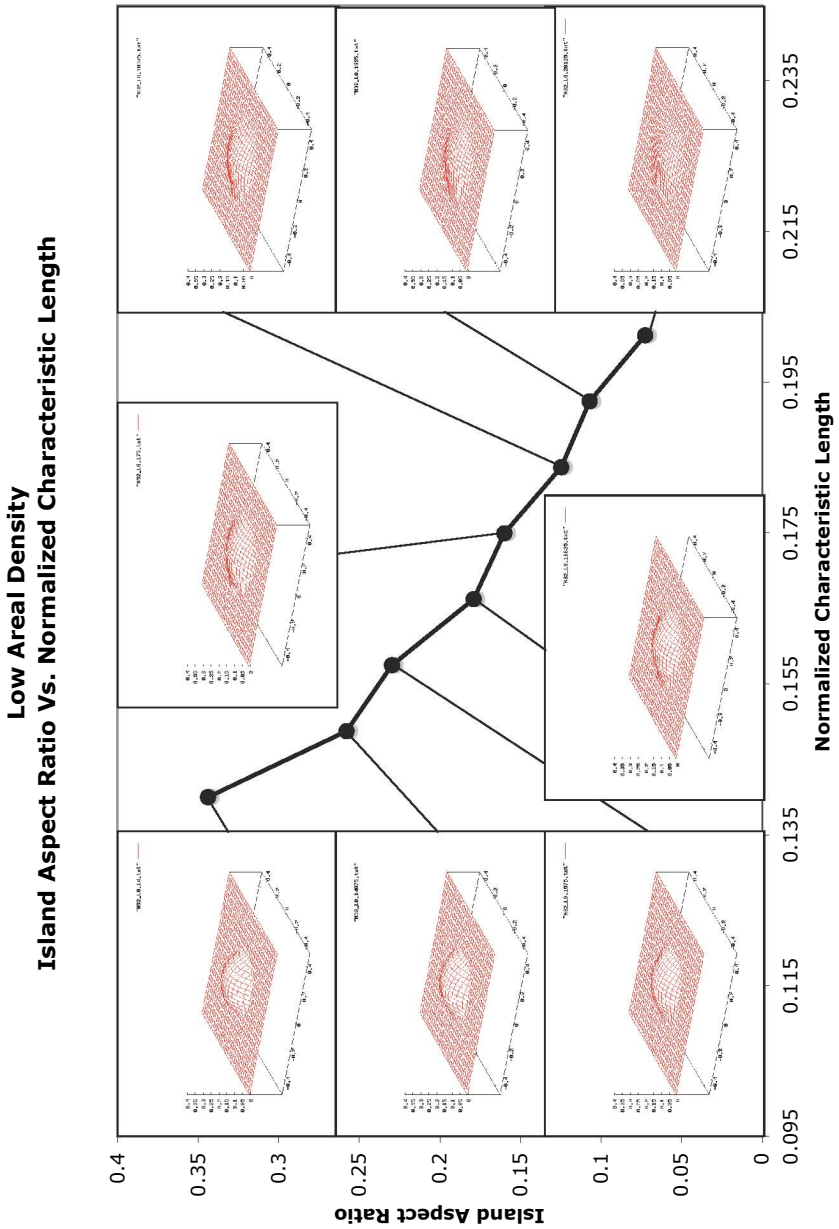

Figure 18: Low areal density island aspect ratio α versus normalized characteristic length $\bar{L}^*$.

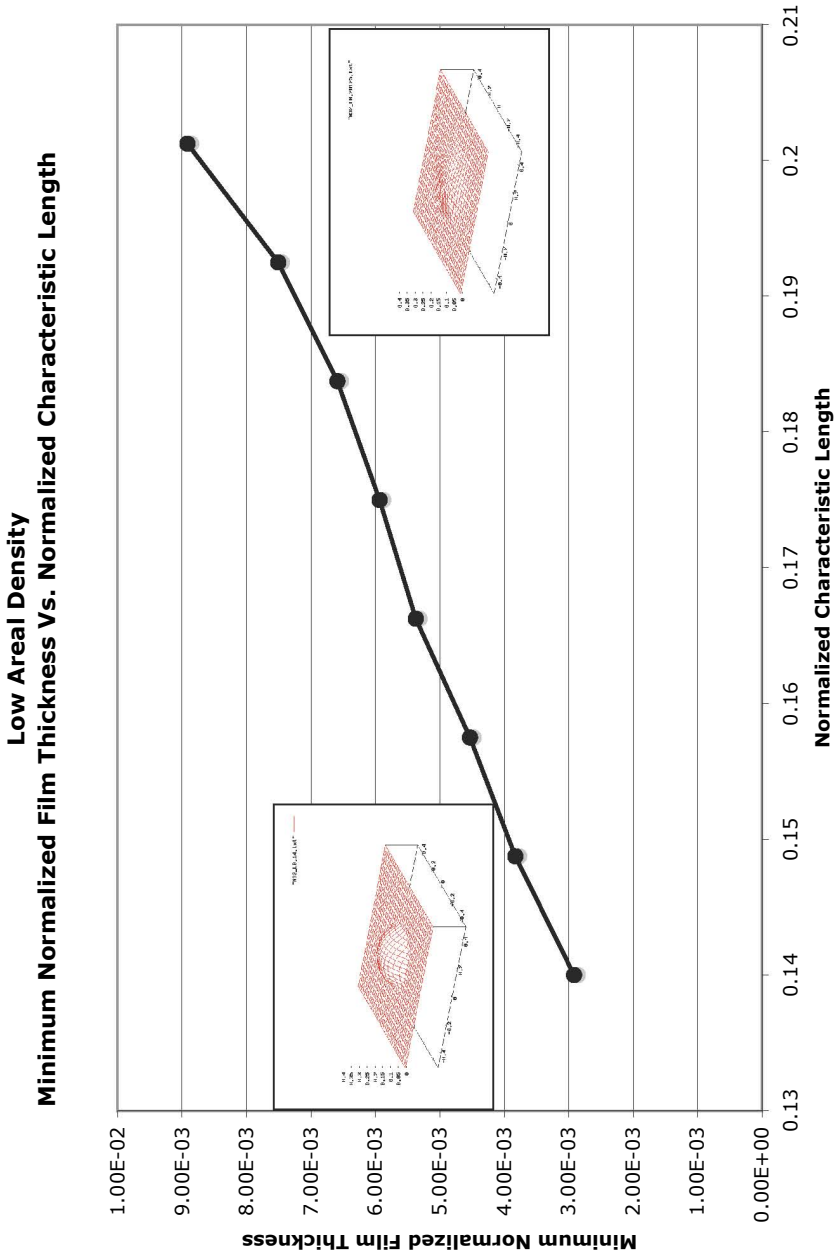

Figure 19: Low areal density minimum film thickness versus normalized characteristic length $\bar{L}^*$.

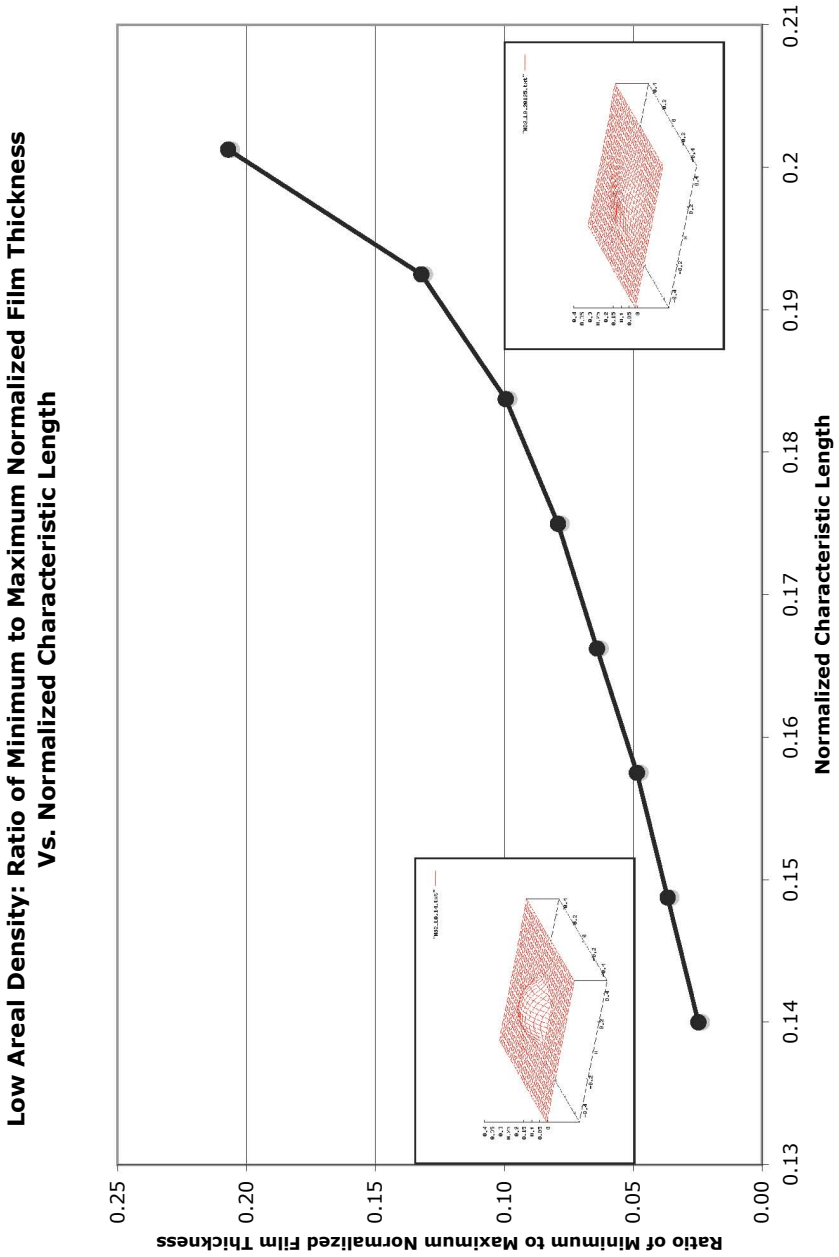

Figure 20: Low areal density ratio of minimum to maximum film thickness versus normalized characteristic length $\bar{L}^*$.

5 Conclusions

Having established the functionality and limitations of the kinetic model developed for this investigation, it was clear that a large scale kinetic simulation of island evolution on a patterned substrate system would not be computationally feasible. To gain insight into the behavior of islands on a patterned substrate, an energetic analysis was conducted in which the free energies of different configurations of islands (that is to say, systems with similar deposit volumes distributed in different arrangements and numbers of islands) were compared to determine the relative favorability between considered cases. The influence of the wetting layer thickness was also considered. While this was a more limited approach compared to a full kinetic evolution simulation, it was computationally reasonable, and still provided valuable understanding regarding the formation of epitaxial nanostructures grown on areally constrained substrate surfaces.

A model based on simple energetic arguments suggests a rather rich behavior of Stranski-Krastanov systems constrained to grow on a finite area of a substrate. Accounting only for strain energy, isotropic surface energy, and a wetting layer potential energy, it is found that the effect of an areal constraint on film growth can cause a configuration with multiple islands to be energetically favored over that of a single large island. Comparisons are made to experimental observations of multiple island formations under fixed-area epitaxial growth condition, and while it has been hypothesized that the nature of these multiple island configurations can be attributed to elastic interaction between the islands and the relative compliance of different locations within the substrate system, the current investigation suggests that the effects of the areal constraint (such as that represented by a raised substrate topology) alone can explain the stability of multiple island configurations.

Several extensions to this work are warranted. Firstly the analysis of the global minima considered a maximum of nine islands. A larger number of islands could be considered in order to form a more complete equilibrium phase diagram. Nevertheless, the diagram of Figure (3) does indicate configurations that resist coars-

ening. Additionally, the effect of island-island elastic interaction energy was considered only for a limited case and omitted from the large scale analysis and including this effect will modify the structure of the phase diagram. This will be fully addressed in future work by utilizing results found using the arbitrary island morphology model. Finally, kinetics is expected to play an important role in determining the configuration resulting from deposition, as metastable configurations are likely to arise. To evaluate the stability of these configurations the activation barrier for transformation to a lower energy state must be calculated.

Based on the kinetic simulation of island evolution for both high and lower areal density systems, it is concluded that the model and its application in the simulation software developed produces results which are consistent with previously observed and understood phenomena. System parameters trending towards lower elastic mismatch between the film and substrate or greater surface energy density result in islands with lower aspect ratios, with an ultimate tendency towards a flat film as the trend continues. System parameters trending towards greater mismatch between the film and substrate or lower surface energy density result in islands with higher aspect ratios. These results are both as expected, as higher elastic mismatch would favor the removal of material from the elastic constraint of the substrate, while greater surface energy density would favor the elimination of free surface area, with a flat film offering the lowest possible surface area.

Plans for future work include the application of the kinetic model to produce more physically representative quasi-analytic energy expressions which can then be reincorporated into the areal constraint model. Reevaluation using these expressions is expected to provide further insight into the specific nature of the effect of island shape and morphology on system arrangements and configurations. This should also include the determination of a reasonable expression for the island-island strain field interaction energy which is currently absent from the areal constraint model. As discussed, it is expected that this island-island interaction energy term will play an important and interesting role in determining the relative favorability of multiple island configurations. These topics are left for future investigations.

References

[1] D. S. L. Mui, D. Leonard, L. A. Coldren, and P. M. Petroff. Surface migration induced self-aligned inas islands grown by molecular beam epitaxy. *Applied Physics Letters.*, 66(13):1620, 1995.

[2] T. Kitajima, B. Liu, and S. R. Leone. Two-dimensional periodic alignment of self-assembled ge islands on patterned si(001) surfaces. *Applied Physics Letters*, 80(3):497, 2002.

[3] G. Jin, J. L. Liu, S. G. Thomas, Y. H. Luo, K. L. Wang, and B. Y. Nguyen. Controlled arrangement of self-organized ge islands on patterned si (001) substrates. *Applied Physics Letters*, 75(18):2752, 1999.

[4] Z. Zhong, A. Halilovic, M. Muhlberger, F. Schaffler, and G. Bauer. Positioning of self-assembled ge islands on stripe-patterned si(001) substrates. *Journal of Applied Physics*, 93:6258, 2003.

[5] F. Liu, A.H. Li, and M.G. Lagally. Self-assembly of two-dimensional islands via strain-mediated coarsening. *Physical Review Letters*, 87(12):126103–1, 2001.

[6] J. J. Eggleston and P. W. Voorhees. Ordered growth of nanocrystals via a morphological instability. *Applied Physics Letters.*, 80(2):306, 2002.

[7] C. h. Chui, Z. Huang, and C.T. Poh. Formation of nanostructures by the activated stranski-krastanow transition method. *Physical Review Letters*, 93(13):136105–1, 2004.

[8] R. V. Kukta and L. B. Freund. Minimum energy configuration of epitaxial material clusters on a lattice-mismatched substrate. *Journal of the Mechanics of Physical Solids*, 45:1835, 1997.

[9] H. T. Johnson and L. B. Freund. Mechanics of coherent and dislocated island morphologies in strained epitaxial material systems. *Journal of Applied Physics*, 81:6081, 1997.

[10] S. C. Lee, A. Stintz, and S. R. J. Brueck. Nanoscale limited area growth of inas islands on gaas(001) by molecular beam epitaxy. *J. Appl. Phys.*, 91:3282–3288, 2002.

[11] L. Vescan, T. Stoica, B. Hollander, A. Nassiopoulou, A. Olzierski, I. Raptis, and E. Sutter. Self-assembling of ge on finite si(001) areas comparable with the island size. *Appl. Phys. Lett.*, 82:3517–3519, 2003.

[12] Tae-Sik Yoon, Zuoming Zhao, Jian Liu, Ya-Hong Xie, Du yeol Ryu, Thomas P. Russell, Hyun-Mi Kim, and Ki-Bum Kim. Selective growth of ge islands on nanometer-scale patterned sio_2/si substrate by molecular beam epitaxy. *Appl. Phys. Lett.*, 89:063107–1–063107–3, 2006.

[13] C. V. Cojocaru, A. Bernardi, J. S. Reparaz, M. I. Alonso, J. M. MacLeod, C. Harnagea, and F. Rosei. Site-controlled growth of ge nanostructures on si (100) via pulsed laser deposition nanostenciling. *Appl. Phys. Lett.*, 91:113112–1–113112–3, 2007.

[14] C. Dais, H. H. Solak, E. Mller, and D. Grtzmacher. Impact of template variations on shape and arrangement of si/ge quantum dot arrays. *Appl. Phys. Lett.*, 92:143102–1–143102–3, 2008.

[15] Q. H. Xie, A. Madhukar, P. Chen, and N. P. Kobayashi. Vertically self-organized inas quantum box islands on gaas(100). *Physical Review Letters*, 75:2542, 1995.

[16] C. S. Ozkan, W. D. Nix, and H. Gao. Strain relaxation and defect formation in heteroepitaxial si1 xgex films via surface roughening induced by controlled annealing experiments. *Applied Physics Letters*, 70(17):2247, 1997.

[17] Y. S. Tang, S. Cai, G. Jin, J. Duan, , K. L. Wang, H. M. Soyez, and B. S. Dunn. Sige quantum dots prepared on an ordered mesoporous silica coated si substrate. *Applied Physics Letters*, 71(17):2448, 1997.

[18] J. A. Floro, E. Chason, M. B. Sinclair, L. B. Freund, and G. A. Lucadamo. Dynamic self-organization of strained islands during sige epitaxial growth. *Applied Physics Letters*, 73(7):951, 1998.

[19] H-J. Gao, D. Kumar, K. G. Cho, P. H. Holloway, R. K. Singh, X. D. Fan, Y. Yan, and S. J. Pennycook. Epitaxial growth of y2o3 :eu thin films on laalo3. *Applied Physics Letters*, 75(15):2223, 1999.

[20] Y.H. Luo, J.L. Liu, G. Jin, J. Wan, K.L. Wang, C.D. Moore, M.S. Goorsky, C. Chih, and K.N. Tu. Effective compliant substrate for low-dislocation relaxed sige growth. *Applied Physics Letters*, 78:1219, 2001.

[21] Y.H. Luo, J. Wan, R.L. Forrest, J.L. Liu, G. Jin, M.S. Goorsky, and K.L. Wang. Compliant effect of low-temperature si buffer for sige growth. *Applied Physics Letters*, 78:454, 2001.

[22] Y.H. Luo, J.L. Liu, G. Jin, J. Wan, and K.L. Wang. An effective compliant substrate for low-dislocation relaxed $si_{1-x}ge_x$ growth. *Applied Physics A*, 74:699, 2002.

[23] X.Z. Liao, J. Zou, D.J.H. Cockayne, J. Wan, Z.M. Jiang, G. Jin, and K.L. Wang. Annealing effects on the microstructure of ge/si(001) quantum dots. *Applied Physics Letters*, 79(9):1258, 2001.

[24] R. Leon, S. Chaparro, S. R. Johnson, C. Navarro, X. Jin, Y. H. Zhang, J. Siegert, S. Marcinkevicius, X. Z. Liao, and J. Zou. Dislocation-induced spatial ordering of inas quantum dots: Effects on optical properties. *Journal of Applied Physics*, 91:5826, 2002.

[25] C. Teichert. Self-organized semiconductor surfaces as templates for nanostructured magnetic thin films. *Applied Physics A*, 76:653, 2003.

[26] E.J. Tan, M.L. Kon, K.L. Pey, P.S. Lee, Y.W. Zhang, W.D. Wang, and D.Z. Chi. Effects of si(001) surface amorphization on ersi2 thin film. *Thin Solid Films*, 504:157, 2006.

[27] K.L. Wang. Self-assembled ge quantum dots on si and their applications. *Journal of Crystal Growth*, 237-239:1892, 2002.

[28] G. Jin, J.L. Liu, S.G. Thomas, Y.H. Luo, K.L. Wang, and B.-Y. Nguyen. Perfect alignment of self-organized ge islands on pre-grown si stripe mesas. *Applied Physics A*, 70:551, 2000.

[29] G. Jin, J.L. Liu, Y.H. Luo, and K.L. Wang. Control of the arrangment of self-organized ge dots on patterned si(001) substrates. *Thin Solid Films*, 369:49, 2000.

[30] G. Jin, J. Wan, Y.H. Luo, J.L. Liu, and K.L. Wang. Uniform and ordered self-assembled ge dots on patterned si substrates with selectively epitaxial growth technique. *Journal of Crystal Growth*, 227:1100, 2001.

[31] G. Jin, J.L. Liu, and K.L. Wang. Regimented placement of self-assembled ge dots on selectively grown si mesas. *Applied Physics Letters*, 76(24):3591, 2000.

[32] G. Jin, J.L. Liu, Y.H. Luo, and K.L. Wang. Cooperative arrangement of self-assembled ge dots on pre-grown si mesas. *Thin Solid Films*, 380:169, 2000.

[33] H.-M. Lee, T.-H. Yang, G. Luo, and E. Y. Chang. Flower-like distributed self-organized ge dots on patterned si(001) substrates. *Japanese Journal of Applied Physics*, 42:L718, 2003.

[34] Z. Zhong, A. Halilovic, M. Muhlberger, F. Schaffler, and G. Bauer. Ge island formation on stripe-patterned si(001) substrates. *Applied Physics Letters.*, 82:445, 2003.

[35] J. Tersoff. Stress-induced layer-by-layer growth of ge on si(100). *Physical Review B*, 43(11):9377, 1991.

[36] J. Tersoff. Stress-induced roughening in epitaxial growth. *Applied Surface Science*, 102:1, 1996.

[37] J. Tersoff. Continuum theory for strained epitaxial islands. *Physical Review Letters*, 79(24):4934, 1997.

[38] J. Tersoff. Self-organized epitaxial growth of low-dimensional structures. *Physica E*, 3:89, 1998.

[39] J. Tersoff. Kinetic effects in heteroepitaxial growth. *Applied Surface Science*, 188:1, 2002.

[40] F. Jonsdottir and L.B. Freund. Equilibrium surface roughness of a strained epitaxial film due to surface diffusion induced by interface misfit dislocations. *Mechanics of Materials*, 20:337, 1995.

[41] V.A. Shchukin, Ledentsov N, N, P.S. Kop'ev, and D. Bimberg. Spontaneous ordering of arrays of coherent strained islands. *Physical Review Letters*, 75(16):2968, 1995.

[42] J. A. Floro, M. B. Sinclair, E. Chason, L. B. Freund, R. D. Twesten, R. Q. Hwang, and G. A. Lucadamo. Novel sige island coarsening kinetics: Ostwald ripening and elastic interactions. *Physical Review Letters*, 84:701, 2000.

[43] R. V. Kukta and D. Kouris. On the mechanisms of epitaxial island alignment on patterned substrates. *Journal of Applied Physics*, 97:033527, 2005.

[44] Z. Suo and Z. Zhang. Epitaxial films stabilized by long ranged forces. *Physical Review B*, 58(8):5116, 1998.

[45] C. h. Chui. The self-assembly of uniform heteroepitaxial islands. *Applied Physics Letters.*, 75(22):3473, 1999.

[46] M. Ortiz, E.A. Repetto, and H. Si. A continuum model of kinetic roughening and coarsening in thin films. *Journal of the Mechanics and Physics of Solids*, 47:697, 1999.

[47] Y. W. Zhang. Formation of epitaxially strained islands by controlled annealing. *Applied Physics Letters.*, 75(2):205, 1999.

[48] Y.W. Zhang. Self-organization, shape transition, and stability of epitaxially strained islands. *Physical Review B*, 61(15):10388, 2000.

[49] Y. W. Zhang. Surface stability and evolution of biaxially strained epitaxial thin films. *Applied Physics letters*, 87:121916–1, 2005.

[50] F. Liu. Self-assembly of three-dimensional metal island: nonstrained versus strained islands. *Physical Review Letters*, 89(24):246105, 2002.

[51] P. Liu, Y. W. Zhang, and C. Lu. Self-organized growth of three-dimensional quantum-dot superlattices. *Applied Physics Letters*, 80(21):3910, 2002.

[52] P. Liu, Y. W. Zhang, and C. Lu. A three-dimensional concurrent atomisticcontinuum analysis of an epitaxially strained island. *Journal of Applied Physics*, 94(10):6350, 2003.

[53] P. Liu, Y. W. Zhang, and C. Lu. Formation of self-assembled heteroepitaxial islands in elastically anisotropic films. *Physical Review B.*, 67:165414–1, 2003.

[54] P. Liu, Y. W. Zhang, and C. Lu. Coarsening kinetics of heteroepitaxial islands in nucleationless stranski-krastanov growth. *Physical Review B.*, 68:035402–1, 2003.

[55] P. Liu, Y. W. Zhang, and C. Lu. Computer simulations of the stranskikrastanov growth of heteroepitaxial films with elastic anisotropy. *Surface Science*, 526:375, 2003.

[56] P. Liu, Y. W. Zhang, and C. Lu. Anisotropy effect on heteroepitaxial growth of self-assembled islands. *Applied Physics Letters*, 88:041922–1, 2006.

[57] C. h. Chui. Stable and uniform arrays of self-assembled nanocrystalline islands. *Physical Review B*, 69:165413, 2004.

[58] C. h. Chui, C.T. Poh, and Z. Huang. Morphological stability of the stranskikrastanow systems under an electric field. *Applied Physics Letters*, 88:241906–1, 2006.

[59] C. h. Chui, Z. Huang, and C.T. Poh. Formation of nanoislands by the electromolding self-organization process. *Physical Review B*, 73:193409–1, 2006.

[60] Y. Pang and R. Huang. Nonlinear effect of stress and wetting on surface evolution of epitaxial thin films. *Physical Review B*, 74:075413–1, 2006.

[61] G. Pandey and R.V. Kukta. Calculation of anisotropic strain-engineered patterns of monolayer islands. *Surface Science*, doi:10.1016/j.susc.2007.06.033:075413–1, 2007.

[62] N.D. Machtay and R.V. Kukta. Energetics of epitaxial island arrangements on substrate mesas. *Journal of Applied Mechanics*, 73:212, 2006.

[63] Ping Liu, Yong-Wei Zhang, Chun Lu, and Khin-Yong Lam. Three-dimensional analysis of the guided-assembled growth of heteroepitaxial islands on imperfectly pre-patterned surfaces. *Nanotechnology*, 19:185302–1–185302–5, 2008.

[64] E. Pan, M. Sun, P. W. Chung, and R. Zhu. Three-dimensional kinetic monte carlo simulation of prepatterned quantum-dot island growth. *Appl. Phys. Lett.*, 91:193110–1–193110–3, 2007.

[65] P. Liu, Y. W. Zhang, and C. Lu. Phase diagrams for growing ordered heteroepitaxial quantum dots and quantum rings by surface prepatterning. *Appl. Phys. Lett.*, 90:071905–1–071905–3, 2007.

[66] N.D. Machtay and R.V. Kukta. Energetics and kinetics of epitaxial island formation on lattice mismatched patterned substrates. *Material Research Society Symposium Proceedings*, 854E:U4.11.1, 2005.

[67] B. J. Spencer and J. Tersoff. Equilibrium shapes of small strain islands. In A. Zangwill *et al.*, editor, *Evolution of Epitaxial Structure and Morpholgy*, volume 399, page 283. Material Research Society Proceedings, Pittsburgh, 1996.

[68] B.J. Spencer and J. Tersoff. Equilibrium shapes and properties of epitaxially strained islands. *Physical Review Letters*, 79(24):4858, 1997.

[69] R. V. Kukta. Mechanics of quantum-dot self-organization by epitaxial growth on small areas. *J. Appl. Mech. - Submitted*, 2008.

[70] C.-H. Chui and Z. Huang. Numerical simuation for the formation of nanostructures on the stranski-krastanow systems by surface undulation. *J. Appl. Phys.*, 101:113540–1–113540–10, 2007.

[71] M. S. Levine, A. A. Golovin, S. H. Davis, and P. W. Voorhees. Self-assembly of quantum dots in a thin epitaxial film wetting an elastic substrate. *Phys. Rev. B*, 75:205312–1–205312–11, 2007.

[72] R. V. Kukta and K. Bhattacharya. A micromechanical model of surface steps. *J. Mech. Phys. Solids*, 50:615–649, 2002.

[73] R. V. Kukta, A. Peralta, and D. Kouris. Elastic interaction of durface steps: Effect of atomic-scale roughness. *Phys. Rev. Lett.*, 88:186102–1–186102–4, 2002.

Appendices

A Complete Mathematical Model Derivation

The system being considered is shown in Figure (5).

The film surface profile can be expressed as the Fourier series

$$z_f(x,y) = \sum_{p,q=-\infty}^{\infty} a_{pq} e^{2\pi i(p\frac{x}{\lambda_x}+q\frac{y}{\lambda_y})} \tag{A.1}$$

and the substrate surface profile can be expressed as the Fourier series

$$z_s(x,y) = \sum_{p,q=-\infty}^{\infty} b_{pq} e^{2\pi i(p\frac{x}{\lambda_x}+q\frac{y}{\lambda_y})} \tag{A.2}$$

where a_{pq} and b_{pq} are the Fourier coefficients for the film and substrate, respectively.

A.1 Elastic Strain Energy

The film surface is traction free, with

$$\sigma_{ij} n_j^f = 0 \tag{A.3}$$

and the tractions on the substrate surface are induced by the difference between the stress fields of the film and substrate. This difference can be expressed as

$$[\![\sigma_{ij}]\!] n_j^s = (\sigma_{ij}^f - \sigma_{ij}^s) n_j^s = 0 \tag{A.4}$$

Where the bracketed term denotes the field resulting from the difference between the film and substrate fields. The combined strain field can also be written as

$$[\![\epsilon_{ij}]\!](\delta_{jk} - n_j^s n_k^s) = \epsilon_{ik}^0 \tag{A.5}$$

where $(\delta_{jk} - n_j^s n_k^s)$ is the projection onto the substrate surface, and ϵ_{ik}^0 is the mismatch strain that results from the discontinuity in strain at the substrate/film interface.

The goal is to find an expression for the energy, U, as a function of the Fourier coefficients of the film and substrate, $U(a_{pq}, b_{pq})$, as an approximation for small slopes. This implies

$$\frac{a_{pq}p}{\lambda_x} \sim \frac{a_{pq}q}{\lambda_y} \sim \frac{b_{pq}p}{\lambda_x} \sim \frac{b_{pq}q}{\lambda_y} \sim \alpha \tag{A.6}$$

where α is small, with the exception of

$$a_{00}, b_{00} \sim O(1) \tag{A.7}$$

which is not small. b_{00} can be taken to be zero, while a_{00} controls the nominal film thickness.

A first order approximation would follow as

$$u \approx u + O(\alpha)^2, \qquad U \approx U + O(\alpha)^3. \tag{A.8}$$

For this investigation, a second order approximation is desired, as governed by

$$u \approx u + O(\alpha)^3, \qquad U \approx U + O(\alpha)^4. \tag{A.9}$$

The elastic field can be represented by a superposition of a known field induced by mismatch between the film and substrate, and an unknown field due to certain applied forces, as shown in Figure (6), and as expressed by

$$\sigma_{ij}^f = \sigma_{ij}^0 + \sigma_{ij}^{f*} \tag{A.10}$$

and

$$\sigma_{ij}^s = \sigma_{ij}^{s*}. \tag{A.11}$$

On the film surface

$$\sigma_{ij}^{f*} n_j^f = -\sigma_{ij}^0 n_j^f \tag{A.12}$$

while on the substrate surface

$$[\![\sigma_{ij}^*]\!] n_j^s = (\sigma_{ij}^{f*} - \sigma_{ij}^{s*}) n_j^s = -\sigma_{ij}^0 n_j^s \tag{A.13}$$

with a strain field expressed as

$$[\![\epsilon_{ij}^*]\!](\delta_{jk} - n_j^s n_k^s) = 0 \tag{A.14}$$

and a displacement continuity constraint,

$$[\![u_i^*]\!] = 0 \tag{A.15}$$

or

$$(u_i^*)^+ = (u_i^*)^- \tag{A.16}$$

The total strain energy of the system can be expressed as

$$\begin{aligned}
U_{tot} &= \frac{1}{2}\int_{V_f} (\sigma_{ij}^0 + \sigma_{ij}^*)(\epsilon_{ij}^0 + \epsilon_{ij}^*)\, dV + \frac{1}{2}\int_{V_s} \sigma_{ij}^* \epsilon_{ij}^*\, dV \\
&= \frac{1}{2}\int_{V_f} \sigma_{ij}^0 \epsilon_{ij}^0\, dV + \int_{V_f} \sigma_{ij}^0 \epsilon_{ij}^*\, dV + \frac{1}{2}\int_{V_f} \sigma_{ij}^* \epsilon_{ij}^*\, dV + \frac{1}{2}\int_{V_s} \sigma_{ij}^* \epsilon_{ij}^*\, dV \\
&= w^0 V_f + \int_{V_f} (\sigma_{ij}^0 u_i^*)_{,j}\, dV + \frac{1}{2}\int_{V_f} (\sigma_{ij}^* u_i^*)_{,j}\, dV + \frac{1}{2}\int_{V_s} (\sigma_{ij}^* u_i^*)_{,j}\, dV \\
&= w^0 V_f + \int_{s_f} (\sigma_{ij}^0 n_j^f u_i^* + \frac{1}{2}\sigma_{ij}^* n_j^f u_i^*)\, dA \\
&\qquad + \int_{s_s} (-\sigma_{ij}^0 n_j^s u_i^* - \frac{1}{2}\sigma_{ij}^{f*} n_j^s u_i^* + \frac{1}{2}\sigma_{ij}^{s*} n_j^s u_i^*)\, dA.
\end{aligned} \tag{A.17}$$

Substituting Equations (A.12) and (A.13) into Equation (A.17) yields

$$U_{tot} = w^0 V_f + \frac{1}{2}\int_{s_f} \sigma_{ij}^0 n_j^f u_i^*\, dA - \frac{1}{2}\int_{s_s} \sigma_{ij}^0 n_j^s u_i^*\, dA. \tag{A.18}$$

For this solution, the displacement field u_i^*, periodic in x and y, is needed. Papkovitch-Neuber potentials will be utilized.

From the linearly elastic stress-displacment relationship

$$\sigma_{ij} = \lambda u_{k,k}\delta_{ij} + \mu(u_{i,j} + u_{j,i}) \tag{A.19}$$

and equilibrium condition

$$\sigma_{ij,j} = 0 \tag{A.20}$$

the constraint

$$(\lambda + \mu)u_{i,ij} + \mu u_{j,ii} = 0 \tag{A.21}$$

can be determined. Applying the Papkovitch-Neuber potentials yields

$$u_i = \phi_i - \frac{1}{4(1-\nu)}(\phi_0 + x - j\phi_j)_{,i} \tag{A.22}$$

where

$$\phi_{0,ii} = \phi_{j,ii} = 0 \tag{A.23}$$

which guarantees that the equilibrium condition, as given in Equation (A.20), is met. Since u_i^* is periodic it is assumed that $\phi_0^* + \phi_i^*$ is also periodic. This periodic potential is truncated to just ϕ_i^*, where $i = 0, 1, 2, 3$, which can be expressed as

$$\phi_k^* = \sum_{p,q=-\infty}^{\infty} F_{kpq}(z) e^{2\pi i(p\frac{x}{\lambda_x} + q\frac{y}{\lambda_y})}. \tag{A.24}$$

Applying the condition set in Equation (B.185) to Equation (B.186) requires that

$$F_{kpq}''(z) - (\frac{4p^2\pi^2}{\lambda_x^2} + \frac{4q^2\pi^2}{\lambda_y^2})F_{kpq}(z) = 0 \tag{A.25}$$

and solving the ODE for $F_{kpq}(z)$ yields

$$F_{kpq}(z) = A_{kpq}e^{2\pi z\sqrt{\frac{p^2}{\lambda_x}+\frac{q^2}{\lambda_y}}} + B_{kpq}e^{-2\pi z\sqrt{\frac{p^2}{\lambda_x}+\frac{q^2}{\lambda_y}}}. \tag{A.26}$$

Periodicity requires that

$$u_x = \phi_1 - \frac{1}{4(1-\nu)}(\phi_0 + x\phi_1 + y\phi_2 + z\phi_3)_{,x}, \tag{A.27}$$

$$u_y = \phi_2 - \frac{1}{4(1-\nu)}(\phi_0 + x\phi_1 + y\phi_2 + z\phi_3)_{,y}, \quad and \tag{A.28}$$

$$u_z = \phi_3 - \frac{1}{4(1-\nu)}(\phi_0 + x\phi_1 + y\phi_2 + z\phi_3)_{,z} \tag{A.29}$$

are periodic in x and y.

Starting with the potential function

$$\phi_i = [B_{i1}(z) + xB_{i2}(z) + yB_{i3}(z)]e^{2\pi i(p\frac{x}{\lambda_x}+q\frac{y}{\lambda_y})} \tag{A.30}$$

restrictions on $B_{ij}(z)$ are determined such that u_i and σ_{ij} are periodic in x and y. This requires that

$$\phi_0 = [B_1(z) - xB_2(z) - yB_3(z)]e^{2\pi i(p\frac{x}{\lambda_x}+q\frac{y}{\lambda_y})}, \tag{A.31}$$

$$\phi_x = B_2(z)e^{2\pi i(p\frac{x}{\lambda_x}+q\frac{y}{\lambda_y})}, \tag{A.32}$$

$$\phi_y = B_3(z)e^{2\pi i(p\frac{x}{\lambda_x}+q\frac{y}{\lambda_y})}, \quad and \tag{A.33}$$

$$\phi_z = B_4(z)e^{2\pi i(p\frac{x}{\lambda_x}+q\frac{y}{\lambda_y})}. \tag{A.34}$$

The displacement equations can then be written as

$$u_x = -\frac{1}{4(1-\nu)}(\phi_0 + z\phi_z)_{,x}, \tag{A.35}$$

$$u_y = -\frac{1}{4(1-\nu)}(\phi_0 + z\phi_z)_{,y}, \quad and \tag{A.36}$$

$$u_z = \phi_z - \frac{1}{4(1-\nu)}(\phi_0 + z\phi_z)_{,z}. \tag{A.37}$$

The potential function

$$\phi_k = \sum_{p,q=-\infty}^{\infty} F_{kpq}(z) e^{2\pi i(p\frac{x}{\lambda_x} + q\frac{y}{\lambda_y})} \tag{A.38}$$

can be determined for the film to be

$$\phi_k^f = \sum_{p,q=-\infty}^{\infty} F_{kpq}^f(z) e^{2\pi i(p\frac{x}{\lambda_x} + q\frac{y}{\lambda_y})} \tag{A.39}$$

and for the substrate to be

$$\phi_k^s = \sum_{p,q=-\infty}^{\infty} F_{kpq}^s(z) e^{2\pi i(p\frac{x}{\lambda_x} + q\frac{y}{\lambda_y})} \tag{A.40}$$

where the film coefficients $F_{kpq}^f(z)$ are requires to satisfy

$$F_{kpq}^f(z) = A_{kpq}^f e^{2\pi z\sqrt{\frac{p^2}{\lambda_x} + \frac{q^2}{\lambda_y}}} + B_{kpq}^f e^{-2\pi z\sqrt{\frac{p^2}{\lambda_x} + \frac{q^2}{\lambda_y}}} \tag{A.41}$$

and the substrate coefficients $F_{kpq}^s(z)$ are required to satisfy

$$F_{kpq}^s(z) = A_{kpq}^s e^{2\pi z\sqrt{\frac{p^2}{\lambda_x} + \frac{q^2}{\lambda_y}}} \tag{A.42}$$

as similarly derived in Equation (B.188). It is noted that $F_{kpq}^s(z)$ decays as z approaches negative infinity ($z \to -\infty$).

A_{kpq}^f, B_{kpq}^f, and A_{kpq}^s are needed, therefore the relations

$$\sigma_{ij}^f n_j^f = -\sigma_{ij}^0 n_j^f \tag{A.43}$$

on the film surface, and

$$[\![\sigma_{ij}]\!] n_j^s = -\sigma_{ij}^0 n_j^s \tag{A.44}$$

and

$$[\![u_i]\!] = u_i^f - u_i^s = 0 \tag{A.45}$$

on the substrate surface are utilized.

Terms in square brackets denote fields that are composed of the field induced by the substrate subtracted from the field induced by the film.

Enforcing Equation (B.207) on the substrate surface, given by

$$z = \sum_{p,q=-\infty}^{\infty} b_{pq} e^{2\pi i(p\frac{x}{\lambda_x}+q\frac{y}{\lambda_y})}, \tag{A.46}$$

with $b_{00} = 0$ and $b_{pq} \sim \alpha$ and restricting that expression to order α^3 yields

$$u_x^f - u_x^s = -\frac{1}{4(1-\nu)}(\phi_0^f + z\phi_z^f)_{,x} - -\frac{1}{4(1-\nu)}(\phi_0^s + z\phi_z^s)_{,x} = 0 \tag{A.47}$$

therefore

$$\phi_{0,x}^f + z\phi_{z,x}^f - \phi_{0,x}^s - z\phi_{z,x}^s = 0 \tag{A.48}$$

on the substrate surface.

Using the potential function

$$\phi_{k,x}^{f,s} = \sum_{p,q=-\infty}^{\infty} F_{kpq}^{f,s}(z)\frac{2\pi ip}{\lambda_x} e^{2\pi i(p\frac{x}{\lambda_x}+q\frac{y}{\lambda_y})} \tag{A.49}$$

and substituting Equation (B.210) into Equation (B.209) yields

$$\sum_{p,q=-\infty}^{\infty} [F_{0pq}^f(z) + zF_{3pq}^f(z) - F_{0pq}^s(z) - zF_{3pq}^s(z)]\frac{2\pi ip}{\lambda_x} e^{2\pi i(p\frac{x}{\lambda_x}+q\frac{y}{\lambda_y})} = 0 \tag{A.50}$$

on the substrate surface.

The term in brackets in Equation (B.211) must then be expanded to $O(\alpha)^3$.

It is noted that, for $b_{00} = 0$

$$z = \sum_{m,n=-\infty}^{\infty} b_{mn} e^{2\pi i(m\frac{x}{\lambda_x} + n\frac{y}{\lambda_y})} \sim \alpha \tag{A.51}$$

and

$$A^f_{kpq} \sim B^f_{kpq} \sim A^s_{kpq} \sim \alpha \tag{A.52}$$

with the exception of A^f_{k00} and A^s_{k00}. Terms proportional to α must vanish as $\alpha \to 0$ ($slope \to 0$). Therefore

$$F^f_{k00} = A^f_{k00} \sim O(1), and \tag{A.53}$$

$$F^s_{k00} = A^s_{k00} \sim O(1). \tag{A.54}$$

On the substrate surface

$$\begin{aligned} F^f_{kpq}(z) &= A^f_{kpq}(1 + 2\pi z\sqrt{\frac{p^2}{\lambda_x^2} + \frac{q^2}{\lambda_y^2}}) + B^f_{kpq}(1 - 2\pi z\sqrt{\frac{p^2}{\lambda_x^2} + \frac{q^2}{\lambda_y^2}}) + O(\alpha)^3 \\ &= A^f_{kpq} + B^f_{kpq} + 2\pi z\sqrt{\frac{p^2}{\lambda_x^2} + \frac{q^2}{\lambda_y^2}}(A^f_{kpq} - B^f_{kpq}) + O(\alpha)^3 \end{aligned} \tag{A.55}$$

$$F^s_{kpq}(z) = A^s_{kpq}(1 + 2\pi z\sqrt{\frac{p^2}{\lambda_x^2} + \frac{q^2}{\lambda_y^2}}) + O(\alpha)^3 \tag{A.56}$$

Substituting Equations (B.216) and (B.217) into Equation (B.211) yields

$$\begin{aligned} \sum_{p,q=-\infty}^{\infty} &[(A^f_{0pq} - A^s_{0pq})(1 + 2\pi z\sqrt{\frac{p^2}{\lambda_x^2} + \frac{q^2}{\lambda_y^2}}) + B^f_{0pq}(1 - 2\pi z\sqrt{\frac{p^2}{\lambda_x^2} + \frac{q^2}{\lambda_y^2}}) \\ &+(A^f_{3pq} - A^s_{3pq})z + B^f_{3pq}z]\frac{2\pi ip}{\lambda_x} e^{2\pi i(p\frac{x}{\lambda_x} + q\frac{y}{\lambda_y})} + O(\alpha)^3 = 0 \end{aligned} \tag{A.57}$$

therefore

$$\begin{aligned} \sum_{p,q=-\infty}^{\infty} &[(A^f_{0pq} - A^s_{0pq} + B^f_{0pq}) + [2\pi\sqrt{\frac{p^2}{\lambda_x^2} + \frac{q^2}{\lambda_y^2}}(A^f_{0pq} - A^s_{0pq} - B^f_{0pq}) \\ &+(A^f_{3pq} - A^s_{3pq} + B^f_{3pq})]z]\frac{2\pi ip}{\lambda_x} e^{2\pi i(p\frac{x}{\lambda_x} + q\frac{y}{\lambda_y})} + O(\alpha)^3 = 0. \end{aligned} \tag{A.58}$$

Substituting Equation (B.212) into Equation (B.219) yields

$$\sum_{p,q=-\infty}^{\infty}[(A_{0pq}^{f}-A_{0pq}^{s}+B_{0pq}^{f})]\frac{2\pi ip}{\lambda_x}e^{2\pi i(p\frac{x}{\lambda_x}+q\frac{y}{\lambda_y})}$$
$$\sum_{p,q=-\infty}^{\infty}\sum_{m,n=-\infty}^{\infty}[2\pi\sqrt{\frac{p^2}{\lambda_x^2}+\frac{q^2}{\lambda_y^2}}(A_{0pq}^{f}-A_{0pq}^{s}-B_{0pq}^{f})$$
$$+(A_{3pq}^{f}-A_{3pq}^{s}+B_{3pq}^{f})]b_{mn}\frac{2\pi ip}{\lambda_x}e^{2\pi i((p+m)\frac{x}{\lambda_x}+(q+n)\frac{y}{\lambda_y})}=O(\alpha)^3 \quad \text{(A.59)}$$

Note that

$$\int_0^{\lambda_x}\int_0^{\lambda_y}e^{-2\pi i(r\frac{x}{\lambda_x}+(s\frac{y}{\lambda_y})}\,dy\,dx=\begin{cases}\lambda_x\lambda_y, & \text{if } r=s=0;\\ 0, & \text{otherwise.}\end{cases} \quad \text{(A.60)}$$

Because of the orthogonality condition, Equation (B.221), $p+m-r=0$ and $q+n-s=0$. Therefore, $m=r-p$ and $n=s-q$. Applying orthogonality to Equation (B.220) produces

$$(A_{0rs}^{f}-A_{0rs}^{s}+B_{0rs}^{f})r+\sum_{p,q=-\infty}^{\infty}[2\pi\sqrt{\frac{p^2}{\lambda_x^2}+\frac{q^2}{\lambda_y^2}}(A_{0pq}^{f}-A_{0pq}^{s}-B_{0pq}^{f})$$
$$+(A_{3pq}^{f}-A_{3pq}^{s}+B_{3pq}^{f})]pb_{r-p,s-q}. \quad \text{(A.61)}$$

From the $[\![u_y]\!]=0$ condition on the substrate surface, it can be similarly determined that

$$(A_{0rs}^{f}-A_{0rs}^{s}+B_{0rs}^{f})s+\sum_{p,q=-\infty}^{\infty}[2\pi\sqrt{\frac{p^2}{\lambda_x^2}+\frac{q^2}{\lambda_y^2}}(A_{0pq}^{f}-A_{0pq}^{s}-B_{0pq}^{f})$$
$$+(A_{3pq}^{f}-A_{3pq}^{s}+B_{3pq}^{f})]qb_{r-p,s-q}. \quad \text{(A.62)}$$

From the $[\![u_z]\!]=0$ condition on the substrate surface, it can be determined that

$$\sum_{p,q=-\infty}^{\infty}[k(A^f_{3pq}-A^s_{3pq}+B^f_{3pq})+2\pi\sqrt{\frac{p^2}{\lambda_x^2}+\frac{q^2}{\lambda_y^2}}(-A^f_{0pq}+A^s_{0pq}+B^f_{0pq})]e^{2\pi i((p)\frac{x}{\lambda_x}+(q)\frac{y}{\lambda_y})}$$
$$+\sum_{p,q=-\infty}^{\infty}\sum_{m,n=-\infty}^{\infty}[2\pi\sqrt{\frac{p^2}{\lambda_x^2}+\frac{q^2}{\lambda_y^2}}k(A^f_{3pq}-A^s_{3pq}-B^f_{3pq})$$
$$+2\pi\sqrt{\frac{p^2}{\lambda_x^2}+\frac{q^2}{\lambda_y^2}}(-A^f_{0pq}+A^s_{0pq}-B^f_{0pq})$$
$$+(-A^f_{3pq}+A^s_{3pq}+B^f_{3pq})]b_{mn}e^{2\pi i((p+m)\frac{x}{\lambda_x}+(q+n)\frac{y}{\lambda_y})}=0 \tag{A.63}$$

where $k=3-4\nu$. Applying orthogonality to Equation (B.224) yields

$$[k(A^f_{3rs}-A^s_{3rs}+B^f_{3rs})+2\pi\sqrt{\frac{r^2}{\lambda_x^2}+\frac{s^2}{\lambda_y^2}}(-A^f_{0rs}+A^s_{0rs}+B^f_{0rs})]$$
$$+\sum_{p,q=-\infty}^{\infty}[2\pi\sqrt{\frac{p^2}{\lambda_x^2}+\frac{q^2}{\lambda_y^2}}k(A^f_{3pq}-A^s_{3pq}-B^f_{3pq})$$
$$+2\pi\sqrt{\frac{p^2}{\lambda_x^2}+\frac{q^2}{\lambda_y^2}}(-A^f_{0pq}+A^s_{0pq}-B^f_{0pq})$$
$$+(-A^f_{3pq}+A^s_{3pq}+B^f_{3pq})]b_{r-p,s-q}=0. \tag{A.64}$$

Equation (B.222) shows that

$$A^f_{0rs}-A^s_{0rs}+B^f_{0rs}=O(\alpha)^2 \tag{A.65}$$

and therefore

$$A^f_{0rs}-A^s_{0rs}=-B^f_{0rs}+O(\alpha)^2. \tag{A.66}$$

In turn, Equation (B.225) shows that

$$k(A^f_{3rs}-A^s_{3rs}+B^f_{3rs})+2\pi\sqrt{\frac{r^2}{\lambda_x^2}+\frac{s^2}{\lambda_y^2}}(-A^f_{0rs}+A^s_{0rs}+B^f_{0rs})=O(\alpha)^2. \tag{A.67}$$

Also, from Equation (B.227),

$$-A^f_{0rs} + A^s_{0rs} + B^f_{0rs} = 2B^f_{0rs} + O(\alpha)^2 \tag{A.68}$$

which, when substituted into Equation (B.228), yields

$$k(A^f_{3rs} - A^s_{3rs} + B^f_{3rs}) = -4\pi B^f_{0rs}\sqrt{\frac{r^2}{\lambda_x^2} + \frac{s^2}{\lambda_y^2}} + O(\alpha)^2. \tag{A.69}$$

Combining these results with Equation (B.222) yields

$$\begin{aligned}(A^f_{0rs} - A^s_{0rs} + B^f_{0rs})r + \sum_{p,q=-\infty}^{\infty} [&-4\pi B^f_{0pq}\sqrt{\frac{p^2}{\lambda_x^2} + \frac{q^2}{\lambda_y^2}} \\ &-\frac{4\pi}{k}B^f_{0pq}\sqrt{\frac{p^2}{\lambda_x^2} + \frac{q^2}{\lambda_y^2}}]pb_{r-p,s-q}\end{aligned} \tag{A.70}$$

which simplifies to

$$(A^f_{0rs} - A^s_{0rs} + B^f_{0rs})r = 4\pi(1 - \frac{1}{k})\sum_{p,q=-\infty}^{\infty} p\sqrt{\frac{p^2}{\lambda_x^2} + \frac{q^2}{\lambda_y^2}}B^f_{0pq}b_{r-p,s-q}$$

Working through the solution for the potential functions, it is found that

$$
\begin{aligned}
\phi_0^f &= \sum_{\substack{p,q=-\infty \\ (p,q)\neq(0,0)}}^{\infty} \Big\{ A_{0pq} e^{2\pi z\sqrt{\frac{p^2}{\lambda_x}+\frac{q^2}{\lambda_y}}} + B_{0pq} e^{-2\pi z\sqrt{\frac{p^2}{\lambda_x}+\frac{q^2}{\lambda_y}}} \\
&+ \frac{\frac{i}{4} A_{1pq} e^{2\pi z\sqrt{\frac{p^2}{\lambda_x}+\frac{q^2}{\lambda_y}}} \lambda_x \lambda_y^2 p(-1+4\pi z\sqrt{\frac{p^2}{\lambda_x}+\frac{q^2}{\lambda_y}})}{\pi(\lambda_y^2 p^2+\lambda_x^2 q^2)} \\
&+ \frac{\frac{-i}{4} B_{1pq} \lambda_x \lambda_y^2 p(1+4\pi z\sqrt{\frac{p^2}{\lambda_x}+\frac{q^2}{\lambda_y}})}{e^{2\pi z\sqrt{\frac{p^2}{\lambda_x}+\frac{q^2}{\lambda_y}}} \pi(\lambda_y^2 p^2+\lambda_x^2 q^2)} \\
&+ \frac{\frac{i}{4} A_{2pq} e^{2\pi z\sqrt{\frac{p^2}{\lambda_x}+\frac{q^2}{\lambda_y}}} \lambda_x^2 \lambda_y q(-1+4\pi z\sqrt{\frac{p^2}{\lambda_x}+\frac{q^2}{\lambda_y}})}{\pi(\lambda_y^2 p^2+\lambda_x^2 q^2)} \\
&+ \frac{\frac{-i}{4} B_{2pq} \lambda_x^2 \lambda_y q(1+4\pi z\sqrt{\frac{p^2}{\lambda_x}+\frac{q^2}{\lambda_y}})}{e^{2\pi z\sqrt{\frac{p^2}{\lambda_x}+\frac{q^2}{\lambda_y}}} \pi(\lambda_y^2 p^2+\lambda_x^2 q^2)} \\
&- x(A_{1pq} e^{2\pi z\sqrt{\frac{p^2}{\lambda_x}+\frac{q^2}{\lambda_y}}} + B_{1pq} e^{-2\pi z\sqrt{\frac{p^2}{\lambda_x}+\frac{q^2}{\lambda_y}}}) \\
&- y(A_{2pq} e^{2\pi z\sqrt{\frac{p^2}{\lambda_x}+\frac{q^2}{\lambda_y}}} + B_{2pq} e^{-2\pi z\sqrt{\frac{p^2}{\lambda_x}+\frac{q^2}{\lambda_y}}}) \Big\} e^{2\pi i(p\frac{x}{\lambda_x}+q\frac{y}{\lambda_y})}, \qquad \text{(A.71)}
\end{aligned}
$$

$$
\phi_x^f = \sum_{\substack{p,q=-\infty \\ (p,q)\neq(0,0)}}^{\infty} \Big\{ A_{1pq} e^{2\pi z\sqrt{\frac{p^2}{\lambda_x}+\frac{q^2}{\lambda_y}}} + B_{1pq} e^{-2\pi z\sqrt{\frac{p^2}{\lambda_x}+\frac{q^2}{\lambda_y}}} \Big\} e^{2\pi i(p\frac{x}{\lambda_x}+q\frac{y}{\lambda_y})}, \qquad \text{(A.72)}
$$

$$
\phi_y^f = \sum_{\substack{p,q=-\infty \\ (p,q)\neq(0,0)}}^{\infty} \Big\{ A_{2pq} e^{2\pi z\sqrt{\frac{p^2}{\lambda_x}+\frac{q^2}{\lambda_y}}} + B_{2pq} e^{-2\pi z\sqrt{\frac{p^2}{\lambda_x}+\frac{q^2}{\lambda_y}}} \Big\} e^{2\pi i(p\frac{x}{\lambda_x}+q\frac{y}{\lambda_y})}, \qquad \text{(A.73)}
$$

$$
\phi_z^f = \sum_{\substack{p,q=-\infty \\ (p,q)\neq(0,0)}}^{\infty} \Big\{ A_{3pq} e^{2\pi z\sqrt{\frac{p^2}{\lambda_x}+\frac{q^2}{\lambda_y}}} + B_{3pq} e^{-2\pi z\sqrt{\frac{p^2}{\lambda_x}+\frac{q^2}{\lambda_y}}} \Big\} e^{2\pi i(p\frac{x}{\lambda_x}+q\frac{y}{\lambda_y})}, \qquad \text{(A.74)}
$$

$$
\begin{aligned}
\phi_0^s &= \sum_{\substack{p,q=-\infty \\ (p,q)\neq(0,0)}}^{\infty} \Big\{ C_{0pq} e^{2\pi z\sqrt{\frac{p^2}{\lambda_x}+\frac{q^2}{\lambda_y}}} \\
&+ \frac{\frac{i}{4} C_{1pq} e^{2\pi z\sqrt{\frac{p^2}{\lambda_x}+\frac{q^2}{\lambda_y}}} \lambda_x \lambda_y^2 p(-1+4\pi z\sqrt{\frac{p^2}{\lambda_x}+\frac{q^2}{\lambda_y}})}{\pi(\lambda_y^2 p^2+\lambda_x^2 q^2)} \\
&+ \frac{\frac{i}{4} C_{2pq} e^{2\pi z\sqrt{\frac{p^2}{\lambda_x}+\frac{q^2}{\lambda_y}}} \lambda_x^2 \lambda_y q(-1+4\pi z\sqrt{\frac{p^2}{\lambda_x}+\frac{q^2}{\lambda_y}})}{\pi(\lambda_y^2 p^2+\lambda_x^2 q^2)} \\
&- x C_{1pq} e^{2\pi z\sqrt{\frac{p^2}{\lambda_x}+\frac{q^2}{\lambda_y}}} - y C_{2pq} e^{2\pi z\sqrt{\frac{p^2}{\lambda_x}+\frac{q^2}{\lambda_y}}} \Big\} e^{2\pi i(p\frac{x}{\lambda_x}+q\frac{y}{\lambda_y})}, \qquad \text{(A.75)}
\end{aligned}
$$

$$
\phi_x^s = \sum_{\substack{p,q=-\infty \\ (p,q)\neq(0,0)}}^{\infty} \Big\{ C_{1pq} e^{2\pi z\sqrt{\frac{p^2}{\lambda_x}+\frac{q^2}{\lambda_y}}} \Big\} e^{2\pi i(p\frac{x}{\lambda_x}+q\frac{y}{\lambda_y})}, \qquad \text{(A.76)}
$$

$$
\phi_y^s = \sum_{\substack{p,q=-\infty \\ (p,q)\neq(0,0)}}^{\infty} \Big\{ C_{2pq} e^{2\pi z\sqrt{\frac{p^2}{\lambda_x}+\frac{q^2}{\lambda_y}}} \Big\} e^{2\pi i(p\frac{x}{\lambda_x}+q\frac{y}{\lambda_y})}, \qquad \text{(A.77)}
$$

and

$$
\phi_z^s = \sum_{\substack{p,q=-\infty \\ (p,q)\neq(0,0)}}^{\infty} \Big\{ C_{3pq} e^{2\pi z\sqrt{\frac{p^2}{\lambda_x}+\frac{q^2}{\lambda_y}}} \Big\} e^{2\pi i(p\frac{x}{\lambda_x}+q\frac{y}{\lambda_y})} \qquad \text{(A.78)}
$$

where

$$
\begin{aligned}
A_{0rs} &= \frac{1}{4e^{4a_{00}\pi\sqrt{R^2+S^2}} M\pi\sqrt{R^2+S^2}} \big\{ ((-1+K)(b_{rs}(K-4a_{00}\pi\sqrt{R^2+S^2}) \\
&+ a_{rs} e^{2a_{00}\pi\sqrt{R^2+S^2}})(-1-K+4a_{00}\pi\sqrt{R^2+S^2}))\sigma_0 \big\} \\
&+ \frac{\frac{i}{8}(8a_{00}(1+K)\pi(R^2+S^2)-\sqrt{R^2+S^2}(1+32a_{00}^2\pi(R^2+S^2)))(RS_1+SS_2)}{e^{4a_{00}\pi\sqrt{R^2+S^2}}(1+K)\pi(R^2+S^2)^{\frac{3}{2}}} \\
&+ \frac{(-16a_{00}^2\pi^2+\frac{-1+K^2}{R^2+S^2})S_3}{16e^{4a_{00}\pi\sqrt{R^2+S^2}} M\pi^2} \\
&+ \frac{\frac{-i}{16}(-1-2K+K^2-4a_{00}(1+K)\pi\sqrt{R^2+S^2}(RS_4+SS_5)}{e^{2a_{00}\pi\sqrt{R^2+S^2}} M\pi^2(R^2+S^2)^{\frac{3}{2}}} \\
&- \frac{(1+K)((-1+K)\sqrt{R^2+S^2}-4a_{00}\pi(R^2+S^2))S_6}{16e^{2a_{00}\pi\sqrt{R^2+S^2}} M\pi^2(R^2+S^2)^{\frac{3}{2}}}, \qquad \text{(A.79)}
\end{aligned}
$$

$$A_{1rs} = \frac{-S_1}{2e^{4a_{00}\pi\sqrt{R^2+S^2}}(1+K)} + \frac{-S_4}{2e^{2a_{00}\pi\sqrt{R^2+S^2}}M\pi\sqrt{R^2+S^2}}, \tag{A.80}$$

$$A_{2rs} = \frac{-S_2}{2e^{4a_{00}\pi\sqrt{R^2+S^2}}(1+K)} + \frac{-S_5}{2e^{2a_{00}\pi\sqrt{R^2+S^2}}M\pi\sqrt{R^2+S^2}}, \tag{A.81}$$

$$\begin{aligned} A_{3rs} &= \frac{(b_{rs} - a_{rs}e^{2a_{00}\pi\sqrt{R^2+S^2}})(-1+K)\sigma_0}{e^{4a_{00}\pi\sqrt{R^2+S^2}}M} \\ &+ \frac{\frac{i}{2}(-1+8a_{00}\pi\sqrt{R^2+S^2})(RS_1+SS_2)}{e^{4a_{00}\pi\sqrt{R^2+S^2}}(1+K)\sqrt{R^2+S^2}} + \frac{(k+4a_{00}\pi\sqrt{R^2+S^2})S_3}{4e^{4a_{00}\pi\sqrt{R^2+S^2}}M\pi\sqrt{R^2+S^2}} \\ &+ \frac{\frac{-i}{2}(-1+K)(RS_4+SS_5)}{e^{2a_{00}\pi\sqrt{R^2+S^2}}M\pi(R^2+S^2)} - \frac{(1+K)S_6}{4e^{2a_{00}\pi\sqrt{R^2+S^2}}M\pi\sqrt{R^2+S^2}}, \end{aligned} \tag{A.82}$$

$$B_{0rs} = \frac{b_r s(-1+K)\sigma_0}{4M\pi\sqrt{R^2+S^2}}, \tag{A.83}$$

$$B_{1rs} = -\frac{(2R^2+S^2)S_1 + RSS_2)}{2(1+K)(R^2+S^2)}, \tag{A.84}$$

$$B_{2rs} = -\frac{RSS_1 + (R^2+2S^2)S_2)}{2(1+K)(R^2+S^2)}, \tag{A.85}$$

$$B_{3rs} = \frac{S_3}{4M\pi\sqrt{R^2+S^2}}, \tag{A.86}$$

$$
\begin{aligned}
C_{0rs} &= \frac{(-a_{rs}+b_{rs}e^{2a_{00}\pi\sqrt{R^2+S^2}})(-1+K)\sigma_0}{4e^{2a_{00}\pi\sqrt{R^2+S^2}}M\pi\sqrt{R^2+S^2}} \\
&+ \frac{(-b_{rs}+a_{rs}e^{2a_{00}\pi\sqrt{R^2+S^2}})(-1+K)(-K+4a_{00}\pi\sqrt{R^2+S^2})\sigma_0}{4e^{4a_{00}\pi\sqrt{R^2+S^2}}M\pi\sqrt{R^2+S^2}} \\
&+ \frac{\frac{i}{8}(RS_1+SS_2)}{e^{4a_{00}\pi\sqrt{R^2+S^2}}(1+K)\pi(R^2+S^2)^{\frac{3}{2}}}\big\{8a_{00}(1+K)\pi(R^2+S^2) \\
&\quad +\sqrt{R^2+S^2}(-1+e^{4a_{00}\pi\sqrt{R^2+S^2}}-32a_{00}^2\pi^2(R^2+S^2))\big\} \\
&+ \frac{(-1+K^2-16a_{00}^2\pi^2(R^2+S^2))S_3}{16e^{4a_{00}\pi\sqrt{R^2+S^2}}M\pi^2(R^2+S^2)} \\
&+ \frac{\frac{-i}{16}(-1-2K+K^2-4a_{00}(1+K)\pi\sqrt{R^2+S^2})(RS_4+SS_5)}{e^{2a_{00}\pi\sqrt{R^2+S^2}}M\pi^2(R^2+S^2)^{\frac{3}{2}}} \\
&- \frac{(1+K)((-1+K)\sqrt{R^2+S^2}-4a_{00}\pi(R^2+S^2))S_6}{16e^{2a_{00}\pi\sqrt{R^2+S^2}}M\pi^2(R^2+S^2)^{\frac{3}{2}}},
\end{aligned} \tag{A.87}
$$

$$
C_{1rs} = \frac{(1-e^{-4a_{00}\pi\sqrt{R^2+S^2}})S_1}{2+2K} - \frac{S_4}{2e^{2a_{00}\pi\sqrt{R^2+S^2}}M\pi\sqrt{R^2+S^2}}, \tag{A.88}
$$

$$
C_{2rs} = \frac{(1-e^{-4a_{00}\pi\sqrt{R^2+S^2}})S_2}{2+2K} - \frac{S_5}{2e^{2a_{00}\pi\sqrt{R^2+S^2}}M\pi\sqrt{R^2+S^2}}, \tag{A.89}
$$

$$
\begin{aligned}
C_{3rs} &= \frac{(b_{rs}-a_{rs}e^{2a_{00}\pi\sqrt{R^2+S^2}})(-1+K)\sigma_0}{e^{4a_{00}\pi\sqrt{R^2+S^2}}M} \\
&+ \frac{\frac{i}{2}(-1+e^{4a_{00}\pi\sqrt{R^2+S^2}}+8a_{00}\pi\sqrt{R^2+S^2})(RS_1+SS_2)}{e^{4a_{00}\pi\sqrt{R^2+S^2}}(1+K)\sqrt{R^2+S^2}} \\
&+ \frac{(e^{4a_{00}\pi\sqrt{R^2+S^2}}+k+4a_{00}\pi\sqrt{R^2+S^2})S_3}{4e^{4a_{00}\pi\sqrt{R^2+S^2}}M\pi\sqrt{R^2+S^2}} \\
&+ \frac{\frac{-i}{2}(-1+K)(RS_4+SS_5)}{e^{2a_{00}\pi\sqrt{R^2+S^2}}M\pi(R^2+S^2)} - \frac{(1+K)S_6}{4e^{2a_{00}\pi\sqrt{R^2+S^2}}M\pi\sqrt{R^2+S^2}},
\end{aligned} \tag{A.90}
$$

$$
S_1 = \sum_{p,q=-\infty}^{\infty} \frac{2ib_{pq}(-1+K)P\pi\sigma_0}{M} b_{r-p,s-q}, \tag{A.91}
$$

$$
S_2 = \sum_{p,q=-\infty}^{\infty} \frac{2ib_{pq}(-1+K)Q\pi\sigma_0}{M} b_{r-p,s-q}, \tag{A.92}
$$

$$S_3 = \sum_{p,q=-\infty}^{\infty} \frac{8b_{pq}(-1+K)\pi^2(PR+QS)\sigma_0}{1+K} b_{r-p,s-q}, \tag{A.93}$$

$$\begin{aligned} S_4 &= \frac{-4i(b_{pq} - a_{pq}e^{2a_{00}\pi\sqrt{P^2+Q^2}})(-1+K)\pi^2}{e^{2a_{00}\pi\sqrt{P^2+Q^2}}(1+K)\sqrt{P^2+Q^2}} \big\{ 4P^2R \\ &\quad -(-3+K)Q^2R + (1+K)PQS\big\}\sigma_0 a_{r-p,s-q}, \end{aligned} \tag{A.94}$$

$$\begin{aligned} S_5 &= \frac{4i(b_{pq} - a_{pq}e^{2a_{00}\pi\sqrt{P^2+Q^2}})(-1+K)\pi^2}{e^{2a_{00}\pi\sqrt{P^2+Q^2}}(1+K)\sqrt{P^2+Q^2}} \big\{ -(1+K)PQR \qquad \text{(A.95)} \\ &\quad +(-3+K)P^2S - 4Q^2S\big\}\sigma_0 a_{r-p,s-q}, \qquad \text{(A.96)} \end{aligned}$$

and

$$S_6 = \sum_{p,q=-\infty}^{\infty} \frac{8a_{pq}(-1+K)\pi^2(PR+QS)\sigma_0}{1+K} a_{r-p,s-q}, \tag{A.97}$$

with

$$P = p\sqrt{\lambda_y/\lambda_x}, \tag{A.98}$$

$$Q = q\sqrt{\lambda_x/\lambda_y}, \tag{A.99}$$

$$R = r\sqrt{\lambda_y/\lambda_x}, \tag{A.100}$$

and

$$S = s\sqrt{\lambda_x/\lambda_y}. \tag{A.101}$$

Therefore, solving for the total strain energy of the system given in Equation (A.18) yields

$$
\begin{aligned}
U_{tot} &= \frac{\sqrt{\lambda_x\lambda_y}^3\pi\sigma_0^2(1-2\nu)^2}{M(1-\nu)}\Bigg\{\frac{\bar{a}_{00}}{2\pi(1+\nu)} \\
&- \sum_{\substack{r,s=-\infty \\ (r,s)\neq(0,0)}}^{\infty} \sqrt{R^2+S^2}(\bar{a}_{-r,-s}-\frac{\bar{b}_{-r,-s}}{e^{2\bar{a}_{00}\pi\sqrt{R^2+S^2}}})(\bar{a}_{r,s}-\frac{\bar{b}_{r,s}}{e^{2\bar{a}_{00}\pi\sqrt{R^2+S^2}}}) \\
&+ 2\pi\sum_{\substack{r,s=-\infty \\ (r,s)\neq(0,0)}}^{\infty}\sum_{\substack{p,q=-\infty \\ (p,q)\neq(0,0)\neq(r,s)}}^{\infty} \sqrt{P^2+Q^2}(\bar{a}_{p,q}-\frac{\bar{b}_{p,q}}{e^{2\bar{a}_{00}\pi\sqrt{P^2+Q^2}}})(2\sqrt{R^2+S^2}(1 \\
&- \frac{(1-\nu)(PS-QR)^2}{(P^2+Q^2)(R^2+S^2))})\bar{a}_{r-p,s-q}(\bar{a}_{-r,-s}-\frac{\bar{b}_{-r,-s}}{e^{2\bar{a}_{00}\pi\sqrt{R^2+S^2}}}) \\
&- \sqrt{P^2+Q^2}(\bar{a}_{-r,-s}\bar{a}_{r-p,s-q}-\frac{\bar{b}_{-r,-s}\bar{b}_{r-p,s-q}}{e^{2\bar{a}_{00}\pi\sqrt{P^2+Q^2}}}))\Bigg\} \qquad \text{(A.102)}
\end{aligned}
$$

and normalizing the total strain energy yields

$$
\begin{aligned}
\bar{U}_{tot} &= U_{tot}\frac{M(1-\nu)}{\sqrt{\lambda_x\lambda_y}^3\pi\sigma_0^2(1-2\nu)^2} \\
&= \frac{\bar{a}_{00}}{2\pi(1+\nu)} \\
&- \sum_{\substack{r,s=-\infty \\ (r,s)\neq(0,0)}}^{\infty} \sqrt{R^2+S^2}(\bar{a}_{-r,-s}-\frac{\bar{b}_{-r,-s}}{e^{2\bar{a}_{00}\pi\sqrt{R^2+S^2}}})(\bar{a}_{r,s}-\frac{\bar{b}_{r,s}}{e^{2\bar{a}_{00}\pi\sqrt{R^2+S^2}}}) \\
&+ 2\pi\sum_{\substack{r,s=-\infty \\ (r,s)\neq(0,0)}}^{\infty}\sum_{\substack{p,q=-\infty \\ (p,q)\neq(0,0)\neq(r,s)}}^{\infty} \sqrt{P^2+Q^2}(\bar{a}_{p,q}-\frac{\bar{b}_{p,q}}{e^{2\bar{a}_{00}\pi\sqrt{P^2+Q^2}}})(2\sqrt{R^2+S^2}(1 \\
&- \frac{(1-\nu)(PS-QR)^2}{(P^2+Q^2)(R^2+S^2))})\bar{a}_{r-p,s-q}(\bar{a}_{-r,-s}-\frac{\bar{b}_{-r,-s}}{e^{2\bar{a}_{00}\pi\sqrt{R^2+S^2}}}) \\
&- \sqrt{P^2+Q^2}(\bar{a}_{-r,-s}\bar{a}_{r-p,s-q}-\frac{\bar{b}_{-r,-s}\bar{b}_{r-p,s-q}}{e^{2\bar{a}_{00}\pi\sqrt{P^2+Q^2}}})) \qquad \text{(A.103)}
\end{aligned}
$$

where

$$
\bar{a}_{m,n} = \frac{a_{m,n}}{\sqrt{\lambda_x\lambda_y}} \qquad \text{(A.104)}
$$

and

$$
\bar{b}_{m,n} = \frac{b_{m,n}}{\sqrt{\lambda_x\lambda_y}}. \qquad \text{(A.105)}
$$

The film surface is defined by the complex Fourier series as

$$z_f(x,y) = \sum_{m,n=-\infty}^{\infty} a_{mn} e^{2\pi i(m\frac{x}{\lambda_x} + n\frac{y}{\lambda_y})} \sim \alpha \tag{A.106}$$

where

$$a_{pq} = \int_0^{\lambda_y} \int_0^{\lambda_x} z_f(x,y) e^{-2\pi i(p\frac{x}{\lambda_x} + q\frac{y}{\lambda_y})}\, dx\, dy. \tag{A.107}$$

Setting

$$\bar{x} = \frac{x}{\lambda_x}, \tag{A.108}$$

$$\bar{y} = \frac{y}{\lambda_y}, \tag{A.109}$$

$$\bar{z_f} = \frac{z_f}{\sqrt{\lambda_x \lambda_y}}, \tag{A.110}$$

and

$$\bar{z_s} = \frac{z_s}{\sqrt{\lambda_x \lambda_y}}, \tag{A.111}$$

Equation (A.106) can be normalized to give

$$\bar{z_f}(x,y) = \sum_{m,n=-\infty}^{\infty} \bar{a}_{mn} e^{2\pi i(m\bar{x} + n\bar{y})} \tag{A.112}$$

where

$$\bar{a}_{pq} = \int_0^1 \int_0^1 \bar{z_f}(x,y) e^{-2\pi i(p\bar{x} + q\bar{y})}\, d\bar{x}\, d\bar{y}. \tag{A.113}$$

The complex coefficients can be expanded as

$$\bar{a}(m,n) = \bar{a}_R(m,n) + i\bar{a}_I(m,n) \tag{A.114}$$

and

$$\bar{b}(m,n) = \bar{b}_R(m,n) + i\bar{b}_I(m,n). \tag{A.115}$$

The normalized complex Fourier series representation of the film surface can then be written as

$$\bar{z_f}(x,y) = \sum_{m,n=-\infty}^{\infty} (\bar{a}_R(m,n) + i\bar{a}_I(m,n))e^{2\pi i(m\bar{x}+n\bar{y})} \tag{A.116}$$

and solving for the imaginary component of Equation (A.116) yields

$$\begin{aligned}
IM[\bar{z_f}(x,y)] &= \bar{a}_I(0,0) \\
&+ \sum_{n=1}^{NN} [(\bar{a}_I(0,-n) + \bar{a}_I(0,n)) \cos 2n\pi\bar{y} + (-\bar{a}_R(0,-n) + \bar{a}_R(0,n)) \sin 2n\pi\bar{y}] \\
&+ \sum_{m=1}^{NN} [(\bar{a}_I(-m,0) + \bar{a}_I(m,0)) \cos 2m\pi\bar{x} + (-\bar{a}_R(-m,0) + \bar{a}_R(m,0)) \sin 2m\pi\bar{x}] \\
&+ \sum_{m,n=1}^{NN} \Big\{ (\bar{a}_I(-m,-n) + \bar{a}_I(-m,n) + \bar{a}_I(m,-n) + \bar{a}_I(m,n)) \\
&\qquad \cos 2m\pi\bar{x} \cos 2n\pi\bar{y} \\
&\quad +(-\bar{a}_R(-m,-n) - \bar{a}_R(-m,n) + \bar{a}_R(m,-n) + \bar{a}_R(m,n)) \\
&\qquad \sin 2m\pi\bar{x} \cos 2n\pi\bar{y} \\
&\quad +(-\bar{a}_R(-m,-n) + \bar{a}_R(-m,n) - \bar{a}_R(m,-n) + \bar{a}_R(m,n)) \\
&\qquad \cos 2m\pi\bar{x} \sin 2n\pi\bar{y} \\
&\quad +(-\bar{a}_I(-m,-n) + \bar{a}_I(-m,n) + \bar{a}_I(m,-n) - \bar{a}_I(m,n)) \\
&\qquad \sin 2m\pi\bar{x} \sin 2n\pi\bar{y} \Big\}
\end{aligned} \tag{A.117}$$

where NN is the number of terms in the Fourier expansion.

Recognizing that the film surface is real, and setting Equation (A.117) equal to zero, a required relationship between the Fourier coefficients can be established;

$$\begin{aligned}
\bar{a}_I(-m,n) &= -\bar{a}_I(m,-n) \\
\bar{a}_I(-m,-n) &= -\bar{a}_I(m,n) \\
\bar{a}_R(-m,n) &= \bar{a}_R(m,-n) \\
\bar{a}_R(-m,-n) &= \bar{a}_R(m,n) \\
\bar{a}_I(0,0) &= 0.
\end{aligned} \tag{A.118}$$

The substrate surface is also real, therefore it can be similarly found that

$$\begin{aligned}
\bar{b}_I(-m,n) &= -\bar{b}_I(m,-n) \\
\bar{b}_I(-m,-n) &= -\bar{b}_I(m,n) \\
\bar{b}_R(-m,n) &= \bar{b}_R(m,-n) \\
\bar{b}_R(-m,-n) &= \bar{b}_R(m,n) \\
\bar{b}_I(0,0) &= 0.
\end{aligned} \tag{A.119}$$

Recall also the $\bar{b}_R(0,0) = 0$ was chosen.

Taking advantage of the relationships given in Equations (A.118) and (A.119) the real part of the normalized film surface expression can be written as

$$\begin{aligned}
RE[\bar{z_f}] &= \bar{a}_R(0,0) \\
&+ 2\sum_{n=1}^{NN} [\bar{a}_R(0,n)\cos 2n\pi\bar{y} - \bar{a}_I(0,n)\sin 2n\pi\bar{y}] \\
&+ 2\sum_{m=1}^{NN} [\bar{a}_R(m,0)\cos 2m\pi\bar{x} - \bar{a}_I(m,0)\sin 2m\pi\bar{x}] \\
&+ 2\sum_{m,n=1}^{NN} \Big\{ (\bar{a}_R(m,-n) + \bar{a}_R(m,n))\cos 2m\pi\bar{x}\cos 2n\pi\bar{y} \\
&\quad -(\bar{a}_I(m,-n) + \bar{a}_I(m,n))\sin 2m\pi\bar{x}\cos 2n\pi\bar{y} \\
&\quad +(\bar{a}_I(m,-n) - \bar{a}_I(m,n))\cos 2m\pi\bar{x}\sin 2n\pi\bar{y} \\
&\quad +(\bar{a}_R(m,-n) - \bar{a}_R(m,n))\sin 2m\pi\bar{x}\sin 2n\pi\bar{y} \Big\}.
\end{aligned} \tag{A.120}$$

Since the imaginary part of the normalized film surface, $\bar{z_f}$, is zero, the real designation can be dropped from Equation (A.120). Therefore

$$\bar{z_f} = RE[\bar{z_f}]. \tag{A.121}$$

With the total strain energy of the system defined as a function of the film surface Fourier coefficients, $U_{tot} = U_{tot}(a_{pq})$, the change in energy with respect to

time can be expressed as

$$\frac{dU_{tot}}{dt} = \int_0^{\lambda_y} \int_0^{\lambda_x} \chi \frac{dz_f}{dt}\, dx\, dy \tag{A.122}$$

where χ is chemical potential. Following the same normalization as before,

$$\frac{\sqrt{\lambda_x \lambda_y}^3 \pi \sigma_0^2 (1-2\nu)^2}{M(1-\nu)} \frac{d\bar{U}_{tot}}{dt} = \sqrt{\lambda_x \lambda_y}^3 \int_0^1 \int_0^1 \chi \frac{d\bar{z}_f}{dt}\, d\bar{x}\, d\bar{y} \tag{A.123}$$

therefore

$$\frac{d\bar{U}_{tot}}{dt} = \frac{M(1-\nu)}{\pi \sigma_0^2 (1-2\nu)^2} \int_0^1 \int_0^1 \chi \frac{d\bar{z}_f}{dt}\, d\bar{x}\, d\bar{y}. \tag{A.124}$$

Now, let

$$\bar{\chi} = \frac{M(1-\nu)}{\pi \sigma_0^2 (1-2\nu)^2} \chi \tag{A.125}$$

therefore

$$\frac{d\bar{U}_{tot}}{dt} = \int_0^1 \int_0^1 \bar{\chi} \frac{d\bar{z}_f}{dt}\, d\bar{x}\, d\bar{y}. \tag{A.126}$$

Taking the function $\bar{U}_{tot} = \bar{U}_{tot}(\bar{a}_{pq})$ given in Equation (A.103),

$$\begin{aligned} \frac{d\bar{U}_{tot}}{dt} &= \sum_{m,n=-\infty}^{\infty} \frac{d\bar{U}_{tot}}{d\bar{a}_{mn}} \frac{d\bar{a}_{mn}}{dt} \\ &= \int_0^1 \int_0^1 \left\{ \bar{\chi} \sum_{m,n=-\infty}^{\infty} \frac{d\bar{a}_{mn}}{dt} e^{2\pi i (m\bar{x} + n\bar{y})} \right\} d\bar{x}\, d\bar{y} \\ &= \sum_{m,n=-\infty}^{\infty} \int_0^1 \int_0^1 \left\{ \bar{\chi} e^{2\pi i (m\bar{x} + n\bar{y})} \frac{d\bar{a}_{mn}}{dt} \right\} d\bar{x}\, d\bar{y}. \end{aligned} \tag{A.127}$$

The normalized chemical potential can be written as

$$\bar{\chi}(x, y) = \sum_{m,n=-\infty}^{\infty} \bar{X}_{mn} e^{2\pi i (m\bar{x} + n\bar{y})} \tag{A.128}$$

where

$$\bar{X}(p,q) = \int_0^1 \int_0^1 \bar{\chi}(x,y) e^{-2\pi i(p\bar{x}+q\bar{y})}\, d\bar{x}\, d\bar{y} \tag{A.129}$$

and therefore

$$\bar{X}(-p,-q) = \int_0^1 \int_0^1 \bar{\chi}(x,y) e^{2\pi i(p\bar{x}+q\bar{y})}\, d\bar{x}\, d\bar{y}. \tag{A.130}$$

Substituting Equation (A.130) into Equation (A.131) yields

$$\begin{aligned} \frac{d\bar{U}_{tot}}{dt} &= \sum_{m,n=-\infty}^{\infty} \frac{d\bar{U}_{tot}}{d\bar{a}_{mn}} \frac{d\bar{a}_{mn}}{dt} \\ &= \sum_{m,n=-\infty}^{\infty} \frac{d\bar{a}_{mn}}{dt} \int_0^1 \int_0^1 \left\{ \bar{\chi} e^{2\pi i(m\bar{x}+n\bar{y})} \right\} d\bar{x}\, d\bar{y} \\ &= \sum_{m,n=-\infty}^{\infty} \bar{X}(-m,-n) \frac{d\bar{a}_{mn}}{dt}. \end{aligned} \tag{A.131}$$

Therefore

$$\bar{X}(-m,-n) = \frac{d\bar{U}_{tot}}{d\bar{a}(m,n)} \tag{A.132}$$

therefore the complex Fourier coefficients of the nondimensional chemical potential and those of the film surface are related through the total nondimensional strain energy by

$$\bar{X}(m,n) = \frac{d\bar{U}_{tot}}{d\bar{a}(-m,-n)}. \tag{A.133}$$

Since the chemical potential is real, as with the film and substrate surfaces,

$$\bar{X}(m,n) = \bar{X}_R(m,n) + i\bar{X}_I(m,n) \tag{A.134}$$

$$\begin{gathered} \bar{X}_I(-m,n) = -\bar{X}_I(m,-n) \\ \bar{X}_I(-m,-n) = -\bar{X}_I(m,n) \\ \bar{X}_R(-m,n) = \bar{X}_R(m,-n) \\ \bar{X}_R(-m,-n) = \bar{X}_R(m,n) \\ \bar{X}_I(0,0) = 0. \end{gathered} \tag{A.135}$$

The real portion of the chemical potential can then be simplified to

$$\begin{aligned} RE[\bar{\chi}] &= \bar{X}_R(0,0) \\ &+ 2\sum_{n=1}^{NN}\left[\bar{X}_R(0,n)\cos 2n\pi\bar{y} - \bar{X}_I(0,n)\sin 2n\pi\bar{y}\right] \\ &+ 2\sum_{m=1}^{NN}\left[\bar{X}_R(m,0)\cos 2m\pi\bar{x} - \bar{X}_I(m,0)\sin 2m\pi\bar{x}\right] \\ &+ 2\sum_{m,n=1}^{NN}\Big\{(\bar{X}_R(m,-n)+\bar{X}_R(m,n))\cos 2m\pi\bar{x}\cos 2n\pi\bar{y} \\ &\quad -(\bar{X}_I(m,-n)+\bar{X}_I(m,n))\sin 2m\pi\bar{x}\cos 2n\pi\bar{y} \\ &\quad +(\bar{X}_I(m,-n)-\bar{X}_I(m,n))\cos 2m\pi\bar{x}\sin 2n\pi\bar{y} \\ &\quad +(\bar{X}_R(m,-n)-\bar{X}_R(m,n))\sin 2m\pi\bar{x}\sin 2n\pi\bar{y}\Big\}. \end{aligned} \tag{A.136}$$

From the inverse Fourier transform and the relations found in Equations (A.135),

$$\int_0^1\int_0^1 \bar{\chi}(x,y)\cos 2\pi i(p\bar{x}+q\bar{y})\,d\bar{x}\,d\bar{y} = \frac{\bar{X}_R(p,q)+\bar{X}_R(-p,-q)}{2} \tag{A.137}$$

and

$$\int_0^1\int_0^1 -\bar{\chi}(x,y)\sin 2\pi i(p\bar{x}+q\bar{y})\,d\bar{x}\,d\bar{y} = \frac{\bar{X}_I(p,q)-\bar{X}_I(-p,-q)}{2}. \tag{A.138}$$

From $\bar{U}_{tot} = \bar{U}_{tot}(\bar{a}_{pq}) = \bar{U}_{tot}(\bar{a}_R(p,q), \bar{a}_I(p,q))$,

$$
\begin{aligned}
\frac{d\bar{U}_{tot}}{dt} &= \sum_{m,n=-\infty}^{\infty} \Big\{ \frac{d\bar{U}_{tot}}{d\bar{a}_R(m,n)} \frac{d\bar{a}_R(m,n)}{dt} + \frac{d\bar{U}_{tot}}{d\bar{a}_I(m,n)} \frac{d\bar{a}_I(m,n)}{dt} \Big\} \\
&= \int_0^1 \int_0^1 \bar{\chi} \frac{d\bar{z}_f}{dt}\, d\bar{x}\, d\bar{y} \\
&= \int_0^1 \int_0^1 \bar{\chi} \sum_{m,n=-\infty}^{\infty} \Big\{ \frac{d\bar{z}_f}{d\bar{a}_R(m,n)} \frac{d\bar{a}_R(m,n)}{dt} + \frac{d\bar{z}_f}{d\bar{a}_I(m,n)} \frac{d\bar{a}_I(m,n)}{dt} \Big\}\, d\bar{x}\, d\bar{y} \\
&= \sum_{m,n=-\infty}^{\infty} \int_0^1 \int_0^1 \bar{\chi} \Big\{ \frac{d\bar{z}_f}{d\bar{a}_R(m,n)} \frac{d\bar{a}_R(m,n)}{dt} + \frac{d\bar{z}_f}{d\bar{a}_I(m,n)} \frac{d\bar{a}_I(m,n)}{dt} \Big\}\, d\bar{x}\, d\bar{y} \\
&= \sum_{m,n=-\infty}^{\infty} \int_0^1 \int_0^1 \bar{\chi} \Big\{ \cos 2\pi i(m\bar{x} + n\bar{y}) \frac{d\bar{a}_R(m,n)}{dt} \\
&\qquad\qquad - \sin 2\pi i(m\bar{x} + n\bar{y}) \frac{d\bar{a}_I(m,n)}{dt} \Big\}\, d\bar{x}\, d\bar{y} \\
&= \sum_{m,n=-\infty}^{\infty} \int_0^1 \int_0^1 \bar{\chi} \Big\{ \cos 2\pi i(m\bar{x} + n\bar{y}) \frac{d\bar{a}_R(m,n)}{dt} \Big\}\, d\bar{x}\, d\bar{y} \\
&\quad + \sum_{m,n=-\infty}^{\infty} \int_0^1 \int_0^1 -\bar{\chi} \Big\{ \sin 2\pi i(m\bar{x} + n\bar{y}) \frac{d\bar{a}_I(m,n)}{dt} \Big\}\, d\bar{x}\, d\bar{y} \qquad \text{(A.139)} \\
& \qquad\qquad\qquad\qquad\qquad\qquad\qquad\qquad\qquad\qquad\qquad\qquad\qquad\qquad \text{(A.140)}
\end{aligned}
$$

therefore

$$
\frac{d\bar{U}_{tot}}{d\bar{a}_R(p,q)} = \int_0^1 \int_0^1 \bar{\chi}(x,y) \cos 2\pi i(p\bar{x} + q\bar{y})\, d\bar{x}\, d\bar{y} = \frac{\bar{X}_R(p,q) + \bar{X}_R(-p,-q)}{2} \qquad \text{(A.141)}
$$

and

$$
\frac{d\bar{U}_{tot}}{d\bar{a}_I(p,q)} = \int_0^1 \int_0^1 -\bar{\chi}(x,y) \sin 2\pi i(p\bar{x} + q\bar{y})\, d\bar{x}\, d\bar{y} = \frac{\bar{X}_I(p,q) - \bar{X}_I(-p,-q)}{2}. \qquad \text{(A.142)}
$$

From Equations (A.135), (A.141), and (A.142) it is concluded that

$$
\bar{X}_R(p,q) = \frac{d\bar{U}_{tot}}{d\bar{a}_R(p,q)} \qquad \text{(A.143)}
$$

and

$$\bar{X}_I(p,q) = \frac{d\bar{U}_{tot}}{d\bar{a}_I(p,q)}. \tag{A.144}$$

A.2 Surface Free Energy

The contribution of the surface energy to the chemical potential must also be considered. The area of the film surface, S, is given by

$$\begin{aligned} S &= \int_0^{\lambda_y}\int_0^{\lambda_x} \sqrt{\Big(\frac{dz_f}{dx}\Big)^2 + \Big(\frac{dz_f}{dy}\Big)^2 + 1}\, dx\, dy \\ &= \lambda_x\lambda_y \int_0^1\int_0^1 \sqrt{\frac{\lambda_y}{\lambda_x}\Big(\frac{d\bar{z}_f}{d\bar{x}}\Big)^2 + \frac{\lambda_x}{\lambda_y}\Big(\frac{d\bar{z}_f}{d\bar{y}}\Big)^2 + 1}\, d\bar{x}\, d\bar{y}. \end{aligned} \tag{A.145}$$

The integrand can be simplified by dropping the higher order terms, as per

$$\sqrt{\frac{\lambda_y}{\lambda_x}\Big(\frac{d\bar{z}_f}{d\bar{x}}\Big)^2 + \frac{\lambda_x}{\lambda_y}\Big(\frac{d\bar{z}_f}{d\bar{y}}\Big)^2 + 1} = \frac{1}{2}\frac{\lambda_y}{\lambda_x}\Big(\frac{d\bar{z}_f}{d\bar{x}}\Big)^2 + \frac{1}{2}\frac{\lambda_x}{\lambda_y}\Big(\frac{d\bar{z}_f}{d\bar{y}}\Big)^2 + 1 + O(\alpha)^3 \tag{A.146}$$

where the higher order terms are not considered. Also, from the Fourier expansion of $\bar{z}_f$ it can be shown that

$$\Big(\frac{d\bar{z}_f}{d\bar{x}}\Big)^2 = \sum_{m,n=-\infty}^{\infty}\sum_{p,q=-\infty}^{\infty} (-4\pi^2) mp\bar{a}(m,n)\bar{a}(p,q)e^{2\pi i((m+p)\bar{x}+(n+q)\bar{y})} \tag{A.147}$$

and

$$\Big(\frac{d\bar{z}_f}{d\bar{y}}\Big)^2 = \sum_{m,n=-\infty}^{\infty}\sum_{p,q=-\infty}^{\infty} (-4\pi^2) nq\bar{a}(m,n)\bar{a}(p,q)e^{2\pi i((m+p)\bar{x}+(n+q)\bar{y})}. \tag{A.148}$$

The surface area can then be expressed as

$$
\begin{aligned}
S &= \lambda_x\lambda_y \int_0^1 \int_0^1 \left\{ \frac{1}{2}\frac{\lambda_y}{\lambda_x}\Big(\frac{d\bar{z}_f}{d\bar{x}}\Big)^2 + \frac{1}{2}\frac{\lambda_x}{\lambda_y}\Big(\frac{d\bar{z}_f}{d\bar{y}}\Big)^2 + 1 \right\} d\bar{x}\, d\bar{y} \\
&= \lambda_x\lambda_y \Bigg(1 - 2\pi^2 \int_0^1 \int_0^1 \Big\{ \sum_{m,n=-\infty}^{\infty} \sum_{p,q=-\infty}^{\infty} \big[\bar{a}(m,n)\bar{a}(p,q) \\
&\qquad e^{2\pi i((m+p)\bar{x}+(n+q)\bar{y})} \big(\frac{\lambda_y}{\lambda_x} mp + \frac{\lambda_x}{\lambda_y} nq \big) \big] \Big\} d\bar{x} d\bar{y} \Bigg). \qquad \text{(A.149)}
\end{aligned}
$$

Applying orthogonality to Equation (A.149) yields

$$
S = \lambda_x\lambda_y \Big(1 + 2\pi^2 \sum_{p,q=-\infty}^{\infty} \big[\bar{a}(-p,-q)\bar{a}(p,q) \big(\frac{\lambda_y}{\lambda_x} p^2 + \frac{\lambda_x}{\lambda_y} q^2 \big) \big] \Big). \qquad \text{(A.150)}
$$

In the interest of simplicity, the case where the surface energy density, γ, is constant and isotropic is considered. The surface free energy can then be expressed as

$$
\gamma S = \gamma\lambda_x\lambda_y \Big(1 + 2\pi^2 \sum_{p,q=-\infty}^{\infty} \big[\bar{a}(-p,-q)\bar{a}(p,q) \big(\frac{\lambda_y}{\lambda_x} p^2 + \frac{\lambda_x}{\lambda_y} q^2 \big) \big] \Big). \qquad \text{(A.151)}
$$

and conducting the energy normalization as before,

$$
\overline{\gamma S} = \frac{\mu(1-\nu)\gamma}{\sqrt{\lambda_x\lambda_y}\pi\sigma_0^2(1-2\nu)^2} \Big(1 + 2\pi^2 \sum_{p,q=-\infty}^{\infty} \big[\bar{a}(-p,-q)\bar{a}(p,q) \big(\frac{\lambda_y}{\lambda_x} p^2 + \frac{\lambda_x}{\lambda_y} q^2 \big) \big] \Big). \qquad \text{(A.152)}
$$

Expanding the complex Fourier coefficients and recognizing that the surface is real, it can be determined that

$$
\begin{aligned}
\overline{\gamma S} &= \frac{\mu(1-\nu)\gamma}{\sqrt{\lambda_x\lambda_y}\pi\sigma_0^2(1-2\nu)^2} \Big(1 + 2\pi^2 \sum_{p,q=-\infty}^{\infty} \big[\bar{a}_R(-p,-q)\bar{a}_R(p,q) \\
&\qquad -\bar{a}_I(-p,-q)\bar{a}_I(p,q) \big] \big(\frac{\lambda_y}{\lambda_x} p^2 + \frac{\lambda_x}{\lambda_y} q^2 \big) \Big). \qquad \text{(A.153)}
\end{aligned}
$$

The derivatives of the normalized surface energy with respect to the real and imaginary surface Fourier coefficients can then be evaluated,

$$\frac{\overline{\gamma S}}{d\bar{a}_R(m,n)} = \frac{4\mu(1-\nu)\gamma\pi}{\sqrt{\lambda_x\lambda_y}\sigma_0^2(1-2\nu)^2}\big(\frac{\lambda_y}{\lambda_x}m^2 + \frac{\lambda_x}{\lambda_y}n^2\big)\bar{a}_R(-m,-n) \tag{A.154}$$

and

$$\frac{\overline{\gamma S}}{d\bar{a}_I(m,n)} = \frac{-4\mu(1-\nu)\gamma\pi}{\sqrt{\lambda_x\lambda_y}\sigma_0^2(1-2\nu)^2}\big(\frac{\lambda_y}{\lambda_x}m^2 + \frac{\lambda_x}{\lambda_y}n^2\big)\bar{a}_I(-m,-n). \tag{A.155}$$

It is further noted that the mismatch stress, σ_0, can be expressed in terms of more readily useful mismatch strain, ϵ_0 as per the constitutive relation

$$\sigma_0 = \frac{\mu(1-\nu)}{(1-2\nu)^2}\epsilon_0. \tag{A.156}$$

Equations (A.154) and (A.155) can then be expressed in terms of the mismatch strain,

$$\frac{\overline{\gamma S}}{d\bar{a}_R(m,n)} = \frac{4(1-2\nu)^2\gamma\pi}{\sqrt{\lambda_x\lambda_y}\mu(1-\nu)\epsilon_0^2}\big(\frac{\lambda_y}{\lambda_x}m^2 + \frac{\lambda_x}{\lambda_y}n^2\big)\bar{a}_R(-m,-n) \tag{A.157}$$

and

$$\frac{\overline{\gamma S}}{d\bar{a}_I(m,n)} = \frac{4(1-2\nu)^2\gamma\pi}{\sqrt{\lambda_x\lambda_y}\mu(1-\nu)\epsilon_0^2}\big(\frac{\lambda_y}{\lambda_x}m^2 + \frac{\lambda_x}{\lambda_y}n^2\big)\bar{a}_I(-m,-n). \tag{A.158}$$

A.3 Combined Elastic Strain and Surface Free Energy

The form of the chemical potential coefficients can then be expanded to include the surface free energy:

$$\bar{X}_R(p,q) = \frac{d\bar{U}_{tot}}{d\bar{a}_R(p,q)} + \frac{\overline{\gamma S}}{d\bar{a}_R(p,q)} \tag{A.159}$$

and

$$\bar{X}_I(p,q) = \frac{d\bar{U}_{tot}}{d\bar{a}_I(p,q)} + \frac{\overline{\gamma S}}{d\bar{a}_I(p,q)}. \tag{A.160}$$

This can in turn be expanded to

$$\bar{X}_R(p,q) = \frac{d\bar{U}_{tot}}{d\bar{a}_R(p,q)} + \bar{L^*}\big(\frac{\lambda_y}{\lambda_x}m^2 + \frac{\lambda_x}{\lambda_y}n^2\big)\bar{a}_R(-m,-n) \tag{A.161}$$

and

$$\bar{X}_I(p,q) = \frac{d\bar{U}_{tot}}{d\bar{a}_I(p,q)} + \bar{L^*}\big(\frac{\lambda_y}{\lambda_x}m^2 + \frac{\lambda_x}{\lambda_y}n^2\big)\bar{a}_I(-m,-n) \tag{A.162}$$

where

$$\bar{L^*} = \frac{4(1-2\nu)^2\gamma\pi}{\sqrt{\lambda_x\lambda_y}\mu(1-\nu)\epsilon_0^2}. \tag{A.163}$$

The normalized characteristic length, $\bar{L^*}$, specifies the balance point between surface free energy and elastic strain energy. For example, a higher value of $\bar{L^*}$ could imply that either the surface energy density, γ, has increased, or else the mismatch strain, ϵ_0 has been reduced, in either case leading to an increased influence of surface free energy over elastic strain energy. Inversely, a decrease in $\bar{L^*}$ could imply a drop in surface energy density, or an increase in mismatch strain, in both cases resulting in an increased importance of elastic strain energy over surface free energy. By comparing the behavior and response of a system to a range of $\bar{L^*}$ values, the relative effects of surface free energy and elastic strain energy can be evaluated and analyzed.

To determine the relationship between chemical potential and surface velocity, first select an orthogonal system on the film surface (S_1, S_2), and including the normal to the film surface $(\hat{n})$, as shown in Figure (7).

The directions S_1 and S_2 are selected such that

$$S_1 = S_1(x, z_f) \tag{A.164}$$

and

$$S_2 = S_2(y, z_f). \tag{A.165}$$

From the Pythagorean theorem

$$\frac{dS_1}{dx} = \sqrt{\left(\frac{dz_f}{dx}\right)^2 + \left(\frac{dx}{dx}\right)^2} = \sqrt{\left(\frac{dz_f}{dx}\right)^2 + 1} \tag{A.166}$$

and similarly

$$\frac{dS_2}{dy} = \sqrt{\left(\frac{dz_f}{dy}\right)^2 + \left(\frac{dy}{dy}\right)^2} = \sqrt{\left(\frac{dz_f}{dy}\right)^2 + 1} \tag{A.167}$$

The film surface is defined by $z_f = z_f(x, y)$, therefore the normal to the film surface is

$$\hat{n} = \frac{\nabla z_f}{|\nabla z_f|} = \frac{\left(\frac{dz_f}{dx}, \frac{dz_f}{dy}, 1\right)}{\sqrt{\left(\frac{dz_f}{dx}\right)^2 + \left(\frac{dz_f}{dy}\right)^2 + 1}} \tag{A.168}$$

Consider some function f on the surface of the film. The surface laplacian is given by

$$\begin{aligned}
\nabla_s^2 f &= \frac{\partial^2 f}{\partial S_1^2} + \frac{\partial^2 f}{\partial S_2^2} = \frac{\partial}{\partial S_1}\left(\frac{\partial f}{\partial x}\frac{\partial x}{\partial S_1}\right) + \frac{\partial}{\partial S_2}\left(\frac{\partial f}{\partial y}\frac{\partial y}{\partial S_2}\right) \\
&= \frac{\partial}{\partial x}\left(\frac{\partial f}{\partial x}\frac{\partial x}{\partial S_1}\right)\frac{\partial x}{\partial S_1} + \frac{\partial}{\partial y}\left(\frac{\partial f}{\partial y}\frac{\partial y}{\partial S_2}\right)\frac{\partial y}{\partial S_2} \\
&= \frac{\partial^2 f}{\partial x^2}\left(\frac{\partial x}{\partial S_1}\right)^2 + \frac{\partial f}{\partial x}\frac{\partial^2 x}{\partial x \partial S_1}\frac{\partial x}{\partial S_1} + \frac{\partial^2 f}{\partial y^2}\left(\frac{\partial y}{\partial S_2}\right)^2 + \frac{\partial f}{\partial y}\frac{\partial^2 y}{\partial y \partial S_2}\frac{\partial y}{\partial S_2} \\
&= \frac{\partial^2 f}{\partial x^2}\left(\frac{1}{\left(\frac{dz_f}{dx}\right)^2 + 1}\right) + \frac{\partial^2 f}{\partial y^2}\left(\frac{1}{\left(\frac{dz_f}{dy}\right)^2 + 1}\right)
\end{aligned} \tag{A.169}$$

The film surface velocity in the normal direction is given by

$$\begin{aligned}
v_n &= M_s \nabla_s^2 \chi \\
&= M_s \left\{ \frac{\partial^2 \chi}{\partial x^2}\left(\frac{1}{\left(\frac{dz_f}{dx}\right)^2 + 1}\right) + \frac{\partial^2 \chi}{\partial y^2}\left(\frac{1}{\left(\frac{dz_f}{dy}\right)^2 + 1}\right) \right\}
\end{aligned} \tag{A.170}$$

where M_s is the surface mobility coefficient.

The component of the surface velocity in the vertical direction is

$$
\begin{aligned}
v_z &= \frac{dz_f}{dt} = v_n \hat{n} \cdot \hat{k} \\
&= \frac{M_s \left\{ \frac{\partial^2 \chi}{\partial x^2} \left(\frac{1}{\left(\frac{dz_f}{dx}\right)^2 + 1} \right) + \frac{\partial^2 \chi}{\partial y^2} \left(\frac{1}{\left(\frac{dz_f}{dy}\right)^2 + 1} \right) \right\}}{\sqrt{\left(\frac{dz_f}{dx}\right)^2 + \left(\frac{dz_f}{dy}\right)^2 + 1}} \\
&= \frac{M_s \left\{ \frac{\partial^2 \chi}{\partial x^2} \left(\left(\frac{dz_f}{dy}\right)^2 + 1 \right) + \frac{\partial^2 \chi}{\partial y^2} \left(\left(\frac{dz_f}{dx}\right)^2 + 1 \right) \right\}}{\left(\left(\frac{dz_f}{dx}\right)^2 + 1 \right) \left(\left(\frac{dz_f}{dy}\right)^2 + 1 \right) \sqrt{\left(\frac{dz_f}{dx}\right)^2 + \left(\frac{dz_f}{dy}\right)^2 + 1}} \\
&= M_s \left\{ \frac{\partial^2 \chi}{\partial x^2} + \frac{\partial^2 \chi}{\partial y^2} \right\} + O(\alpha)^3 \qquad \text{(A.171)}
\end{aligned}
$$

as $z_{,x}, z_{,y}, \chi_{,xx}, \chi_{,yy} \sim \alpha$.

Conducting the same normalization procedure as used previously yields

$$
\frac{d\bar{z}_f}{d\bar{t}} = \left(\frac{\lambda_y}{\lambda_x} \frac{d^2 \bar{\chi}}{d\bar{x}^2} + \frac{\lambda_x}{\lambda_y} \frac{d^2 \bar{\chi}}{d\bar{y}^2} \right) \qquad \text{(A.172)}
$$

where

$$
\bar{t} = \frac{t}{\tau}. \qquad \text{(A.173)}
$$

and the time normalization factor is

$$
\tau = \frac{(1-2\nu)^2 (\lambda_x \lambda_y)^{\frac{3}{2}}}{M_s \mu (1-\nu) \pi \epsilon_0^2}. \qquad \text{(A.174)}
$$

From the form of the normalized chemical potential given in Equation (A.136) the required second derivative terms appearing in Equation (A.172) can be evaluated as

$$
\begin{aligned}
\frac{d^2 \bar{\chi}}{d\bar{x}^2} &= 2 \sum_{m=1}^{NN} 4M^2 \pi^2 \left(\bar{X}_I(m,0) \sin 2M\pi\bar{x} - \bar{X}_R(m,0) \cos 2M\pi\bar{x} \right) \\
&+ 2 \sum_{m,n=1}^{NN} 4M^2 \pi^2 \big(\bar{X}_I(m,-n) \sin 2\pi(M\bar{x} - N\bar{y}) + \bar{X}_I(m,n) \sin 2\pi(M\bar{x} + N\bar{y}) \\
&\quad - \bar{X}_R(m,-n) \cos 2\pi(M\bar{x} - N\bar{y}) - \bar{X}_R(m,n) \cos 2\pi(M\bar{x} + N\bar{y}) \big) \qquad \text{(A.175)}
\end{aligned}
$$

and

$$\begin{aligned}\frac{d^2\bar{\chi}}{d\bar{y}^2} &= 2\sum_{n=1}^{NN} 4N^2\pi^2\big(\bar{X}_I(0,n)\sin 2N\pi\bar{y} - \bar{X}_R(0,n)\cos 2N\pi\bar{y}\big) \\ &+ 2\sum_{m,n=1}^{NN} 4N^2\pi^2\big(\bar{X}_I(m,-n)\sin 2\pi(M\bar{x}-N\bar{y}) + \bar{X}_I(m,n)\sin 2\pi(M\bar{x}+N\bar{y}) \\ &\quad -\bar{X}_R(m,-n)\cos 2\pi(M\bar{x}-N\bar{y}) - \bar{X}_R(m,n)\cos 2\pi(M\bar{x}+N\bar{y})\big). \quad \text{(A.176)}\end{aligned}$$

Substituting Equations (A.175) and (A.176) into Equation (A.172) yields

$$\begin{aligned}\frac{d\bar{z}_f}{d\bar{t}} &= \left(\frac{\lambda_y}{\lambda_x}\frac{d^2\bar{\chi}}{d\bar{x}^2} + \frac{\lambda_x}{\lambda_y}\frac{d^2\bar{\chi}}{d\bar{y}^2}\right) \\ &= 2\sum_{m=1}^{NN} 4\frac{\lambda_y}{\lambda_x}M^2\pi^2\big(\bar{X}_I(m,0)\sin 2M\pi\bar{x} - \bar{X}_R(m,0)\cos 2M\pi\bar{x}\big) \\ &+ 2\sum_{n=1}^{NN} 4\frac{\lambda_x}{\lambda_y}N^2\pi^2\big(\bar{X}_I(0,n)\sin 2\frac{\lambda_x}{\lambda_y}N\pi\bar{y} - \bar{X}_R(0,n)\cos 2N\pi\bar{y}\big) \\ &+ 2\sum_{m,n=1}^{NN} \frac{4(\lambda_y^2M^2+\lambda_x^2N^2)\pi^2}{\lambda_x\lambda_y}\big\{ -\bar{X}_R(m,-n)\cos 2\pi(M\bar{x}-N\bar{y}) \\ &\qquad -\bar{X}_R(m,n)\cos 2\pi(M\bar{x}+N\bar{y}) \\ &\qquad +\bar{X}_I(m,-n)\sin 2\pi(M\bar{x}-N\bar{y}) \\ &\qquad +\bar{X}_I(m,n)\sin 2\pi(M\bar{x}+N\bar{y})\big\}. \quad \text{(A.177)}\end{aligned}$$

The vertical velocity of the film surface can also be evaluated as the time derivative of the Fourier expansion given in Equation (A.120)

$$
\begin{aligned}
\frac{d\bar{z}_f}{d\bar{t}} &= \frac{\bar{a}_R(0,0)}{d\bar{t}} \\
&+ 2\sum_{n=1}^{NN}\left[\frac{\bar{a}_R(0,n)}{d\bar{t}}\cos 2n\pi\bar{y} - \frac{\bar{a}_I(0,n)}{d\bar{t}}\sin 2n\pi\bar{y}\right] \\
&+ 2\sum_{m=1}^{NN}\left[\frac{\bar{a}_R(m,0)}{d\bar{t}}\cos 2m\pi\bar{x} - \frac{\bar{a}_I(m,0)}{d\bar{t}}\sin 2m\pi\bar{x}\right] \\
&+ 2\sum_{m,n=1}^{NN}\left\{\frac{\bar{a}_R(m,-n)}{d\bar{t}}\cos 2\pi(M\bar{x}-N\bar{y})\right. \\
&\qquad + \frac{\bar{a}_R(m,n)}{d\bar{t}}\cos 2\pi(M\bar{x}+N\bar{y}) \\
&\qquad - \frac{\bar{a}_I(m,-n)}{d\bar{t}}\sin 2\pi(M\bar{x}-N\bar{y}) \\
&\qquad \left. - \frac{\bar{a}_I(m,n)}{d\bar{t}}\sin 2\pi(M\bar{x}+N\bar{y})\right\}. \qquad \text{(A.178)}
\end{aligned}
$$

By comparing the terms in Equations (A.177) and (A.178) it is determined that

$$
\frac{\bar{a}_R(m,n)}{d\bar{t}} = -\frac{4(\lambda_y^2M^2+\lambda_x^2N^2)\pi^2}{\lambda_x\lambda_y}\bar{X}_R(m,n) \qquad \text{(A.179)}
$$

and

$$
\frac{\bar{a}_I(m,n)}{d\bar{t}} = -\frac{4(\lambda_y^2M^2+\lambda_x^2N^2)\pi^2}{\lambda_x\lambda_y}\bar{X}_I(m,n). \qquad \text{(A.180)}
$$

The evolution of the film can then be conducted spectrally using the results in Equations (A.179) and (A.180) along with a desired time stepping routine.

A.4 Film/Substrate Interfacial Interaction Energy

In order to insure that the film evolution responds appropriately to the substrate surface, and a wetting layer typical for SK growth is maintained, a film/substrate interface interaction contribution to the chemical potential is also considered. The model employed to account for this effect was used previously [7,57–59]. The energy density of the film and substrate interface is first taken as

$$g(z_f) = \frac{g_0 l^p}{(z_f - z_s + l)^p} \tag{A.181}$$

where g_0 and l are material properties. The exponent term p varies depending on the interaction mechanism being considered [7, 57–59].

The contribution of this interaction energy to the chemical potential is

$$\bar{\chi}_{int} = \Omega n_z \frac{\partial g(z_f)}{\partial z_f} = \frac{-\Omega g_0 l}{\sqrt{\left(\frac{dz_f}{dx}\right)^2 + \left(\frac{dz_f}{dy}\right)^2 + 1}\left(z_f - z_s + l\right)^2} \tag{A.182}$$

Where Ω is the atomic volume, g_0 is the atomic density of the interface, and l is the relevant length scale factor. Equation (A.182) can be expressed in terms of the normalized surface profiles as

$$\bar{\chi}_{int} = \frac{-\Omega g_0 \bar{l}}{\sqrt{\left(\frac{\lambda_y}{\lambda_x}\frac{d\bar{z}_f}{d\bar{x}}\right)^2 + \frac{\lambda_x}{\lambda_y}\left(\frac{d\bar{z}_f}{d\bar{y}}\right)^2 + 1}\left(\bar{z}_f - \bar{z}_s + \bar{l}\right)^2 \sqrt{\lambda_x \lambda_y}} \tag{A.183}$$

where

$$\bar{l} = \frac{l}{\sqrt{\lambda_x \lambda_y}}. \tag{A.184}$$

The contribution of the interface to the chemical potential can then be incorporated into the evolution process, noting that due to the inverse dependence on the film thickness, the term will only be significantly expressed for instances where the film has become very thin.

B Potential Function Derivation

The Papkovitch-Neuber potentials are required to satisfy the condition

$$\phi_{0,ii} = \phi_{j,ii} = 0 \tag{B.185}$$

which guarantees that the equilibrium condition, as given in Equation (A.20), is met. Since u_i^* is periodic it is assumed that $\phi_0^* + \phi_i^*$ is also periodic. This periodic potential is truncated to just ϕ_i^*, where $i = 0, 1, 2, 3$, which can be expressed as

$$\phi_k^* = \sum_{p,q=-\infty}^{\infty} F_{kpq}(z)\, e^{2\pi i\left(p\frac{x}{\lambda_x} + q\frac{y}{\lambda_y}\right)}. \tag{B.186}$$

Applying the condition set in Equation (B.185) to Equation (B.186) requires that

$$F''_{kpq}(z) - \left(\frac{4p^2\pi^2}{\lambda_x^2} + \frac{4q^2\pi^2}{\lambda_y^2}\right) F_{kpq}(z) = 0 \tag{B.187}$$

and solving the ODE for $F_{kpq}(z)$ yields

$$F_{kpq}(z) = A_{kpq} e^{2\pi z\sqrt{\frac{p^2}{\lambda_x} + \frac{q^2}{\lambda_y}}} + B_{kpq} e^{-2\pi z\sqrt{\frac{p^2}{\lambda_x} + \frac{q^2}{\lambda_y}}}. \tag{B.188}$$

Periodicity requires that

$$u_x = \phi_1 - \frac{1}{4(1-\nu)}\left(\phi_0 + x\phi_1 + y\phi_2 + z\phi_3\right)_{,x}, \tag{B.189}$$

$$u_y = \phi_2 - \frac{1}{4(1-\nu)}\left(\phi_0 + x\phi_1 + y\phi_2 + z\phi_3\right)_{,y}, \quad \textit{and} \tag{B.190}$$

$$u_z = \phi_3 - \frac{1}{4(1-\nu)}\left(\phi_0 + x\phi_1 + y\phi_2 + z\phi_3\right)_{,z} \tag{B.191}$$

are periodic in x and y.

Starting with the potential function

$$\phi_i = \left[B_{i1}(z) + xB_{i2}(z) + yB_{i3}(z)\right] e^{2\pi i\left(p\frac{x}{\lambda_x} + q\frac{y}{\lambda_y}\right)} \tag{B.192}$$

restrictions on $B_{ij}(z)$ are determined such that u_i and σ_{ij} are periodic in x and y. This requires that

$$\phi_0 = [B_1(z) - xB_2(z) - yB_3(z)]e^{2\pi i\left(p\frac{x}{\lambda_x}+q\frac{y}{\lambda_y}\right)}, \tag{B.193}$$

$$\phi_x = B_2(z)\, e^{2\pi i\left(p\frac{x}{\lambda_x}+q\frac{y}{\lambda_y}\right)}, \tag{B.194}$$

$$\phi_y = B_3(z)\, e^{2\pi i\left(p\frac{x}{\lambda_x}+q\frac{y}{\lambda_y}\right)}, \quad \textit{and} \tag{B.195}$$

$$\phi_z = B_4(z)\, e^{2\pi i\left(p\frac{x}{\lambda_x}+q\frac{y}{\lambda_y}\right)}. \tag{B.196}$$

The displacement equations can then be written as

$$u_x = -\frac{1}{4(1-\nu)}(\phi_0 + z\phi_z)_{,x}, \tag{B.197}$$

$$u_y = -\frac{1}{4(1-\nu)}(\phi_0 + z\phi_z)_{,y}, \quad \textit{and} \tag{B.198}$$

$$u_z = \phi_z - \frac{1}{4(1-\nu)}(\phi_0 + z\phi_z)_{,z}. \tag{B.199}$$

The potential function

$$\phi_k = \sum_{p,q=-\infty}^{\infty} F_{kpq}(z)\, e^{2\pi i\left(p\frac{x}{\lambda_x}+q\frac{y}{\lambda_y}\right)} \tag{B.200}$$

can be determined for the film to be

$$\phi_k^f = \sum_{p,q=-\infty}^{\infty} F_{kpq}^f(z)\, e^{2\pi i\left(p\frac{x}{\lambda_x}+q\frac{y}{\lambda_y}\right)} \tag{B.201}$$

and for the substrate to be

$$\phi_k^s = \sum_{p,q=-\infty}^{\infty} F_{kpq}^s(z)\, e^{2\pi i\left(p\frac{x}{\lambda_x}+q\frac{y}{\lambda_y}\right)} \tag{B.202}$$

where the film coefficients $F^f_{kpq}(z)$ are requires to satisfy

$$F^f_{kpq}(z) = A^f_{kpq} e^{2\pi z\sqrt{\frac{p^2}{\lambda_x}+\frac{q^2}{\lambda_y}}} + B^f_{kpq} e^{-2\pi z\sqrt{\frac{p^2}{\lambda_x}+\frac{q^2}{\lambda_y}}} \tag{B.203}$$

and the substrate coefficients $F^s_{kpq}(z)$ are required to satisfy

$$F^s_{kpq}(z) = A^s_{kpq} e^{2\pi z\sqrt{\frac{p^2}{\lambda_x}+\frac{q^2}{\lambda_y}}} \tag{B.204}$$

as similarly derived in Equation (B.188). It is noted that $F^s_{kpq}(z)$ decays as z approaches negative infinity ($z \to -\infty$).

A^f_{kpq}, B^f_{kpq}, and A^s_{kpq} are needed, therefore the relations

$$\sigma^f_{ij} n^f_j = -\sigma^0_{ij} n^f_j \tag{B.205}$$

on the film surface, and

$$[\![\sigma_{ij}]\!] n^s_j = -\sigma^0_{ij} n^s_j \tag{B.206}$$

and

$$[\![u_i]\!] = u^f_i - u^s_i = 0 \tag{B.207}$$

on the substrate surface are utilized.

Terms in square brackets denote fields that are composed of the field induced by the substrate subtracted from the field induced by the film.

Enforcing Equation (B.207) on the substrate surface with $b_{00} = 0$ and $b_{pq} \sim \alpha$ and restricting that expression to order α^3 yields

$$u^f_x - u^s_x = -\frac{1}{4(1-\nu)}\left(\phi^f_0 + z\phi^f_z\right)_{,x} - -\frac{1}{4(1-\nu)}\left(\phi^s_0 + z\phi^s_z\right)_{,x} = 0 \tag{B.208}$$

therefore

$$\phi^f_{0,x} + z\phi^f_{z,x} - \phi^s_{0,x} - z\phi^s_{z,x} = 0 \tag{B.209}$$

on the substrate surface.

Using the potential function

$$\phi_{k,x}^{f,s} = \sum_{p,q=-\infty}^{\infty} F_{kpq}^{f,s}(z) \frac{2\pi ip}{\lambda_x} e^{2\pi i\left(p\frac{x}{\lambda_x}+q\frac{y}{\lambda_y}\right)} \tag{B.210}$$

and substituting Equation (B.210) into Equation (B.209) yields

$$\sum_{p,q=-\infty}^{\infty} [F_{0pq}^{f}(z) + zF_{3pq}^{f}(z) - F_{0pq}^{s}(z) - zF_{3pq}^{s}(z)] \frac{2\pi ip}{\lambda_x} e^{2\pi i\left(p\frac{x}{\lambda_x}+q\frac{y}{\lambda_y}\right)} = 0 \tag{B.211}$$

on the substrate surface.

The term in brackets in Equation (B.211) must then be expanded to $O(\alpha)^3$.

It is noted that, for $b_{00} = 0$

$$z = \sum_{m,n=-\infty}^{\infty} b_{mn} e^{2\pi i\left(m\frac{x}{\lambda_x}+n\frac{y}{\lambda_y}\right)} \sim \alpha \tag{B.212}$$

and

$$A_{kpq}^{f} \sim B_{kpq}^{f} \sim A_{kpq}^{s} \sim \alpha \tag{B.213}$$

with the exception of A_{k00}^{f} and A_{k00}^{s}. Terms proportional to α must vanish as $\alpha \to 0$ ($slope \to 0$). Therefore

$$F_{k00}^{f} = A_{k00}^{f} \sim O(1), and \tag{B.214}$$

$$F_{k00}^{s} = A_{k00}^{s} \sim O(1). \tag{B.215}$$

On the substrate surface

$$\begin{aligned} F_{kpq}^{f}(z) &= A_{kpq}^{f}\left(1 + 2\pi z\sqrt{\frac{p^2}{\lambda_x^2}+\frac{q^2}{\lambda_y^2}}\right) + B_{kpq}^{f}\left(1 - 2\pi z\sqrt{\frac{p^2}{\lambda_x^2}+\frac{q^2}{\lambda_y^2}}\right) + O(\alpha)^3 \\ &= A_{kpq}^{f} + B_{kpq}^{f} + 2\pi z\sqrt{\frac{p^2}{\lambda_x^2}+\frac{q^2}{\lambda_y^2}}\left(A_{kpq}^{f} - B_{kpq}^{f}\right) + O(\alpha)^3 \end{aligned} \tag{B.216}$$

$$F^s_{kpq}(z) = A^s_{kpq}\left(1 + 2\pi z\sqrt{\frac{p^2}{\lambda_x^2} + \frac{q^2}{\lambda_y^2}}\right) + O(\alpha)^3 \tag{B.217}$$

Substituting Equations (B.216) and (B.217) into Equation (B.211) yields

$$\sum_{p,q=-\infty}^{\infty} [\left(A^f_{0pq} - A^s_{0pq}\right)\left(1 + 2\pi z\sqrt{\frac{p^2}{\lambda_x^2} + \frac{q^2}{\lambda_y^2}}\right) + B^f_{0pq}\left(1 - 2\pi z\sqrt{\frac{p^2}{\lambda_x^2} + \frac{q^2}{\lambda_y^2}}\right) + \left(A^f_{3pq} - A^s_{3pq}\right)z + B^f_{3pq}z]\frac{2\pi ip}{\lambda_x}e^{2\pi i\left(p\frac{x}{\lambda_x} + q\frac{y}{\lambda_y}\right)} + O(\alpha)^3 = 0 \tag{B.218}$$

therefore

$$\sum_{p,q=-\infty}^{\infty} [\left(A^f_{0pq} - A^s_{0pq} + B^f_{0pq}\right) + [2\pi\sqrt{\frac{p^2}{\lambda_x^2} + \frac{q^2}{\lambda_y^2}}\left(A^f_{0pq} - A^s_{0pq} - B^f_{0pq}\right) + \left(A^f_{3pq} - A^s_{3pq} + B^f_{3pq}\right)]z]\frac{2\pi ip}{\lambda_x}e^{2\pi i\left(p\frac{x}{\lambda_x} + q\frac{y}{\lambda_y}\right)} + O(\alpha)^3 = 0. \tag{B.219}$$

Substituting Equation (B.212) into Equation (B.219) yields

$$\sum_{p,q=-\infty}^{\infty} [\left(A^f_{0pq} - A^s_{0pq} + B^f_{0pq}\right)]\frac{2\pi ip}{\lambda_x}e^{2\pi i\left(p\frac{x}{\lambda_x} + q\frac{y}{\lambda_y}\right)} \sum_{p,q=-\infty}^{\infty}\sum_{m,n=-\infty}^{\infty} [2\pi\sqrt{\frac{p^2}{\lambda_x^2} + \frac{q^2}{\lambda_y^2}}\left(A^f_{0pq} - A^s_{0pq} - B^f_{0pq}\right) + \left(A^f_{3pq} - A^s_{3pq} + B^f_{3pq}\right)]b_{mn}\frac{2\pi ip}{\lambda_x}e^{2\pi i\left((p+m)\frac{x}{\lambda_x} + (q+n)\frac{y}{\lambda_y}\right)} = O(\alpha)^3 \tag{B.220}$$

Note that

$$\int_0^{\lambda_x}\int_0^{\lambda_y} e^{-2\pi i\left(r\frac{x}{\lambda_x} + s\frac{y}{\lambda_y}\right)}\,dy\,dx = \begin{cases}\lambda_x\lambda_y, & \text{if } r = s = 0;\\ 0, & \text{otherwise.}\end{cases} \tag{B.221}$$

Because of the orthogonality condition, Equation (B.221), $p + m - r = 0$ and $q + n - s = 0$. Therefore, $m = r - p$ and $n = s - q$. Applying orthogonality to Equation (B.220) produces

$$\left(A^f_{0rs} - A^s_{0rs} + B^f_{0rs}\right) r + \sum_{p,q=-\infty}^{\infty} [2\pi \sqrt{\frac{p^2}{\lambda_x^2} + \frac{q^2}{\lambda_y^2}} \left(A^f_{0pq} - A^s_{0pq} - B^f_{0pq}\right) + \left(A^f_{3pq} - A^s_{3pq} + B^f_{3pq}\right)] p b_{r-p,s-q}. \quad \text{(B.222)}$$

From the $[\![u_y]\!] = 0$ condition on the substrate surface, it can be similarly determined that

$$\left(A^f_{0rs} - A^s_{0rs} + B^f_{0rs}\right) s + \sum_{p,q=-\infty}^{\infty} [2\pi \sqrt{\frac{p^2}{\lambda_x^2} + \frac{q^2}{\lambda_y^2}} \left(A^f_{0pq} - A^s_{0pq} - B^f_{0pq}\right) + \left(A^f_{3pq} - A^s_{3pq} + B^f_{3pq}\right)] q b_{r-p,s-q}. \quad \text{(B.223)}$$

From the $[\![u_z]\!] = 0$ condition on the substrate surface, it can be determined that

$$\begin{aligned}
&\sum_{p,q=-\infty}^{\infty} [k \left(A^f_{3pq} - A^s_{3pq} + B^f_{3pq}\right) + 2\pi \sqrt{\frac{p^2}{\lambda_x^2} + \frac{q^2}{\lambda_y^2}} \left(-A^f_{0pq} + A^s_{0pq} + B^f_{0pq}\right)] e^{2\pi i \left((p)\frac{x}{\lambda_x} + (q)\frac{y}{\lambda_y}\right)} \\
&+ \sum_{p,q=-\infty}^{\infty} \sum_{m,n=-\infty}^{\infty} [2\pi \sqrt{\frac{p^2}{\lambda_x^2} + \frac{q^2}{\lambda_y^2}} k \left(A^f_{3pq} - A^s_{3pq} - B^f_{3pq}\right) \\
&+ 2\pi \sqrt{\frac{p^2}{\lambda_x^2} + \frac{q^2}{\lambda_y^2}} \left(-A^f_{0pq} + A^s_{0pq} - B^f_{0pq}\right) \\
&+ \left(-A^f_{3pq} + A^s_{3pq} + B^f_{3pq}\right)] b_{mn} e^{2\pi i \left((p+m)\frac{x}{\lambda_x} + (q+n)\frac{y}{\lambda_y}\right)} = 0
\end{aligned} \quad \text{(B.224)}$$

where $k = 3 - 4\nu$. Applying orthogonality to Equation (B.224) yields

$$\begin{aligned}
&[k \left(A^f_{3rs} - A^s_{3rs} + B^f_{3rs}\right) + 2\pi \sqrt{\frac{r^2}{\lambda_x^2} + \frac{s^2}{\lambda_y^2}} \left(-A^f_{0rs} + A^s_{0rs} + B^f_{0rs}\right)] \\
&+ \sum_{p,q=-\infty}^{\infty} [2\pi \sqrt{\frac{p^2}{\lambda_x^2} + \frac{q^2}{\lambda_y^2}} k \left(A^f_{3pq} - A^s_{3pq} - B^f_{3pq}\right) \\
&+ 2\pi \sqrt{\frac{p^2}{\lambda_x^2} + \frac{q^2}{\lambda_y^2}} \left(-A^f_{0pq} + A^s_{0pq} - B^f_{0pq}\right) \\
&+ \left(-A^f_{3pq} + A^s_{3pq} + B^f_{3pq}\right)] b_{r-p,s-q} = 0.
\end{aligned} \quad \text{(B.225)}$$

Equation (B.222) shows that

$$A^f_{0rs} - A^s_{0rs} + B^f_{0rs} = O(\alpha)^2 \tag{B.226}$$

and therefore

$$A^f_{0rs} - A^s_{0rs} = -B^f_{0rs} + O(\alpha)^2 . \tag{B.227}$$

In turn, Equation (B.225) shows that

$$k\left(A^f_{3rs} - A^s_{3rs} + B^f_{3rs}\right) + 2\pi\sqrt{\frac{r^2}{\lambda_x^2} + \frac{s^2}{\lambda_y^2}}\left(-A^f_{0rs} + A^s_{0rs} + B^f_{0rs}\right) = O(\alpha)^2 . \tag{B.228}$$

Also, from Equation (B.227),

$$-A^f_{0rs} + A^s_{0rs} + B^f_{0rs} = 2B^f_{0rs} + O(\alpha)^2 \tag{B.229}$$

which, when substituted into Equation (B.228), yields

$$k\left(A^f_{3rs} - A^s_{3rs} + B^f_{3rs}\right) = -4\pi B^f_{0rs}\sqrt{\frac{r^2}{\lambda_x^2} + \frac{s^2}{\lambda_y^2}} + O(\alpha)^2 . \tag{B.230}$$

Combining these results with Equation (B.222) yields

$$\begin{aligned}\left(A^f_{0rs} - A^s_{0rs} + B^f_{0rs}\right) r + \sum_{p,q=-\infty}^{\infty} [&-4\pi B^f_{0pq}\sqrt{\frac{p^2}{\lambda_x^2} + \frac{q^2}{\lambda_y^2}} \\ &-\frac{4\pi}{k} B^f_{0pq}\sqrt{\frac{p^2}{\lambda_x^2} + \frac{q^2}{\lambda_y^2}}]\, p b_{r-p,s-q}\end{aligned} \tag{B.231}$$

which simplifies to

$$\left(A^f_{0rs} - A^s_{0rs} + B^f_{0rs}\right) r = 4\pi\left(1 - \frac{1}{k}\right)\sum_{p,q=-\infty}^{\infty} p\sqrt{\frac{p^2}{\lambda_x^2} + \frac{q^2}{\lambda_y^2}} B^f_{0pq} b_{r-p,s-q}$$

C Potential Function Coefficients

$$
\begin{aligned}
A_{0rs} &= \frac{1}{4e^{4a_{00}\pi\sqrt{R^2+S^2}}M\pi\sqrt{R^2+S^2}}\{\left((K-1)\left(b_{rs}\left(K-4a_{00}\pi\sqrt{R^2+S^2}\right)\right.\right.\\
&+ \left.\left.a_{rs}e^{2a_{00}\pi\sqrt{R^2+S^2}}\right)\left(-1-K+4a_{00}\pi\sqrt{R^2+S^2}\right)\right)\sigma_0\}\\
&+ \frac{\frac{i}{8}\left(8a_{00}\left(1+K\right)\pi\left(R^2+S^2\right)-\sqrt{R^2+S^2}\left(1+32a_{00}^2\pi\left(R^2+S^2\right)\right)\right)\left(RS_1+SS_2\right)}{e^{4a_{00}\pi\sqrt{R^2+S^2}}\left(1+K\right)\pi\left(R^2+S^2\right)^{\frac{3}{2}}}\\
&+ \frac{\left(-16a_{00}^2\pi^2+\frac{-1+K^2}{R^2+S^2}\right)S_3}{16e^{4a_{00}\pi\sqrt{R^2+S^2}}M\pi^2}\\
&+ \frac{\frac{-i}{16}\left(-1-2K+K^2-4a_{00}\left(1+K\right)\pi\sqrt{R^2+S^2}\left(RS_4+SS_5\right)\right)}{e^{2a_{00}\pi\sqrt{R^2+S^2}}M\pi^2\left(R^2+S^2\right)^{\frac{3}{2}}}\\
&- \frac{\left(1+K\right)\left(\left(K-1\right)\sqrt{R^2+S^2}-4a_{00}\pi\left(R^2+S^2\right)\right)S_6}{16e^{2a_{00}\pi\sqrt{R^2+S^2}}M\pi^2\left(R^2+S^2\right)^{\frac{3}{2}}},
\end{aligned}
\tag{C.1}
$$

$$
A_{1rs} = \frac{-S_1}{2e^{4a_{00}\pi\sqrt{R^2+S^2}}\left(1+K\right)} + \frac{-S_4}{2e^{2a_{00}\pi\sqrt{R^2+S^2}}M\pi\sqrt{R^2+S^2}},
\tag{C.2}
$$

$$
A_{2rs} = \frac{-S_2}{2e^{4a_{00}\pi\sqrt{R^2+S^2}}\left(1+K\right)} + \frac{-S_5}{2e^{2a_{00}\pi\sqrt{R^2+S^2}}M\pi\sqrt{R^2+S^2}},
\tag{C.3}
$$

$$
\begin{aligned}
A_{3rs} &= \frac{\left(b_{rs}-a_{rs}e^{2a_{00}\pi\sqrt{R^2+S^2}}\right)\left(K-1\right)\sigma_0}{e^{4a_{00}\pi\sqrt{R^2+S^2}}M}\\
&+ \frac{\frac{i}{2}\left(-1+8a_{00}\pi\sqrt{R^2+S^2}\right)\left(RS_1+SS_2\right)}{e^{4a_{00}\pi\sqrt{R^2+S^2}}\left(1+K\right)\sqrt{R^2+S^2}} + \frac{\left(k+4a_{00}\pi\sqrt{R^2+S^2}\right)S_3}{4e^{4a_{00}\pi\sqrt{R^2+S^2}}M\pi\sqrt{R^2+S^2}}\\
&+ \frac{\frac{-i}{2}\left(K-1\right)\left(RS_4+SS_5\right)}{e^{2a_{00}\pi\sqrt{R^2+S^2}}M\pi\left(R^2+S^2\right)} - \frac{\left(1+K\right)S_6}{4e^{2a_{00}\pi\sqrt{R^2+S^2}}M\pi\sqrt{R^2+S^2}},
\end{aligned}
\tag{C.4}
$$

$$
B_{0rs} = \frac{b_{rs}\left(K-1\right)\sigma_0}{4M\pi\sqrt{R^2+S^2}},
\tag{C.5}
$$

$$
B_{1rs} = -\frac{\left(2R^2+S^2\right)S_1+RSS_2}{2\left(1+K\right)\left(R^2+S^2\right)},
\tag{C.6}
$$

$$
B_{2rs} = -\frac{RSS_1+\left(R^2+2S^2\right)S_2}{2\left(1+K\right)\left(R^2+S^2\right)},
\tag{C.7}
$$

$$B_{3rs} = \frac{S_3}{4M\pi\sqrt{R^2+S^2}}, \tag{C.8}$$

$$\begin{aligned}
C_{0rs} &= \frac{\left(-a_{rs} + b_{rs}e^{2a_{00}\pi\sqrt{R^2+S^2}}\right)(K-1)\,\sigma_0}{4e^{2a_{00}\pi\sqrt{R^2+S^2}}M\pi\sqrt{R^2+S^2}} \\
&+ \frac{\left(-b_{rs} + a_{rs}e^{2a_{00}\pi\sqrt{R^2+S^2}}\right)(K-1)\left(-K + 4a_{00}\pi\sqrt{R^2+S^2}\right)\sigma_0}{4e^{4a_{00}\pi\sqrt{R^2+S^2}}M\pi\sqrt{R^2+S^2}} \\
&+ \frac{\frac{i}{8}\left(RS_1 + SS_2\right)}{e^{4a_{00}\pi\sqrt{R^2+S^2}}(1+K)\,\pi\left(R^2+S^2\right)^{\frac{3}{2}}}\left\{8a_{00}(1+K)\,\pi\left(R^2+S^2\right)\right. \\
&\left. +\sqrt{R^2+S^2}\left(-1 + e^{4a_{00}\pi\sqrt{R^2+S^2}} - 32a_{00}^2\pi^2\left(R^2+S^2\right)\right)\right\} \\
&+ \frac{\left(-1 + K^2 - 16a_{00}^2\pi^2\left(R^2+S^2\right)\right)S_3}{16e^{4a_{00}\pi\sqrt{R^2+S^2}}M\pi^2\left(R^2+S^2\right)} \\
&+ \frac{\frac{-i}{16}\left(-1 - 2K + K^2 - 4a_{00}(1+K)\,\pi\sqrt{R^2+S^2}\right)\left(RS_4 + SS_5\right)}{e^{2a_{00}\pi\sqrt{R^2+S^2}}M\pi^2\left(R^2+S^2\right)^{\frac{3}{2}}} \\
&- \frac{(1+K)\left((K-1)\sqrt{R^2+S^2} - 4a_{00}\pi\left(R^2+S^2\right)\right)S_6}{16e^{2a_{00}\pi\sqrt{R^2+S^2}}M\pi^2\left(R^2+S^2\right)^{\frac{3}{2}}},
\end{aligned} \tag{C.9}$$

$$C_{1rs} = \frac{\left(1 - e^{-4a_{00}\pi\sqrt{R^2+S^2}}\right)S_1}{2+2K} - \frac{S_4}{2e^{2a_{00}\pi\sqrt{R^2+S^2}}M\pi\sqrt{R^2+S^2}}, \tag{C.10}$$

$$C_{2rs} = \frac{\left(1 - e^{-4a_{00}\pi\sqrt{R^2+S^2}}\right)S_2}{2+2K} - \frac{S_5}{2e^{2a_{00}\pi\sqrt{R^2+S^2}}M\pi\sqrt{R^2+S^2}}, \tag{C.11}$$

$$\begin{aligned}
C_{3rs} &= \frac{\left(b_{rs} - a_{rs}e^{2a_{00}\pi\sqrt{R^2+S^2}}\right)(K-1)\,\sigma_0}{e^{4a_{00}\pi\sqrt{R^2+S^2}}M} \\
&+ \frac{\frac{i}{2}\left(-1 + e^{4a_{00}\pi\sqrt{R^2+S^2}} + 8a_{00}\pi\sqrt{R^2+S^2}\right)\left(RS_1 + SS_2\right)}{e^{4a_{00}\pi\sqrt{R^2+S^2}}(1+K)\sqrt{R^2+S^2}} \\
&+ \frac{\left(e^{4a_{00}\pi\sqrt{R^2+S^2}} + k + 4a_{00}\pi\sqrt{R^2+S^2}\right)S_3}{4e^{4a_{00}\pi\sqrt{R^2+S^2}}M\pi\sqrt{R^2+S^2}} \\
&+ \frac{\frac{-i}{2}(K-1)\left(RS_4 + SS_5\right)}{e^{2a_{00}\pi\sqrt{R^2+S^2}}M\pi\left(R^2+S^2\right)} - \frac{(1+K)\,S_6}{4e^{2a_{00}\pi\sqrt{R^2+S^2}}M\pi\sqrt{R^2+S^2}},
\end{aligned} \tag{C.12}$$

$$S_1 = \sum_{p,q=-\infty}^{\infty} \frac{2ib_{pq}\,(K-1)\,P\pi\sigma_0}{M} b_{r-p,s-q}, \tag{C.13}$$

$$S_2 = \sum_{p,q=-\infty}^{\infty} \frac{2ib_{pq}\,(K-1)\,Q\pi\sigma_0}{M} b_{r-p,s-q}, \tag{C.14}$$

$$S_3 = \sum_{p,q=-\infty}^{\infty} \frac{8b_{pq}\,(K-1)\,\pi^2\,(PR+QS)\,\sigma_0}{1+K} b_{r-p,s-q}, \tag{C.15}$$

$$\begin{aligned} S_4 \;=\; & \frac{-4i\left(b_{pq} - a_{pq}e^{2a_{00}\pi\sqrt{P^2+Q^2}}\right)(K-1)\,\pi^2}{e^{2a_{00}\pi\sqrt{P^2+Q^2}}\,(1+K)\,\sqrt{P^2+Q^2}}\big\{4P^2R \\ & -(-3+K)\,Q^2R + (1+K)\,PQS\big\}\sigma_0 a_{r-p,s-q}, \end{aligned} \tag{C.16}$$

$$\begin{aligned} S_5 \;=\; & \frac{4i\left(b_{pq} - a_{pq}e^{2a_{00}\pi\sqrt{P^2+Q^2}}\right)(K-1)\,\pi^2}{e^{2a_{00}\pi\sqrt{P^2+Q^2}}\,(1+K)\,\sqrt{P^2+Q^2}}\big\{-(1+K)\,PQR \qquad \text{(C.17)} \\ & +(-3+K)\,P^2S - 4Q^2S\big\}\sigma_0 a_{r-p,s-q}, \qquad \text{(C.18)} \end{aligned}$$

and

$$S_6 = \sum_{p,q=-\infty}^{\infty} \frac{8a_{pq}\,(K-1)\,\pi^2\,(PR+QS)\,\sigma_0}{1+K} a_{r-p,s-q}, \tag{C.19}$$